ABSTRACT

Title of Dissertation: MEMS-BASED SILICON NITRIDE THIN FILM MATERIALS AND DEVICES AT CRYOGENIC TEMPERATURES FOR SPACE APPLICATIONS

Wen-Hsien Chuang, Doctor of Philosophy, 2005

Dissertation directed by: Professor Reza Ghodssi

Department of Electrical and Computer Engineering

Microshutter arrays, scheduled to be launched in 2011 as part of NASA's James Webb Space Telescope (JWST), will be the first micro-scale optical devices in outer space using MEMS technology. As the microshutter arrays consist of electrical and mechanical components and must operate in a cryogenic environment reliably over a 10 year mission lifetime, a fundamental challenge for the development of this device is to understand the mechanical behaviors of the micro-scale materials used and the possible failure mechanisms at 30 K.

This thesis investigates the mechanical properties and reliability of low-stress LPCVD silicon nitride thin films, the structural materials of the microshutter arrays, at cryogenic temperatures. A helium-cooled cryogenic measurement setup installed inside a focused-ion-beam system is designed, implemented, and characterized to obtain a

cryogenic environment down to 20 K. Resonating T-shaped cantilevers with different "milling masses" are used to measure the Young's modulus of silicon nitride thin films, while the fracture strength is characterized by bending tests of these beams. A passive high-sensitivity microgauge sensor based on displacement amplification is introduced to measure residual stress and coefficients of thermal expansion, which are critical for the device performance. To achieve accelerated fatigue study of the microshutter arrays, a novel mechanical-amplifier actuator is designed, fabricated, and tested to emulate their torsional operating stress. Furthermore, nano-scale tensile fatigue tests are demonstrated using similar mechanical-amplifier actuators.

The research results of this thesis provide important thin film material parameters for the design, fabrication, and characterization of the microshutter arrays. Moreover, the presented test devices and experimental techniques are not limited for space applications only but can be extended for characterization of other thin film materials used in MEMS and microsystems.

MEMS-BASED SILICON NITRIDE THIN FILM MATERIALS AND DEVICES AT

CRYOGENIC TEMPERATURES FOR SPACE APPLICATIONS

by

Wen-Hsien Chuang

Dissertation submitted to the Faculty of the Graduate School of the
University of Maryland, College Park in partial fulfillment
of the requirements for the degree of
Doctor of Philosophy
2005

Advisory Committee:
        Professor Reza Ghodssi, Chair
        Professor Amr Baz
        Professor John Melngailis
        Professor Robert Newcomb
        Professor Jon Orloff

DEDICATION

To my parents and my wife for their love, sacrifice, and support

ACKNOWLEDGEMENTS

TABLE OF CONTENTS

LIST OF TABLES

LIST OF FIGURES

CHAPTER 1

INTRODUCTION

For centuries people were fascinated by the prospect of making mechanical devices smaller and smaller, while maintaining their functionality. Since 1960, the complexity and performance of microelectronic devices has increased by many orders of magnitude, whereas size, power consumption, and price have been reduced significantly. Meanwhile, the advance of microfabrication techniques in the semiconductor industry also provides an opportunity for researchers to develop versatile systems on the micro-scale, called microelectromechanical systems (MEMS). Basically, MEMS are microscale devices, which combine electrical and mechanical components, and are fabricated using integrated circuit batch-processing technologies. Various MEMS structures such as linear comb capacitors, micro-mirrors, micro-channels, cantilevers, and diaphragms have been successfully fabricated and widely used in accelerometers [1], pressure sensors [2], optical switches [3], and lab-on-chip platforms [4]. Key benefits of MEMS devices include miniature size, light weight, high resonant frequencies, short thermal time constant, and the capability to integrate with microelectronics.

As the field of MEMS grows considerably, the advantages of smaller, less costly devices and systems have given impetus to develop MEMS devices for space applications. Micro-spacecrafts [5], miniature communication satellites [6], and meteorological instrumentation [7] based on utilization of MEMS technology have been proposed. However, one of the key challenges facing the design of these devices is reliability in the outer space environment. Despite the increasing popularity of MEMS in research and

industry, reliability is still a critical factor that hinders the commercialization of MEMS products. For space applications, failure of MEMS devices may cause not only enormous costs but also unpredictable disastrous results. Therefore, starting with the selection of materials in the design phase, a complete understanding of mechanical properties and reliability issues in the operational environment is crucial in the development of MEMS devices for space applications.

1.1 Motivation and background

The James Webb Space Telescope (JWST), scheduled to be launched in 2011, is currently being developed at NASA Goddard Space Flight Center to determine the origins of galaxies, clusters, and large-scale structures in the universe [8]. In order to observe galaxies in the peak of the merging and star-forming era, JWST operation requires a spectroscopic coverage in the near-infrared (NIR) wavelength region from 0.6 to 5 μm. A Multi-Object Spectrometer (MOS) has been proposed for the JWST to fulfill the detection of the NIR wavelength region. For the operation of the MOS, an imaging mode and a spectrum mode can be interchanged by supporting a prism assembly, gratings, and a mirror in the system. In order to cover a required spectral band without overlap in the spectrum mode, a programmable aperture mask (PAM) utilized as an object selector which can operate over a broad spectral range and select objects at random positions is needed. The selection of a set of objects for spectroscopic observation is based on a prior image of the area of the sky taken in the imaging mode.

A MEMS-based microshutter array (MSA) for application as the PAM on the JWST has been proposed at NASA Goddard Space Flight Center [9, 10]. The MSA design

2

consists of a 2 × 2 format mosaic of four 384 × 175 arrays placed in the JWST optical path at the focal plane. Each shutter element covers an area of 100 × 200 μm and is connected to a frame through a neck region and a torsion beam as shown in Figure 1.1 [11]. A schematic cross-section of a single shutter element indicating the primary components is shown in Figure 1.2 [12]. Since the fracture strength of silicon nitride thin films is higher than that of silicon, the shutter and torsion spring are made of low-stress low pressure chemical vapor deposition (LPCVD) silicon nitride with a thickness of 0.5 μm [13]. The frame of the MSA is 100 μm thick single crystal silicon with frame widths of less than 8 μm between the shutters. Around the perimeter of the shutter element is an overhanging light shield. This shield blocks light from leaking through the gaps between the shutter, hinge and the array frame when the shutter is in the horizontal closed position. There are two sets of electrodes utilized for addressing the MSA. One set of electrodes covers the shutter surface and is connected in column arrangement via leads on the torsion hinge and array frame. The second set of electrodes covers the side wall of the silicon frames and is connected in rows via leads on the top of the frame. Deposited over the column electrode on the shutter is a region of magnetic cobalt/iron alloy.

In the mechanism of actuation, a permanent tri-pole magnet aligned to the shutter rows is swept across the MSA along the columns [12]. As the magnet sweeps across the array, sequential rows of shutters are rotated from their horizontal closed position (Figure 1.2 (a)) to a vertical open orientation (Figure 1.2 (b)) in contact with the vertical electrodes. The selective nature of the MSA is then achieved electrostatically using three voltage bias levels where the difference between any two voltages is sufficient to hold the shutters open in contact with the vertical electrodes against the mechanical restoring force

of the torsion hinge. All combinations of the open shutter elements can be obtained by appropriately choosing the voltage bias in each row and column.

(a)   (b)
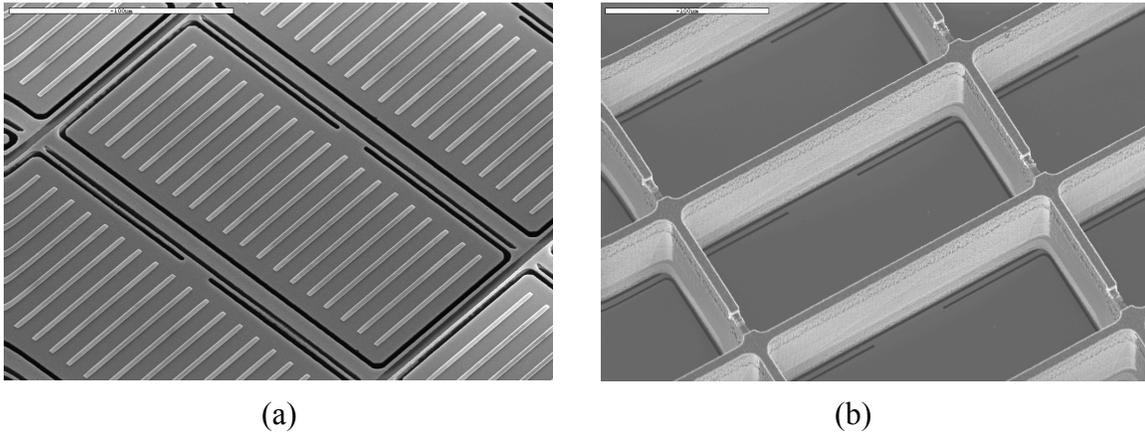
Figure 1.1: Scanning electron micrographs of a 128 × 64 microshutter array: (a) front-side view without light shields for clarity, and (b) back-side view.

(a)   (b)
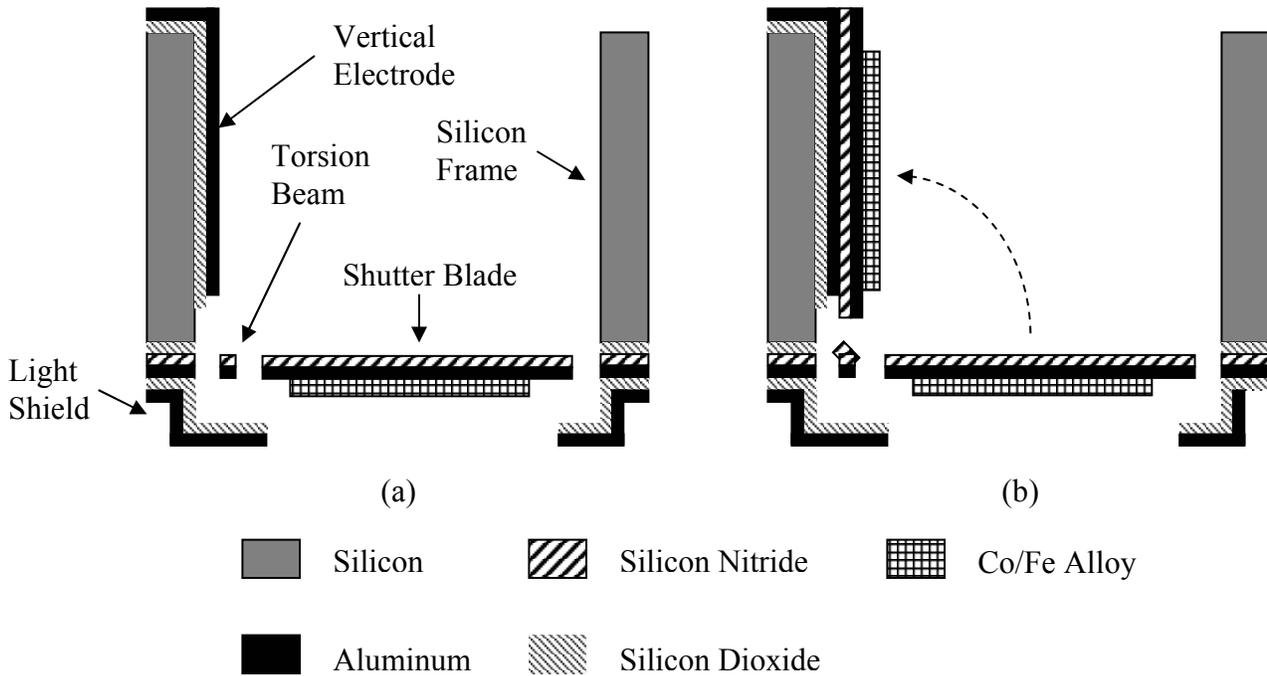
Figure 1.2: Schematic cross-section of a single shutter element: (a) at close state, and (b) at open state.

The scientific goal for the JWST is to detect extremely faint infrared photons coming from the farthest reaches of the universe. Temperature is an essential consideration since "heat" would create too much infrared background noise. To minimize thermal emissions into the Multi-Object Spectrometer, the JWST's orbit will be at the second Lagrange Point (L2), located 940,000 miles from the Earth in the anti-Sun direction to provide a thermally stable environment [11]. This location is inaccessible to space shuttle re-servicing missions. Thus, the MSA must operate in a cryogenic (~30 K) vacuum environment reliably over a 10 year mission lifetime without repair after launch.

The challenges facing the MSA are to design and fabricate test structures and devices emulating the same operation condition and to develop characterization techniques for comprehensive tests. As MEMS is a relatively new technology, emphasis over the past dozen years has been on new materials, new manufacturing processes, and new micro-devices. Limited mechanical property and reliability data of thin film materials utilized in MEMS devices is available, even for room temperature environment. Current state-of-the-art techniques for mechanical property and reliability characterization focus mainly on scaled down setups that are used for macroscopic material analysis and most often are developed for measuring polysilicon thin films. Therefore, it is clear that to expand MEMS devices for space applications, new test devices and characterization techniques suitable for the cryogenic environment need to be developed.

1.2 Literature review

1.2.1 Microelectromechanical systems technology

A. Fabrication techniques for MEMS

The evolution of microfabrication techniques to create precision three-dimensional micromachining structures in the last couple of decades has led to an exciting revolution in understanding and utilizing MEMS devices for different applications. The most common fabrication techniques for MEMS devices include bulk micromachining [14], surface micromachining [15], dissolved wafer process [16], LIGA (a German acronym for lithography, electroplating, and molding) [17], and micro-electro-discharge machining (EDM) [18]. A typical MEMS device can be realized by using any of these processes in their prevalent forms or several variants of these processes. In this research work, bulk micromachining and surface micromachining techniques are utilized to fabricate test devices and therefore are discussed in detail.

Bulk micromachining is based on anisotropic etching of single-crystalline silicon to form micro mechanical structures from the bulk of the silicon wafer [14]. Strongly alkaline liquids such as potassium hydroxide (KOH) preferentially etch the {100} planes of single crystalline silicon in comparison to the {111} planes. The mechanism responsible for orientation dependent etching in silicon has been suggested [19] [20] to be the bond structure of the atoms that are revealed in different surface planes. {100} planes of single crystalline silicon have atoms with two dangling bonds. However, atoms in {111} planes have only one dangling bond on the surface. Hence, atoms in {111} planes are more tightly bound to the rest of the crystal and this may explain the observed lower etch rate in these planes.

The difference in these etch rates (typically 100 times smaller in {111} planes) can be utilized to create three-dimensional structures in silicon substrates using standard photolithography in conjunction with masking layers such as silicon nitride. Anisotropic etching can be used either from the front side of the wafer, backside of the wafer or from both sides to realize an array of micromechanical structures. Figure 1.3 is a schematic diagram of process steps to fabricate a silicon nitride membrane using this technique. Bulk micromachining is a proven high-volume production process and is routinely used to fabricate microstructures due to its simplicity. However, the alkaline-based solutions are not compatible with CMOS fabrication processes and the etch rate of silicon in these chemicals is relatively slow (~ 1 μm/min). In addition, bulk micromachining prevents efficient use of silicon "real estate" since large etch windows need to be defined even for realizing small micromechanical structures.
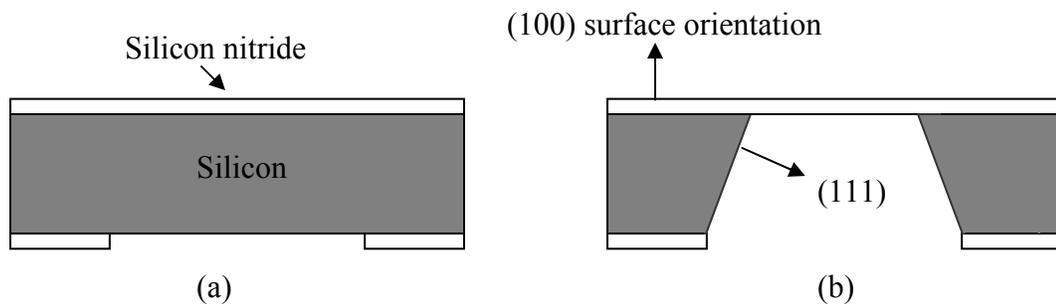
Figure 1.3: Schematic diagram of process steps to fabricate silicon nitride membrane using bulk micromachining technique: (a) deposit and pattern silicon nitride, and (b) etch silicon in alkaline liquid to produce cavity.

Surface-micromachining, on the other hand, is based on sequential deposition and etching of thin films on the surface of a carrier substrate [15]. Freestanding structures can be released by etching away sacrificial layers under structural thin films. The basic fabrication process sequence is shown in Figure 1.4. As the polycrystalline silicon thin

film exhibits excellent mechanical properties (its Young's modulus is near that of stainless steel and its fracture strength is close to the ultimate strength of nickel-iron) and in particular is known as one of the key materials for IC-derived processing, it has become the most common MEMS material, especially in surface micromachining technique. The early effort in the development of polycrystalline silicon micromechanical structures was to control the film stress after deposition. It has been found that the resonant frequency of a micromachined resonator is strongly related to the residual stress of the structural layer [21] and out-of-plane curvature of micromechanical structures is
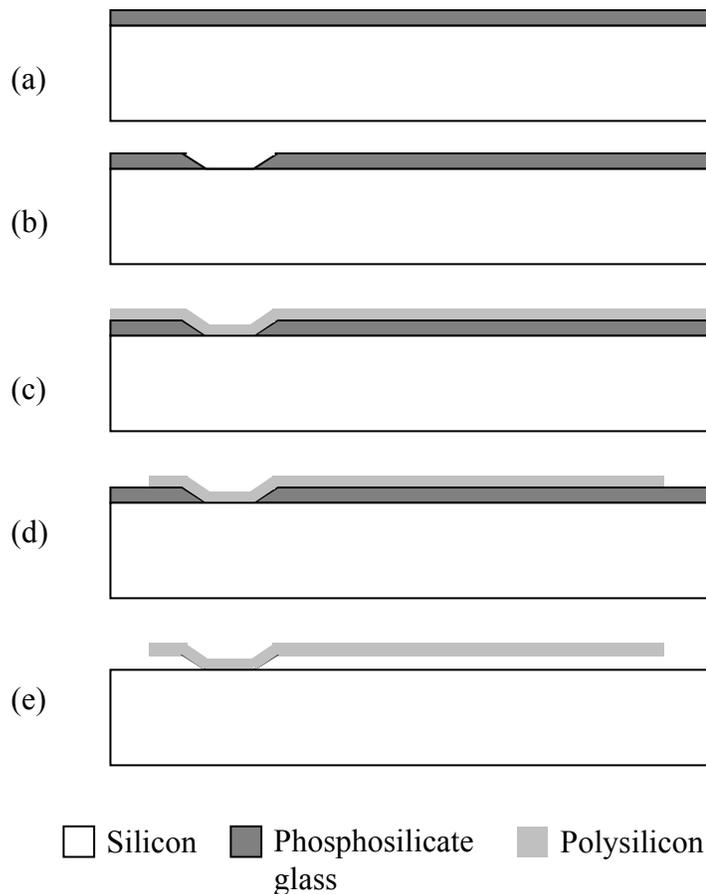
Figure 1.4: Basic surface micromachining process sequence: (a) deposition of sacrificial layer, (b) patterning of sacrificial layer with mask, (c) deposition of structural layer, (d) patterning of structural layer with mask, and (e) etching of sacrificial layer to produce free-standing structure.

8

generated due to the stress gradient of this thin film. Several techniques can be used to control the initial stress of polycrystalline silicon thin films such as annealing at high temperatures between 900 °C and 1150 °C with nitrogen flow [22]. Micromechanical structures upon release in wet etchant usually suffer from stiction problems. This problem has been widely studied and complex CMOS-based micromachining processes using up to 3-layers of polysilicon have been demonstrated to fabricate complex micromechanical structures such as micro-gears, micro-motors, and micro-mirrors [23]. One advantage of surface micromachining is that a slightly modified CMOS process can be used for the realization of the MEMS device. However, due to the structural layers being limited in thickness to a few microns, the disadvantage of this technique leads to fabrication difficulty of micromechanical structures with large mass or dimensions.

B. Integrated microsystems

One of the main goals for the development of MEMS technologies is to integrate microelectronic circuitry along with micromachined three-dimensional structures through microengineering. Integrated micro-systems offer several advantages as compared to standalone sensors, actuators, or circuits. Systems level advantages include improved reliability and performance, low cost, and ease of use. Since the range of applications of micro-systems is virtually limitless, the associated problems and solutions in each design are almost always unique and depend upon the specific applications and the choice of the transduction technique. Microsystems can be implemented by using either monolithic integration techniques or hybrid integration techniques. In hybrid microsystems, the sensor/actuator structures are located on a separate chip(s) from the electronic circuit chip.

9

The obvious advantage of using hybrid techniques is large latitude in the choice of the fabrication processes and materials for each of the chips constituting the microsystem. The main disadvantages are that it generally degrades performance and often adds complexity to the packaging of the overall system. In the development of the microshutter array, a CMOS-based dynamic random access memory (DRAM) device is integrated with each array on the same chip and utilized as an addressing circuit [10]. Four individual chips are then attached to a multi-chip module (MCM) for assembly.

In contrast, monolithic integration of microelectromechanical structures with microelectronic circuits can potentially create the most compact and versatile microsystems. However, the materials and processes for the micromechanical structures are constrained to be compatible with silicon and its processing techniques. Examples of commercialized monolithic microsystems are the digital micromirror array from Texas Instruments [24], the surface micromachined accelerometers from Analog Devices [25], and the room temperature bolometer infrared array from Honeywell [26].

C. Packaging of MEMS devices

As MEMS technology has evolved out of semiconductor processing technology, some of the packaging concepts have also developed from conventional semiconductor or IC packaging techniques. Even so, packaging of MEMS devices is more complex since in some cases it needs to provide protection from the environment while at other times it needs to allow access to the environment to measure or affect the direct physical or chemical parameters. Stresses and thermal effects, induced during the packaging and interconnection steps, can adversely affect the mechanical performance of MEMS

devices. Currently, it is estimated that MEMS packaging costs are in the range of 50% to 75% of the component's total cost [27].

Very often MEMS packaging relies on wafer level packaging [28]. Since MEMS devices have movable structures on the surface of the wafer, addition of a cap wafer on the silicon substrate makes the device suitable for handling and assembly. A typical capping process involves bonding of the substrate with active devices to a second wafer either of the same material or of different material. The bond is obtained by using glass frit material or by using anodic bonding created by the application of electrical potential. Additionally, many MEMS devices such as accelerometers, RF filters, and digital micromirror displays require the moving parts to be enclosed in hermetically sealed cavities. The cavity pressure in this case determines the frequency response of the micromechanical structure due to viscous damping effects [29]. The high vacuum cavities can also be fabricated by using wafer level packaging techniques. However, even if the bonding process is performed in high vacuum environment, it is found that the pressure in the enclosed cavities is high. This is thought to be due to outgassing effects and the generation of gaseous by-products during the bonding reaction [30]. A more important problem concerns the maintenance of the high vacuum over the lifetime of the sensors. Even an extremely small leak rate from the cavities which is impossible to be measured using conventional leak-rate detection methods can influence the sensor performance dramatically. New solutions that use active gettering materials inside these enclosed cavities have been proposed [30].

For packaging of the miroshutter arrays, the main challenge is the cryogenic operation of the whole system at outer space. Even a slight mismatch of the coefficient of

thermal expansion (CTE) could distort or damage the delicate shutter element. The current design adopts a silicon multi-chip module (MCM) approach where four individual shutter arrays (chips) are attached from the backside via indium bumps [31]. The electrical connections between the microshutter arrays and MCM bonding pads are obtained by wirebonding from the top side. The fully assembled microshutter array will consist of 16 individual microshutter chips, and each chip is approximately 6 cm square.

1.2.2   Reliability and failure mechanisms of MEMS

In recent years, enormous progress has been made in developing new design concepts, new processing techniques, and in identifying new applications for MEMS [32]. Widespread acceptance of such technologies, both for large-volume commercialization and for the use of a few components in critical applications, is dictated by their reliability. Identification of the mechanisms of failure, development of predictive models for such mechanisms, and finally, the inclusion of such models in computer-aided-design tools for MEMS form the goals of reliability engineering.

In general, there are three kinds of failure mechanisms for MEMS devices: process related failure mechanisms, in-use failure mechanisms, and packaging related failure mechanisms [33]. Similar to IC development, early failures of MEMS devices are affected by defects from microfabrication. Particles, inter-metallic diffusion, under-cutting, poor adhesion, and non-uniform step coverage all will lead to failure in operation. For surface micromachined MEMS devices, the release process to remove sacrificial layers usually causes permanent adhesion of microstructures to adjacent structures, which is the phenomenon called stiction. Carbon dioxide (CO_2) super critical drying [34],

incorporation of dimples to minimize contact area [35], and monolayer surface coatings [36] have been widely studied and successfully demonstrated to avoid this release stiction.

The fact that MEMS devices involve moving structures is the most obvious aspect in which they are different from conventional IC devices and this certainly introduces new in-use failure mechanisms. During the early stage of useful lifetime, the failures are mostly caused by external events, such as voltage excursion, vibration, shock loading, and electrostatic discharge (ESD). Stiction during the normal operation may also occur at this time due to capillary forces, electrostatic attraction, and chemical bonding. As MEMS devices are used continuously, mechanical failures (including fracture, fatigue, creep, and frictional wear), electrostatic charging (charge accumulation in dielectric layers), electromigration in electromagnets, and changes in morphology or geometry with temperature (bending or warping of components) start to deteriorate and render MEMS devices inoperative. These failure mechanisms are a function of operation time and are difficult to be characterized quantitatively.

MEMS devices face more challenges when it comes to packaging as mentioned previously. In addition to the same packaging related failure mechanisms existing in IC devices, the requirement of environmental exposure for some MEMS devices accelerates corrosion of electrical leads and bonding pads as a result of incomplete encapsulation. Furthermore, hinged, cantilevered, and floating components utilized in MEMS devices are very vulnerable to the packaging process, whether from mechanical or thermal stress or from contamination. Even a small stress change in these structures may induce a significant shift in performance and lead to failure.

Currently, MEMS reliability appears to be a key limiting factor for technology exploitation and volume production [37]. Many of the MEMS failure mechanisms are not well understood. The lack of understanding presents a challenge in developing practical testing and qualification techniques for MEMS devices. On the near horizon, if these issues can be addressed and overcome, there is no doubt that MEMS technology will have a huge impact on our daily lives.

1.3 Techniques for mechanical property and reliability characterizations of MEMS materials

It is well known that mechanical properties of thin films are different from those of bulk materials [38]. This difference can be explained by the large surface-to-volume ratio, since the microstructure of the surface will have significant influence on the mechanical properties of thin films. Furthermore, defects and unique microstructures from the fabrication process in thin films also contribute to the variation of mechanical properties.

Since the late 1980s, researchers have tried to determine mechanical properties of thin film materials experimentally. Measurement of specimens at microscale (or nanoscale) is demanding; not only it is difficult to handle them but there is also a series of new problems caused by the unusually small size. The challenges include the ability to measure the geometrical features of test structures and relative displacements (strain) accurately, to apply a small force (μN or mN range) to test structures, and to make a good alignment between applied forces and test structures. In addition, small imprecision in the setup, which has negligible consequences for macroscale measurement, can be a major source of systematic measurement error for microsamples. In previous work, significant

efforts were focused on improving the measurement techniques and sample preparation methods. Several main techniques for mechanical property and reliability measurements are summarized below:

a) **Beam-bending test:** The test structure for beam-bending test is usually a simple cantilever beam with one end fixed. A small force is applied to the free end of the cantilever yielding a vertical deformation large enough to be measured using optical microscopy, as shown in Figure 1.5 [39]. A doubly clamped beam can also be utilized in the bending test. Compared to a cantilever, a doubly clamped beam is stiffer and more robust. A surface profilometer was used to trace the shapes of fixed-fixed beams at various load settings [40]. By comparison of measured traces and using a finite element analysis (FEA) of the structures, the Young's modulus can be obtained. The advantages of the beam-bending test are that it is simple and is not affected by slight misalignments in the loading direction. Therefore, micromachined samples can be prepared without considering how to accommodate the loading. However, the difficulty of this method is the measurement of such a small applied force.
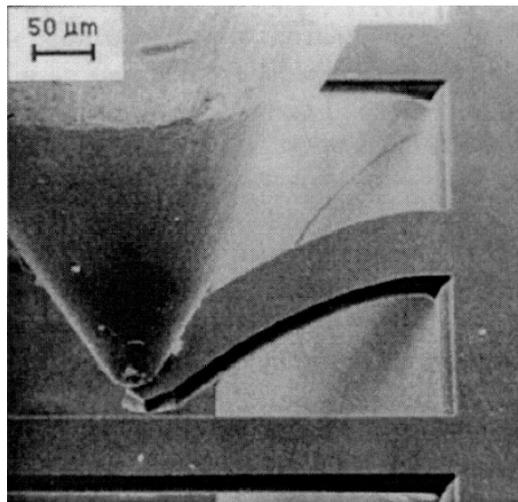
Figure 1.5: A cantilever deflected out of plane by a stylus.

b) **Indentation test:** A probe-based nanoindentation system with a load and a displacement resolution better than 0.01 μN and 0.1 nm, respectively, has been extensively utilized to characterize the mechanical properties of thin film materials [41]. Basically, this system is a miniature and highly sensitive hardness tester. An indenter tip is brought in contact with the test structure, possibly damaging the test structure. Hardness and Young's modulus are then calculated from the load-displacement curve. The Young's modulus measured by nanoindentation is usually higher than from other tests where the large pressure of the indentation tip is the probable cause [42]. Careful modeling regarding deformation of the indentation tip during measurement is required to obtain accurate measurement results.

c) **M-test:** M-test is a widely used method to determine the Young's modulus and residual stress of doubly clamped beams [43]. A voltage is applied between a conductive polysilicon beam and the substrate to pull the beam down as shown in Figure 1.6, where pull-in voltage is a measurement of its stiffness. The advantage of this method is that the measurements can be made entirely with electrical probing in a manner similar to that used to check microelectronic circuits. This provides the opportunity for process monitoring and quality control. The disadvantages are that
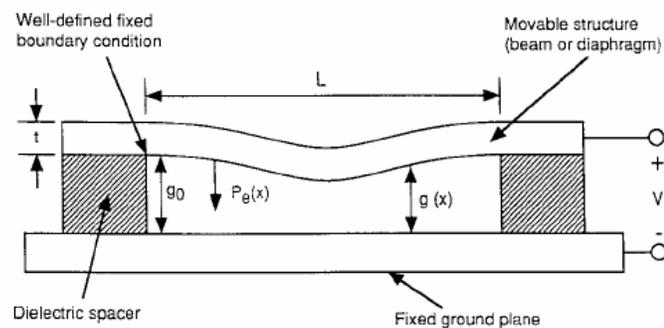
Figure 1.6: Schematic cross-section of the M-test.

only conductive materials are suitable for this technique and the strict requirement of a flat beam before testing.

d) **Direct tension test:** The concept of direct tension test is rather simple: a test structure is loaded in axial tension until it breaks. Direct tension test is an effective method to measure the mechanical properties and the measured data can be easily interpreted. However, the requirements for strain measurement and sample alignment are stringent. Atomic-force microscopes (AFM) [44], image-correlation methods [44], and optical interferometry [45] have been used to measure such a small displacement. On the other hand, the loading system is usually incorporated in the specimen preparation step to solve the alignment problem. An effective way of handling thin film specimens, which is a specimen suspended across a rectangular frame, was introduced [46]. The suspended specimen was released by etching of the backside of the wafer and can be handled easily to be placed into a test machine. A specimen fixed to the die at one end and gripped with an electrostatic probe at the other end is also adopted for sample holding [47] to meet the alignment requirement.

e) **Bulge test:** A thin membrane fabricated by etching away the substrate is pressurized and the measured deflection can be used to determine the biaxial modulus. An advantage of this approach is that the tensile residual stress in the membrane can be measured. However, the value of the Poisson's ratio must be assumed and an analytical model is required. The need to assume a value of the Poisson's ratio was eliminated by testing rectangular silicon nitride films with different aspect ratios [48]. More recently, a similar approach to measure Young's modulus and the Poisson's ratio of polysilicon was developed [49].

f) **Resonant test:** The resonant structure concept was introduced in 1979 by fabricating arrays of thin, narrow cantilever beams of various lengths with composite structures extending over an anisotropically etched pit in the substrate [50]. The beams were excited by variable frequency electrostatic attraction between the substrates and the beams, and elastic properties of the composite structure can be determined from the measurement of the resonant frequency. The test structures used in resonant tests can be very small, which makes this approach suitable for on-chip testing with appropriate actuation designs.

g) **Fatigue test:** Many fatigue tests have been done directly on MEMS devices, such as digital mirrors, instead of the more basic fatigue tests on the materials. Since MEMS devices are usually designed to reduce the stress intensity during operation, these tests only prove that they can operate for millions (or billions) of cycles but no information for fatigue properties of the materials is obtained. However, the fatigue property is one of the important parameters when designing MEMS devices, especially when reliability is emphasized. A circular comb drive actuator with a small notch [51] is one of the few test devices that have been reported to study fatigue mechanisms of polycrystalline silicon thin films as shown in Figure 1.7. This device consists of a notched specimen, a resonant mass (A in Figure 1.7), a capacitive displacement transducer (B in Figure 1.7), and an electromechanical load frame (C in Figure 1.7). Similar to M-test, this technique is only applicable to conductive materials. Therefore, it can not be used to study fatigue properties of silicon nitride thin films.
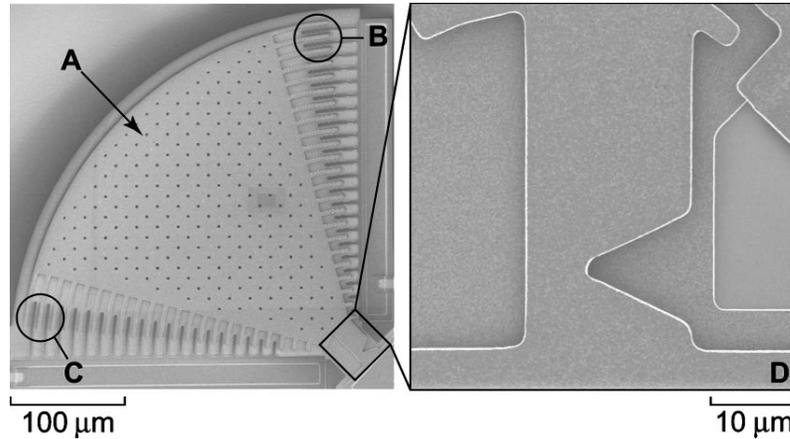
Figure 1.7: Scanning electron micrographs of a circular comb drive with a small notch for fatigue study.

1.4 Research objectives and thesis organization

From the literature review, no mechanical properties and reliability of MEMS-based thin film materials at cryogenic temperatures have been reported. Current techniques were developed for characterizing these materials in room-temperature or high-temperature environments and the measurement data cannot be used in the design of MEMS devices for space applications.

The objectives of this thesis are to develop new test devices and measurement techniques to characterize mechanical properties and reliability of MEMS-based thin film materials and devices at cryogenic temperatures. This thesis focuses on the study of LPCVD silicon nitride thin films, which are the structural materials utilized in the microshutter array (MSA) in the James Webb Space Telescope. The measurement results will provide not only a comprehensive understanding of mechanical behavior and reliability issues of MSA at room temperature and in the outer space environment, but also design guidelines of MEMS devices for other space and/or cryogenic applications.

This chapter has given an introduction to the goals of this research, and the relevant background technologies. The current developments of the MSA and techniques for mechanical property and reliability characterization were reviewed and emphasized to highlight the requirement of new technologies for understanding the mechanical behaviors of MEMS devices at cryogenic temperatures. The organization of the remaining chapters is as follows.

Chapter 2 discusses the design and implementation of a cryogenic measurement setup to emulate the operational environment of outer space. This setup is installed inside a focused-ion-beam (FIB) system, which can provide several unique capabilities including ion milling, ion-induced metal deposition, and *in situ* scanning electron microscopy (SEM). The techniques to adjust and measure temperatures of this setup are also described.

Chapter 3 starts with the design and fabrication of T-shaped cantilevers. Resonant and bending tests of T-shaped cantilevers are performed to characterize the Young's modulus, the Poisson's ratio, and the fracture strength of silicon nitride thin films. Experimental techniques, ANSYS finite element analysis (FEA) models, and the measurement results of the Young's modulus, the Poisson's ratio, and the fracture strength are presented.

Chapter 4 focuses on a new test device – a microgauge sensor - to characterize residual stress and coefficients of thermal expansion (CTE) for silicon nitride thin films. Analytic models based on beam analysis theory are then developed, followed by the discussion of CTE values at cryogenic temperatures.

In chapter 5, a novel test device – the so-called "mechanical-amplifier actuator" – is developed for fatigue study of silicon nitride thin films. An amplification mechanism for

mechanical movement is described in the design of mechanical-amplifier devices. Critical fabrication processes such as the creation of a vertical etch-through sidewall using deep reactive ion etching (DRIE) are then discussed. Experimental techniques and the fatigue test results are presented at the end of this chapter.

In chapter 6, a modified mechanical-amplifier actuator is designed and fabricated to perform tensile test on nano-scale test samples. This design extends applications of mechanical-amplifier actuators to characterize nano-scale thin film materials and to understand the variation of mechanical properties in micro- and nano- dimensions.

The primary test results and accomplishments of this thesis research are summarized in chapter 7.

1.5 Contributions

This thesis focuses on the study of mechanical properties and reliability of thin film materials at cryogenic temperatures. The most important and salient contributions of this research project include:

a) **Experimental setup:** a cryogenic measurement setup emulating the environment of outer space is designed and implemented inside a FIB system. The combination of the FIB system with the setup provides several unique capabilities and they are listed below:

- Precise temperature control down to $20 \, \mathrm{K}$,

- Actuation capability to actuate test devices,

- Measurement capability (SEM image, and secondary electron signal) to measure the response of test devices.

b) **Experimental techniques:** FIB-based experimental techniques are developed for the first time in this thesis that includes the following:

- *In-situ* mechanical property measurement in a FIB system,
- Use of secondary electron signal to measure vibration frequency of a test device,
- A milling mass approach to determine effective thin film thickness,
- Use of a micro-needle as a ground electrode to actuate a test device,
- A post-fabrication micro-repair technique for MEMS devices.

c) **Device design, modeling, and fabrication:** several unique test devices are developed to understand the mechanical behavior of thin film materials at cryogenic temperatures. These include:

- T-shaped cantilevers,
- High-sensitivity microgauge sensors,
- Mechanical-amplifier actuators,
- Modified mechanical-amplifier actuators.

d) **Experimental results:** we report the mechanical properties and reliability of LPCVD silicon nitride thin films at cryogenic temperatures for the first time. The measurement results provide important design parameters of MEMS devices for space and/or cryogenic applications, and they are summarized below:

- Young's modulus, Poisson's ratio, fracture strength, coefficient of thermal expansion, and fatigue property at room and cryogenic temperatures,
- Average and local value of residual stress after nitride deposition,
- Amplification of tiny residual/thermal strain ($\sim 5\mu\varepsilon$) using the microgauge sensors,
- Demonstration of the mechanical-amplifier actuators.

CHAPTER 2

CRYOGENIC MEASUREMENT SETUP IN A FOCUSED-ION-BEAM SYSTEM

The word *cryogenics* is usually defined as the study of low-temperature phenomena; however the temperature level at which *cryogenics* begins is ambiguous. One definition given by the National Institute for Standards and Technology suggests that *cryogenics* covers temperatures below 123 K (-150 °C), since the normal boiling points of the so-called permanent gases, such as helium, hydrogen, nitrogen, neon, and oxygen are lower than this temperature. As discussed in Chapter 1, the microshutter array in the James Webb Space Telescope must operate in a cryogenic vacuum environment reliably over a 10 year mission life without repair after launch. Therefore, a cryogenic apparatus for testing the microshutter array is required to understand the device performance and reliability in the cryogenic operating environment.

This chapter presents a cryogenic measurement setup installed inside a focused-ion-beam (FIB) system to study mechanical properties and reliability of the microshutter array [52, 53]. The detailed design, realization, and characterization of each component utilized in this setup are described. A thin-film thermo-resistor with a meander structure, designed by Tomas Luger, is utilized as an integrated temperature sensor for temperature measurement. The capability to test MEMS materials and devices under vacuum at variable temperatures (from 298 K to 20 K) are demonstrated. At the end of this chapter, a micro-repair technique for the microshutter arrays and stress analysis of multilayer structures based on the entire measurement system are also discussed.

2.1 Requirement of a cryogenic measurement setup

The goal of this research project is to understand the mechanical behavior and reliability of MEMS devices for space applications. Therefore, a cryogenic measurement setup to emulate the environment of outer space is needed. The design criteria for this setup are: (a) a cryogenic vacuum environment with temperatures less than 30 K; (b) a method to obtain accurate temperature measurement; (c) implementation of an actuation system; and (d) development of *in-situ* measurement techniques. In addition, an electrical interface for signal connection and mounting of test chips in this setup should be simple. Since a FIB system provides several unique capabilities, the cryogenic measurement setup is designed to be installed inside this system.

2.2 Introduction of a focused-ion-beam system

The FIB technique was mainly developed during the late 1970s and modern FIB systems are becoming widely used in semiconductor research and processing environments, as well as in failure analysis and chip-design centers. The technology enables localized milling and deposition of conductors and insulators with high precision; hence it can be utilized in device modification, mask repair, process control and failure analysis [54, 55] . Also, the preparation of specimens for transmission electron microscopy (TEM) [56] and the trimming of thin-film magnetoresistive heads for magnetic storage disks [57] are important applications of the FIB. Recently, the fabrication of microstructures of various geometries and prototype nano-scale devices [58] has been successfully demonstrated using FIB systems, which extends this technique into MEMS research.

The FEI 620 FIB system used in our experiment is a dual beam vacuum system, with ion and electron columns. When energetic ions coming from the ion column hit the surface of a solid sample, they lose energy to the electrons and atoms of the solid. Three important physical effects of incident ions on the substrate can be used for ion milling, ion imaging, and platinum deposition [59-61]. Sputtering of neutral and ionized substrate atoms enables mask-less substrate milling (or ion milling), and secondary electrons emitted from the substrate are collected on a biased detector or a multichannel plate (MCP) to form the image. In the FEI 620 FIB system, there is a fine needle with trimethyl platinum precursor gas, which can be sprayed and absorbed on the surface of the substrate. The incident ion beam decomposes the absorbed precursor gas; then the volatile reaction products desorb from the surface and are removed through the vacuum system, while platinum is deposited on the surface as a thin film. The principles of ion milling, ion imaging, and platinum deposition are shown in Figure 2.1 [54]. In addition, electron beams coming from the electron column of this system can provide *in-situ* scanning electron microscopy (SEM) function. The FEI 620 FIB system with the cryogenic measurement setup installed inside is shown in Figure 2.2.

(a)   (b)   (c)
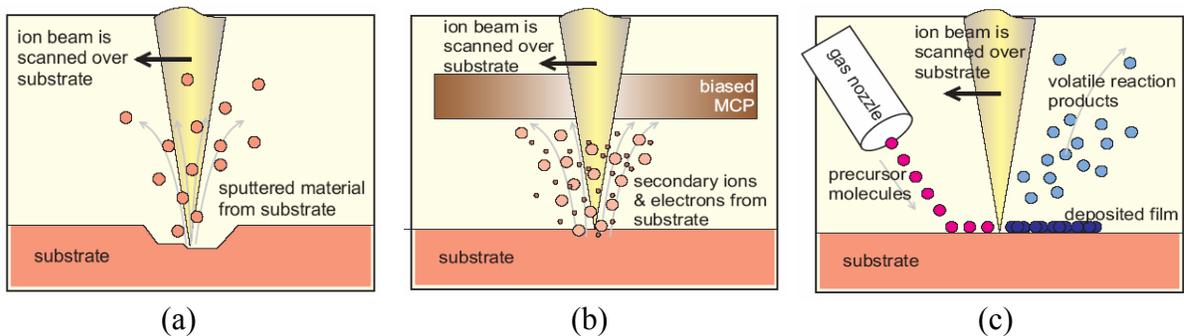
Figure 2.1: Principles of a FIB system: (a) ion milling, (b) ion imaging, and (c) platinum deposition [54].

25
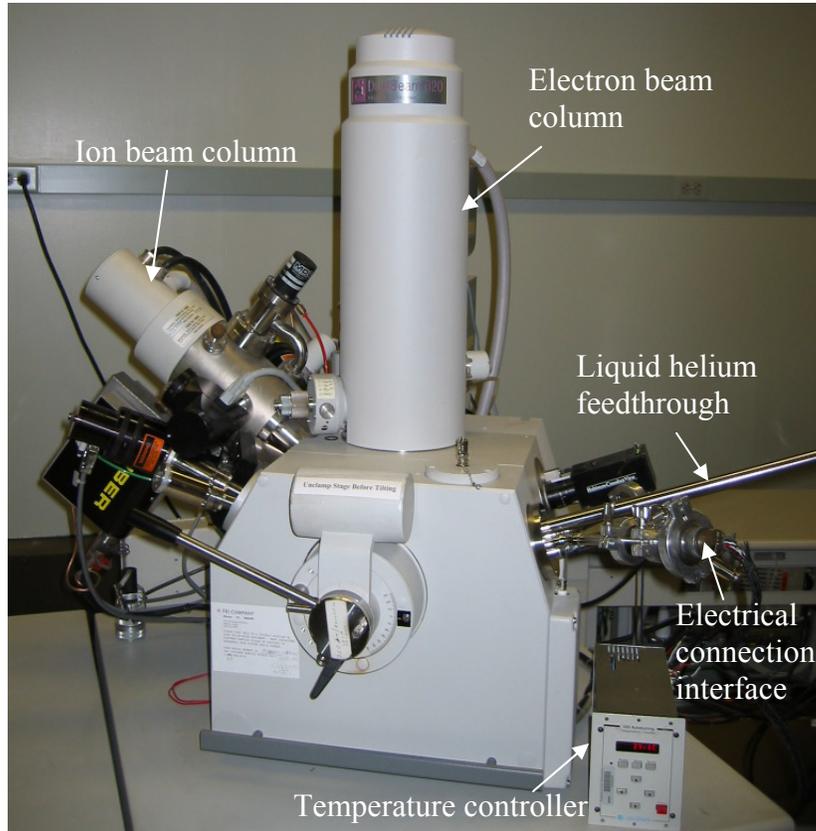
Figure 2.2: FIB system with a cryogenic measurement setup installed inside. The helium transfer tube connecting liquid helium feedthrough and liquid helium dewar is not shown in this figure.

2.3 Design and implementation of the cryogenic measurement setup

The cooling process of the cryogenic measurement setup relies upon evaporation of a liquefied gas. Table 2.1 lists the boiling points of several liquefied gases at one atmosphere [62]. Since the desired temperature is 30 K and hydrogen requires more safety concerns during experiments, liquid helium (^{4}He) was selected as the cooling source for this setup. A liquid helium feedthrough with an electrical connection interface was designed to fit the port of the FIB system. In order to transfer liquid helium between

the feedthrough and a helium dewar, a flexible helium transfer tube with multiple radiation shields and vacuum insulation were adopted [63].

Table 2.1: The boiling points of common liquefied gases used in low-temperature experiments.

	^{3}He	^{4}He	H_2	N_2	O_2	C_2H_4
T_{bp} (K)	3.20	4.22	20.39	77.35	90.30	169.50

Figure 2.3 shows the configuration of the cryogenic measurement setup inside the FIB system. Liquid helium in combination with a commercial resistive thermal source [64] is used to control the temperature of the device stage by adjusting the flow rate of liquid helium (coarse tuning) and the electrical current flowing through the resistor (fine tuning). Since the cryogenic measurement setup operates at temperature levels much below ambient environment, heat transfer is the main concern when designing such a setup, and therefore, a thermally isolated device stage with cooling power is required. In our design, the cooling power is provided by a helium diffuser connected to a thermally isolated device stage (rotate-able and tilt-able) with a flexible wire providing a thermal path. As copper has high thermal conductivity and can be machined easily, the device stage, the helium diffuser and the thermal path are made from copper.

One challenge for designing this setup is to obtain a thermally isolated device stage by minimizing heat transfer between the device stage and other components. Hence, the cryogenic heat transfer needs to be understood. The main heat transfer mechanisms at 30 K are conduction, convection, and radiation [65]. In general, conduction heat transfer can be expressed by the Fourier rate equation:

(a)

(b)

(c)
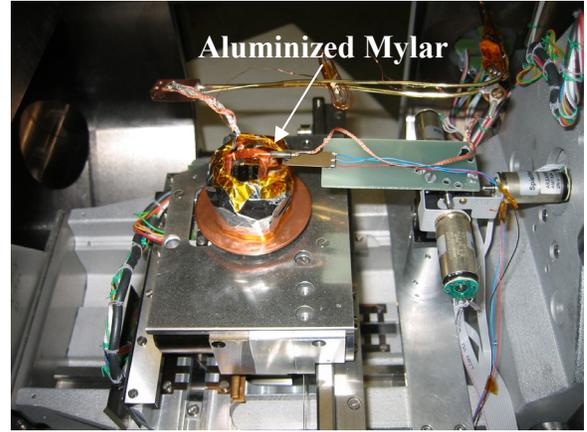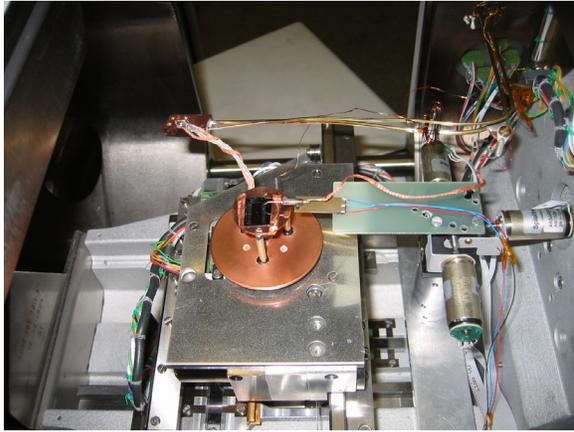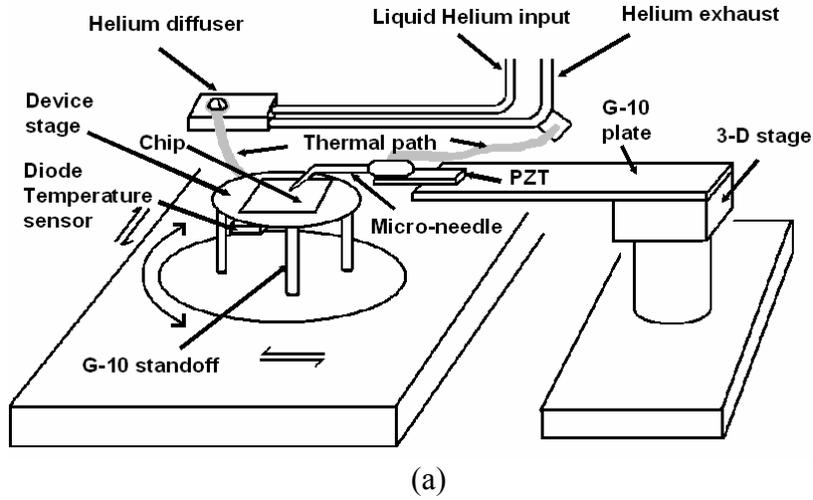
Figure 2.3: Configuration of the cryogenic measurement setup inside the FIB system: (a) schematic view, (b) photograph of the system without Mylar shield, and (c) photograph of the system with Mylar shield.

$$Q = -k_t A \cdot \nabla T \qquad (2.1)$$

where Q is heat transfer rate (W), k_t is the thermal conductivity (W/m-K), A is the area (m^2), and T is the temperature (K). Conduction heat transfer can be reduced by using thermal insulating materials (low thermal conductivity) with small contact area. In the realization of the thermally isolated device stage, three hollow G-10 (a continuous filament glass cloth material with an epoxy resin binder) standoffs were used as thermal insulators (thermal conductivity of 0.04 W/m·K at 30 K) to minimize conduction heat

transfer between the device stage and the FIB chamber. Due to a high vacuum ($<10^{-6}$ torr) inside the FIB system, convection heat transfer can be neglected.

However, in most cryogenic setups, the primary mode of heat transfer is radiation heat transfer. The Stefan-Boltzman law indicating the total amount of heat radiated from a nonreflective emitting surface can be expressed as [66]

$$Q = \varepsilon_T \sigma A T^4 \qquad (2.2)$$

where Q is the heat transfer rate (W), ε_T is the emissivity (dimensionless correction factor for how closely a given material approximates the characteristics of an ideal blackbody radiator), σ is the Stefan-Boltzman constant (5.67032×10^{-8} W/m^2·K^4), T is the temperature in K, and A is the area. In our design of the radiant shield, three layers of aluminized Mylar [62] enclosing the device stage were utilized to reduce radiation heat transfer because of the lower emissivity of aluminized Mylar compared with that of stainless steel/aluminum oxide chamber wall. Additionally, there is no thermal conduction path between the Mylar shield and the device stage.

A diode temperature sensor [67] attached to the device stage, with thermal response time of 10 ms at 4.2 K and accuracy of 0.25 K at 30 K, was first utilized to measure the temperature of the chip. The temperature reading and calibration were obtained from a commercial temperature controller [68]. However, the temperature of a device chip may be different from the one measured by the diode temperature sensor as a result of thermal resistance between the device chip and the device stage. In addition, radiant heat transfer is not zero since the device stage is not wholly enclosed by aluminized Mylar layers. An opening must be used for the entrance of electron and ion beams. To obtain an accurate temperature measurement, a temperature sensor integrated on the device chip is required.

There are several techniques used to design temperature sensors, such as the measurement of thermo-electric effect, thermo-mechanical effect, temperature dependence of electrical conductivity, and voltage-current (V-I) behaviors of diodes and transistors [66]. In designing an integrated temperature sensor for our purpose, two issues need to be considered: First, the fabrication steps of this temperature sensor should be compatible with fabrication processes of the test devices. Second, the interconnection strategy should be simple. A thin-film thermo-resistor with a meander structure was designed as an integrated temperature sensor with test devices (Figure 2.4) due to its simplicity. In the material selection for the integrated temperature sensor, metal thin films are good candidates since the resistances of most metals decrease with temperatures and have a unique response. Here, chromium/gold metallization with the thickness of 5 nm and 50 nm, respectively, was utilized as the structural layer of this thin-film thermo-resistor since these two metal layers were also used in the fabrication of test devices. In the dimension design of the integrated temperature sensor, the meander structure was used to increase resistance value and sensitivity. The overlap length of the conduction path is 102 mm with a line width of 25 μm (Figure 2.4). The expected variation of the resistance value from 298 K to 30 K is 1.5 kΩ if the resistivities of gold are assumed to be 2×10^{-8} Ω-m at 298 K and 7×10^{-10} Ω-m at 30 K [69], respectively. The interconnection was made using low-temperature conductive epoxy to connect the bonding pads of the integrated temperature sensor with manganin wires.
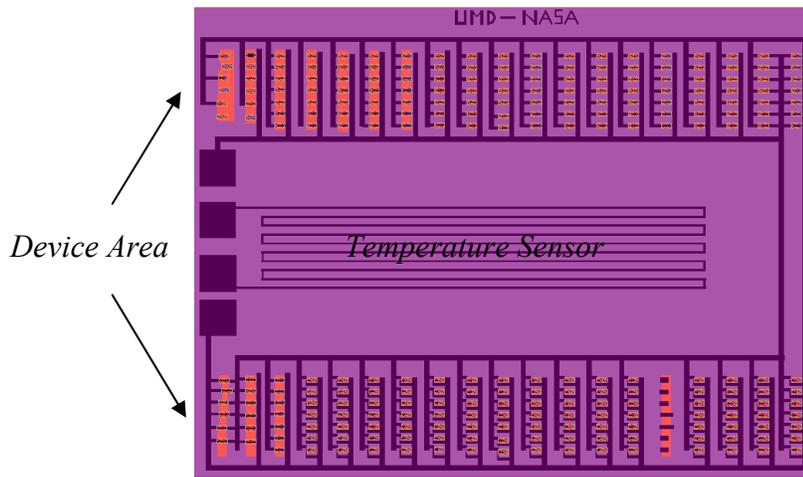
Figure 2.4: Layout design of an integrated temperature sensor in the center of a test chip. The area of the integrated temperature sensor is 5 mm × 10mm.

For actuating test devices, a lead-zirconate-titanate (PZT) translator, powered by a function generator and a DC voltage, was attached to a G-10 plate with a stycast epoxy [70]. The G-10 plate was then fixed on a 3-D stage controlled by three stepper motors. A small G-10 tube (10 mm in length, 3.5 mm in diameter, and 0.6 mm in wall thickness) with a thin metal layer at its inner surface was attached on the top surface of the PZT translator. A micro-needle was mounted to the metal part at the end of this tube, which can be positioned with high accuracy to a few nanometers by using the PZT translator and the 3-D stage. A flexible copper wire (thermal path) cooling the micro-needle was soldered to the metal part of the G-10 tube. This configuration prevents the PZT translator from malfunction as it remains warm during cryogenic operation of the micro-needle.

31

2.4 System characterization

A copper block attached to the helium diffuser inside the FIB chamber was designed and machined to calibrate the integrated temperature sensor, as shown in Figure 2.5. Both the diode temperature sensor and the integrated temperature sensor were placed next to each other in the copper block. Since copper is a good thermal conductor and the FIB is a high vacuum system, the temperature difference between these two sensors is assumed to be negligible. As the temperature decreased, the temperature was recorded from the diode temperature sensor, while resistance was determined from the integrated temperature sensor. Thus, the relationship between temperature and resistance was obtained (Figure 2.6). From the measurement result, the resistance of the integrated temperature sensor decreases linearly when cooling down to 20 K with an average sensitivity of 7.85 Ω/K due to fewer collisions of conduction electrons with lattice phonons in the chromium/gold thin films at cryogenic temperatures. No hysteresis of resistance was observed during the cooling and warm-up cycles (the difference is less than 1Ω at a specific temperature).
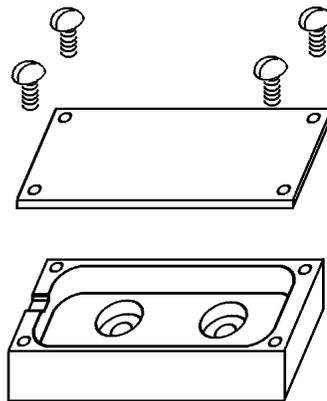
Figure 2.5: Schematic view of the copper block for calibration of the integrated temperature sensor.
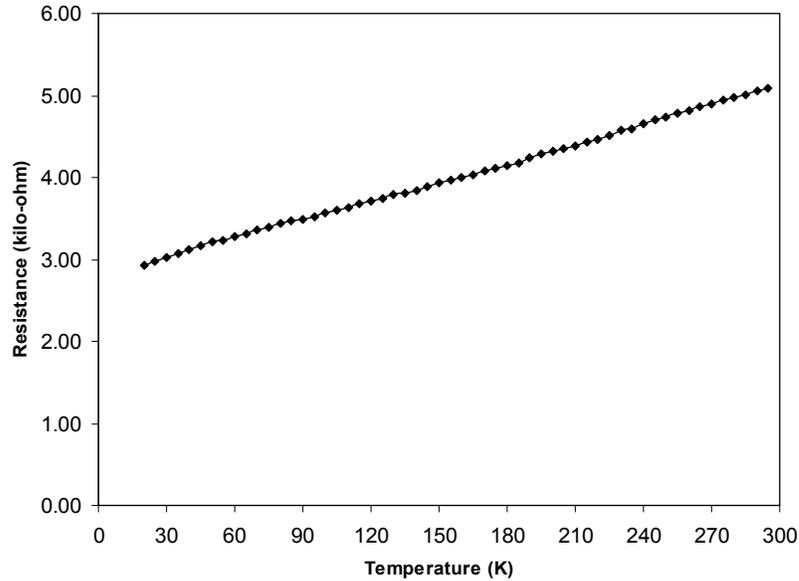
Figure 2.6: Resistance-temperature curve of the integrated temperature sensor. The resistance of the integrated temperature sensor decreases linearly when cooling down to 20 K with an average sensitivity of 7.85 Ω/K.

The accurate temperature measurement of the device chip can then be obtained by using the calibrated integrated temperature sensor. In order to characterize the cryogenic measurement setup, the integrated temperature sensor was attached on the device stage as the temperature decreased. The two diode temperature sensors mentioned previously were utilized to monitor the temperatures of the device stage and the helium diffuser, respectively. When the temperature of the integrated temperature sensor was set to 30 K by adjusting the flow rate of liquid helium, the temperatures of the device stage and the helium diffuser were measured to be 22.6 K and 4.2 K. The equivalent thermal model of the cryogenic measurement setup is presented in Figure 2.7. Here, the values of 0.015 J/g·K at 25 K, 0.0025 J/g·K at 14.4 K, and 0.00015 J/g·K at 4.2 K [71] were used as the specific heat of copper in the calculation of heat capacity, defined as the quantity of heat required to raise the temperature of a substance one degree (K or °C). In addition, the

33

temperature of the copper cable is assumed to be 13.4 K, the average value of the device stage and the helium diffuser.

From the thermal model shown in Figure 2.7, the temperature difference between the device chip and the device stage is only 7.4 K and it is mainly caused by a thermal resistance in between. The thermal capacity of the device stage is two orders of magnitude higher than that of the helium diffuser. Although the device stage with higher heat capacity requires longer time to cool down, it provides a more stable thermal environment once reaching the desired temperature.
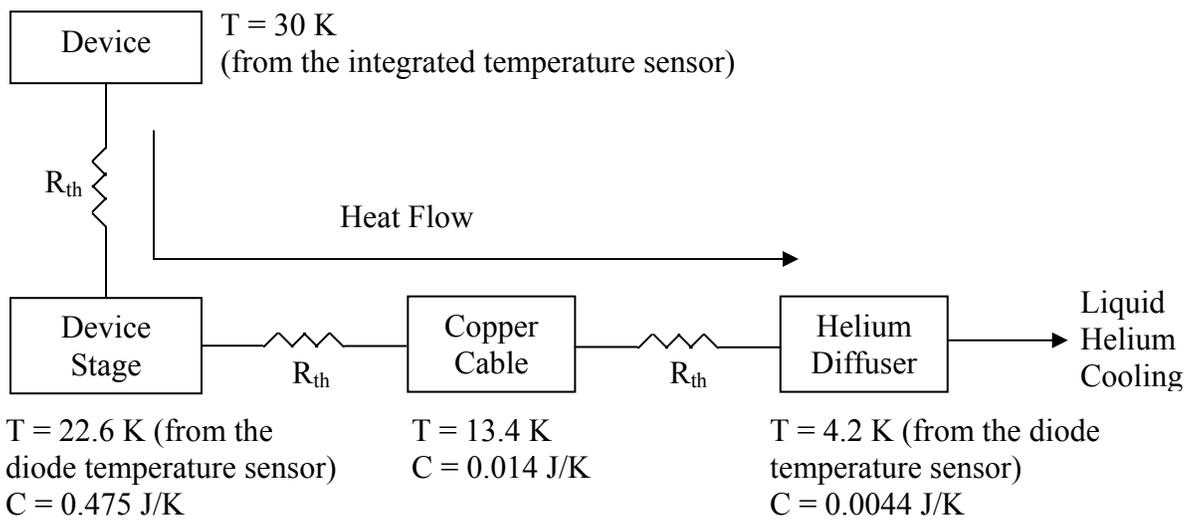
Figure 2.7: Equivalent thermal model of the cryogenic measurement setup. Thermal capacity C and temperature T of each component are given at cryogenic temperatures. R_{th} represents thermal resistance.

2.5 Two applications of the cryogenic measurement setup

A. Micro-repair technique for the microshutter arrays

As mentioned in Chapter 1, the microshutter arrays are currently being developed as programmable field selectors on NASA's James Webb Space Telescope. Individual shutter elements consist of a shutter blade of low-stress LPCVD silicon nitride suspended

from the shutter frame by a nitride torsion flexure. The key requirement of the microshutter array is to provide high on-to-off contrast ratio greater than 2000:1 at 30 K. However, the limitation of fabrication techniques makes this requirement difficult to achieve. Even though the microshutter array is fabricated using microfabrication techniques with a yield over 99%, in order to obtain such a high contrast ratio, broken elements in the array after fabrication must be blocked to keep them in the permanently closed state.

A technique to block a broken microshutter window was developed using the cryogenic measurement setup and the FIB system. The experimental procedure of this technique is as follows: The micro-needle is brought into contact with an appropriate membrane which will be utilized to block the broken window. Here, the same shutter element is used as the membrane from a testing chip for this purpose and the microshutter devices on this testing chip were fabricated without light shields (see Chapter 1 for detail). Ion-induced platinum deposition is performed to weld the micro-needle to the membrane. Next, the micro-needle with the membrane is released as a free structure by using ion milling to separate the connection between the membrane and substrate. The micro-needle with the membrane is positioned to the light shield of a broken window, followed by ion-induced platinum deposition to weld the membrane to the light shield. Finally, the connection between the micro-needle and the membrane is removed by ion milling. In this experiment, the motorized 3-D stage and the PZT translator provide the freedom to move the micro-needle with high resolution (few nanometers). Figure 2.8 shows the scanning electron micrographs summarizing the experimental steps.

The optical test of the microshutter array with blocked windows is performed, which

shows promising results with one order of magnitude higher than the required contrast ratio. This demonstrates that the micro-repair technique is useful to increase the contrast ratio after fabrication. The only disadvantage is that this technique is a slow process and can be applied to only one element at a time.

(a)

(b)

(c)

(d)
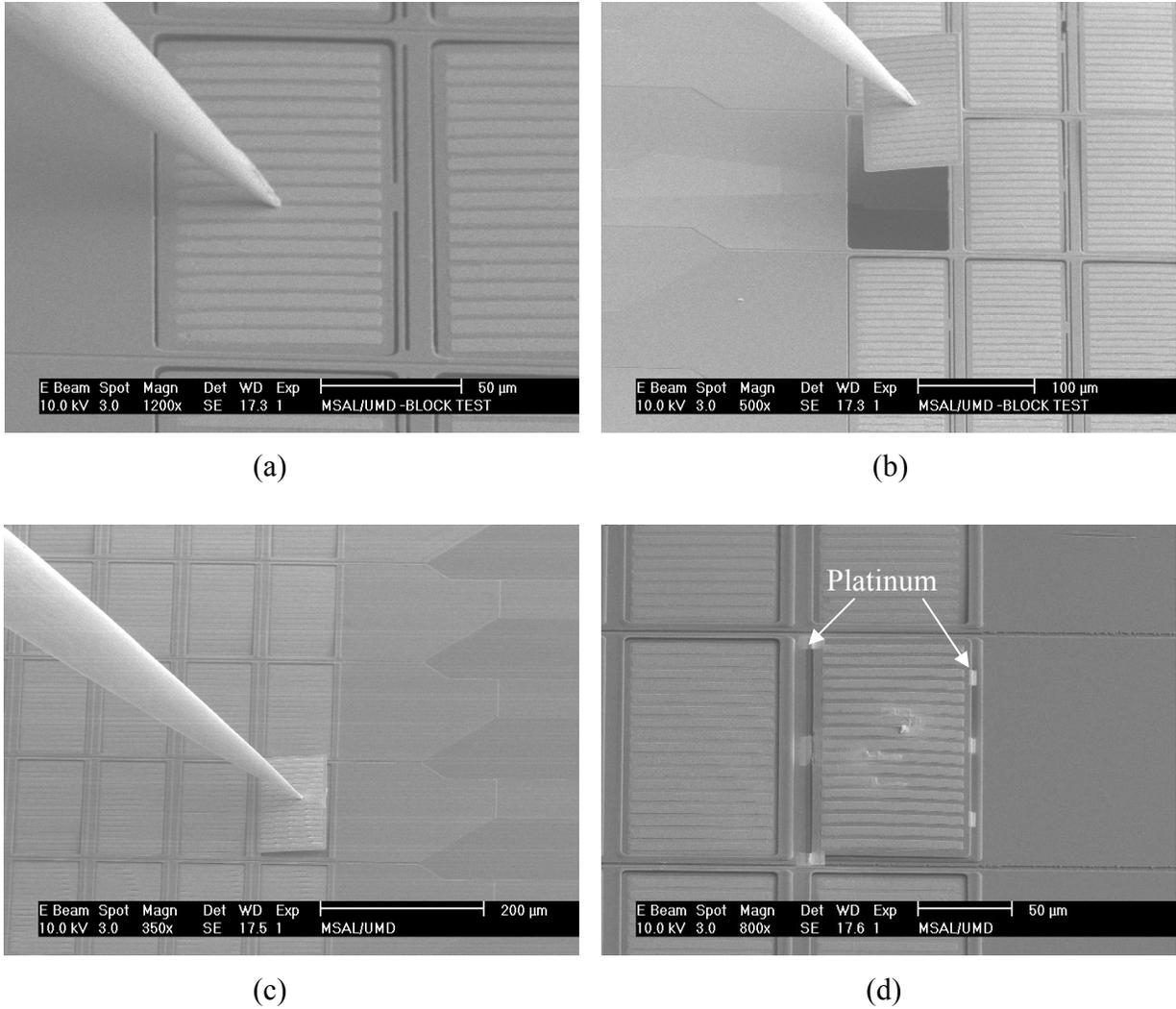
Figure 2.8: Micro-repair for blocking test of a microshutter array: (a) the micro-needle is placed into contact with a membrane utilized to block a broken shutter element. Ion-induced platinum deposition is then performed to weld the micro-needle with the membrane. (b) the micro-needle with the membrane is released by ion milling the connecting part of the membrane to the substrate, (c) transport the membrane to the position of the broken shutter element, and (d) the membrane is welded with the broken shutter window using platinum deposition. Finally, the micro-needle is released from the membrane by ion milling.

B. Stress analysis of multilayer structures

The microshutter arrays are optical MEMS devices operating in outer space. In order to prevent leakage light at the closed state of shutter elements, these devices require flat surfaces. As the structural layers of microshutter devices are low-stress LPCVD silicon nitride, aluminum, and cobalt/iron, the surfaces curl up 12 μm at 30 K as shown in Figure 2.9 according to the cooling test using the cryogenic measurement setup. The curvature is mainly caused by the mismatch of the coefficients of thermal expansion (CTE) among these three layers.

Since the residual stress of thin film materials is sensitive to fabrication processes, one possible solution without dimensional modification of shutter elements is to tune parameters in microfabrication steps. The principle is to compensate the thermal stress at 30 K with induced residual stress during fabrication. The sputtering process of cobalt/iron deposition has been varied to obtain compressive residual stress and to intentionally curl down the shutter blade at room temperature as shown in Figure 2.10. In this figure, the patterns of cobalt/iron are also modified as strip structures to prevent unwanted lateral movement of the shutter blades during magnetic actuation. However, when cooling down the microshutter arrays using the cryogenic measurement setup, the shutter elements still curl up 4.5 μm at 30 K as a result of insufficient thermal stress compensation.

A high sensitivity microgauge sensor for residual stress and CTE measurement at cryogenic temperatures is developed and will be discussed later in Chapter 4. The values of the residual stress and the CTE for each layer of the microshutter arrays are acquired using the microgauge sensor. Further stress analysis based on these measurement results can lead to evaluate required compensated stress values, which can be achieved by

process tuning or utilizing additional layers to obtain stress balancing of these multilayer

structures.
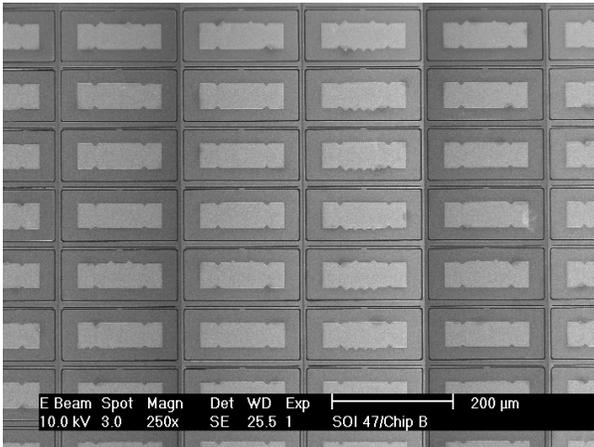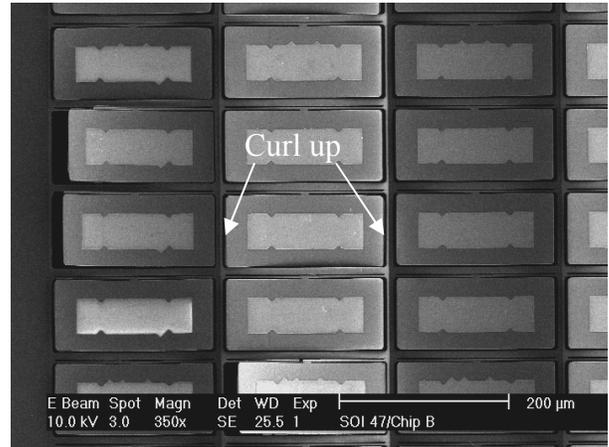
(a)   (b)

Figure 2.9: Scanning electron micrographs of a microshutter array at (a) 298 K and (b) 30 K. The surface of the shutter element curls up at 30 K due to the mismatch of the coefficients of thermal expansion of the structural layers.
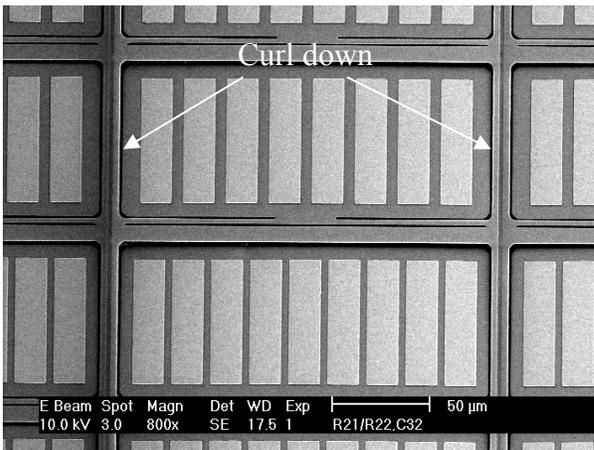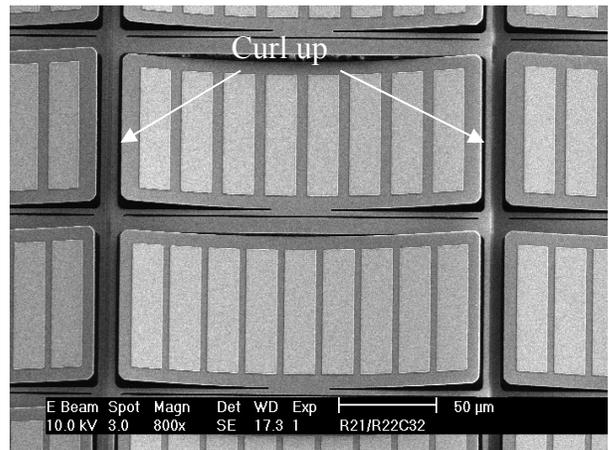
(a)   (b)

Figure 2.10: Scanning electron micrograph of a microshutter element with a curl-down surface at (a) 298 K and (b) 30 K. The shutter elements still curl up 4.5 µm at 30 K as a result of insufficient thermal stress compensation.

2.6 Summary

A helium-cooled cryogenic measurement setup installed inside a FIB system is developed, which is capable of providing cryogenic temperatures down to 20 K. A thin-film thermal resistor with a sensitivity of 7.85 Ω/K is fabricated with test devices as an integrated temperature sensor and a micro-needle attached on a PZT translator is utilized to actuate test devices and transport membranes. A micro-repair technique for the microshutter arrays and stress analysis of multilayer structures based on the designed setup are discussed. The following chapters are focused on the characterization of mechanical properties and reliability of LPCVD silicon nitride thin films using the developed cryogenic measurement setup.

CHAPTER 3

MECHANICAL PROPERTY CHARACTERIZATION OF LPCVD SILICON NITRIDE THIN FILMS

It is essential for MEMS designers to know mechanical properties of different materials at the micro-scale for the anticipated operating environment, as most mechanical properties are known to depend on specimen size [38] and temperature [72]. Mechanical properties of interest fall into three general categories: elastic, inelastic, and strength. Elastic properties allow designers to predict the amount of deflection from an applied force, or vice versa. If the material is ductile and the deformed structure does not return to its initial state, then the inelastic material behavior is necessary. The strength of the material must also be known so allowable operating limits can be set to avoid fracture.

LPCVD silicon nitride thin films, previously functioning as oxidation masks and as gate dielectrics in combination with thermally growth SiO_2 in the IC industry, have been utilized to fabricate plates, cantilevers, and membranes [73] for different MEMS applications due to their excellent mechanical, electrical, and thermal properties. However, the mechanical properties of this material are not fully understood, even at room temperature. Table 3.1 presents some mechanical property data of silicon nitride thin films published in the literature. Large variation of these data is observed and is mainly caused by different deposition methods of these thin films. Therefore, it is important to notice that the published mechanical property data can only be used as reference values for initial designs.

Table 3.1 Mechanical property data of silicon nitride thin films.

Young's modulus (GPa)	Fracture strength (GPa)	Poisson's ratio	Coefficient of thermal expansion (µstrain/K)	Residual stress (MPa)	Comment / Reference
270	-	0.27	2.3	+1100	Stoichiometric / [32]
270	-	0.27	2.3	-50 - +800	Silicon rich / [32]
202.57	12.26	-	-	-	Silicon rich / [74]
194	-	-	-	-	[75]

This chapter presents the characterization of Young's modulus, Poisson's ratio, and fracture strength for low-stress LPCVD silicon nitride thin films utilized in the microshutter arrays [76, 77]. By definition, Young's modulus is the slope of the linear part of a stress-strain curve, Poisson's ratio is a measure of the lateral contraction or expansion of a material when subjected to an axial stress within the elastic region, and fracture strength is the normal stress at the beginning of fracture [42]. In this study, new experimental techniques are developed to measure the Young's modulus, Poisson's ratio, and the fracture strength of silicon nitride thin films at cryogenic temperatures using the designed cryogenic measurement setup (discussed in Chapter 2). To increase the accuracy of the measurements, a "milling mass" approach to determine a thin-film thickness, which is a critical parameter of the developed method, has also been proposed and applied in the study of the Young's modulus. Finally, the test results of Young's modulus, Poisson's ratio, and fracture strength are reported at room and cryogenic temperatures.

3.1 Test device design: T-shaped cantilevers

3.1.1 Young's modulus of thin films

In general, it is difficult to measure the Young's modulus of thin films. In static-loading methods, such as tension and bending tests, both the strain and load must be measured precisely. However, these values are extremely small, so accurate measurements require special apparatus, for instance - a laser interferometer. Instead of using the static-loading methods, a resonant technique of T-shaped cantilevers is developed to determine the Young's modulus of silicon nitride thin films. Unlike conventional cantilevers, a mass m_b is added to the end of a cantilever as shown in Figure 3.1 to form a "spring-mass" system whose first resonant frequency can be measured and computed analytically. The advantage of this design is that the resonant frequency of this T-shaped cantilever can be reduced to a range that can be easily measured. From the beam theory, the first resonant frequency of a T-shaped cantilever is expressed as [78]

$$f = \frac{1}{2\pi} \sqrt{\frac{3EI}{L^3(m_b + c_1 m_a)}} \tag{3.1}$$

where $c_1 m_a$ (c_1 is a constant and equal to 0.2357) is the effective mass of the cantilever beam in region A, m_b is the added mass of region B, f is the first resonant frequency in Hz, $L = L_a + L_b/2$ is the effective cantilever length, and E is the Young's modulus. The area moment of inertia I is equal to $(w_a t^3)/12$, where w_a is the width of region A, and t is the thickness of the cantilever. Here, T-shaped cantilevers are modeled as structures under uni-axial stress. This may violate the condition of bi-axial stress at the supporting boundary and lead to error in the expression of the resonant frequency. An ANSYS finite element analysis (FEA) model has been developed to examine this effect. The variation of Young's modulus is found to be only 1.05 % even with the consideration of Poisson's

ratio for the T-shaped cantilever. Therefore, this effect can be neglected.
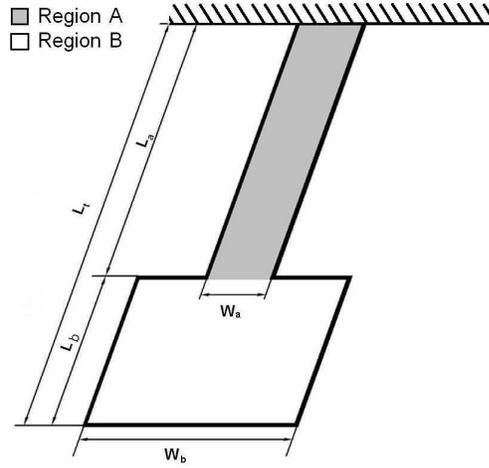
Figure 3.1: Schematic diagram of a T-shaped cantilever for resonant tests.

3.1.2 Poisson's ratio of thin films

The measurement of the Poisson's ratio uses the same resonant technique as discussed in the previous section. However, the T-shaped cantilever (shown in Figure 3.1) is driven at the torsional resonant mode instead of the fundamental mode and this frequency can be expressed as [78]

$$f = \frac{1}{2\pi}\sqrt{\frac{GJ}{L(I_{pb} + \frac{1}{3}I_{pa})}} \tag{3.2}$$

and

$$G = \frac{E}{2(1+v)} \tag{3.3}$$

$$J = (\frac{w_a t^3}{3})(1 - 0.63\frac{t}{w_a} + 0.052\frac{t^5}{w_a^5}) \tag{3.4}$$

43

$$I_{pa} = \frac{1}{12} m_a (w_a^2 + t^2) \tag{3.5}$$

$$I_{pb} = \frac{1}{12} m_b (w_b^2 + t^2) \tag{3.6}$$

where f is the torsional resonant frequency in Hz, $L = L_a + L_b/2$ is the effective cantilever beam, E is the Young's modulus, v is the Poisson's ratio, t is the thickness of the cantilever, m_a is the mass of region A, and m_b is the added mass of region B. Once the torsional resonant frequency is determined, the Poisson's ratio from equation (3.2) is given by

$$v = \frac{EJ}{2L} \frac{1}{(2\pi f)^2 (I_{pb} + \frac{1}{3} I_{pa})} - 1 \tag{3.7}$$

3.1.3 Fracture strength of thin films

For measuring the fracture strength of silicon nitride thin films, bending tests of T-shaped cantilevers are performed. The dimensions of the T-shaped cantilevers used for bending tests (Figure 3.2) are different from those used in the resonant tests. The width and length in region B are selected to be larger than those in region A, such that region B is rigid relative to region A during the bending test. If a force F is applied to a cantilever at a distance L_f from the fixed end, the inclination θ of the end region A (at $x = L_a$) can be expressed as [78]

$$\theta = \frac{F(2L_f L_a - L_a^2)}{2EI} \tag{3.8}$$

where L_a is the length of region A, E is the Young's modulus, and I is the moment of inertial of region A. Equation (3.8) is valid only when θ is small. If L_f is assumed to be

44

nL_a ($L_f = nL_a$), the above equation can be rewritten as

$$\theta = \frac{FL_f L_a}{EI}\left(1 - \frac{1}{2n}\right)$$ (3.9)

Therefore, the maximum moment M about the fixed end of the beam is

$$M = FL_f = \frac{\theta EI}{L_a(1 - \frac{1}{2n})}$$ (3.10)

In the experiment, the large blade of a cantilever (region B) is pushed by a micro-needle through a rotation angle θ. The peak stress occurs at the fixed end and is expressed as

$$\sigma = \frac{Mc}{I} = \frac{\theta Ec}{L_a(1 - \frac{1}{2n})}$$ (3.11)

where c is the half thickness of the cantilever. Since the accurate position and force of the micro-needle applied to the cantilever are difficult to measure, the stress determined from equation (3.11) has the advantage of being insensitive to the force position if n is large, and the value of the applied force is not needed. The maximum bending angle before failure is measured and the fracture strength of the silicon nitride thin film can be obtained.
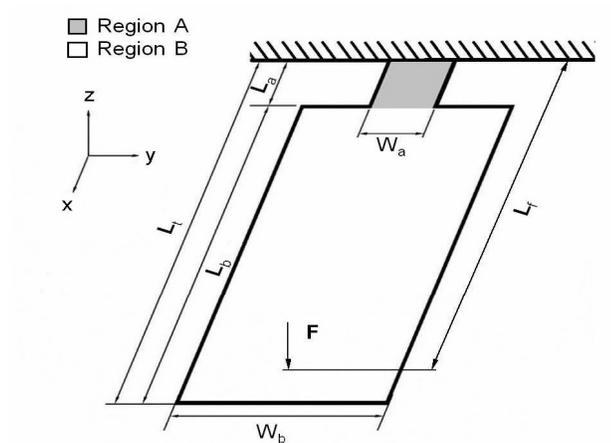
Figure 3.2: Schematic diagram of a T-shaped cantilever for bending tests.

3.2 Device preparation

T-shaped cantilevers were fabricated using bulk micro-machining technique. The basic process flow is shown in Figure 3.3, and specific details are described below. A layer of low-stress LPCVD silicon nitride with an approximate thickness of 0.45 μm and residual stress of 200 MPa was first deposited on a 500 μm thick n-type silicon substrate. In this step, if a p-type silicon substrate is used, the concentration of boron doping can not exceed 5×10^{18} cm^{-3}. Otherwise, the etch rate of silicon in alkaline liquids will reduce significantly [79]. A standard lithography process (Table 3.2) was then performed, and the patterned photoresist was used as a masking layer for silicon nitride etching. The silicon nitride thin film was etched in a reactive ion etcher (Trion^{TM} Minilock RIE System) using CF_4 and O_2. The process parameters were P = 250 mTorr, flow rates of 50 sccm and 5 sccm for CF_4 and O_2, respective, and a RF power of 100 W. The silicon nitride etch rate was 180 nm/min, and the photoresist etch rate was around 80 nm/min. After etching the silicon nitride, the photoresist was removed using a photoresist stripper (Baker Aleg – 625) heated to 45 °C.

Table 3.2: A standard lithography process used in this study.

Step	Recipe
Photoresist coating	Photoresist: AZ 9245 (Clarinet^{TM}) Spin coating: 1750 rpm for 5 seconds, then 3000 rpm for 40 seconds Soft bake: 110 °C for 90 seconds
Exposure	Dose: 300 mJ Contact aligner: Quintel^{TM} Q4000
Photoresist development	Developer: AZ 400 K mixed with DI water (1:3) Developing time: 2 minutes

Next, the wafer was placed into a 20%, 72 °C potassium hydroxide (KOH) solution [26] for 2.5 hours with uniform agitation to release the T-shaped cantilever structures. The etching apparatus sat inside a constant-temperature thermal bath (NESLAB GP-300) with a condenser to keep the concentration of KOH steady. A magnet positioned under the solution beaker along with a magnetic stirring bar in the KOH solution was used to produce uniform agitation (1000 rpm). The etch rate from the experiment was 0.79 μm/min. The depth of the etched v-groove was 118.5 μm and the undercut of silicon (lateral etch) was 4 μm.

(a) Deposit 0.45 μm silicon nitride (LPCVD)

(b) Pattern photoresist as a masking layer

(c) Etch silicon nitride in a reactive ion etcher

(d) Strip photoresist and etch silicon in KOH solution

Silicon   Silicon nitride   Photoresist
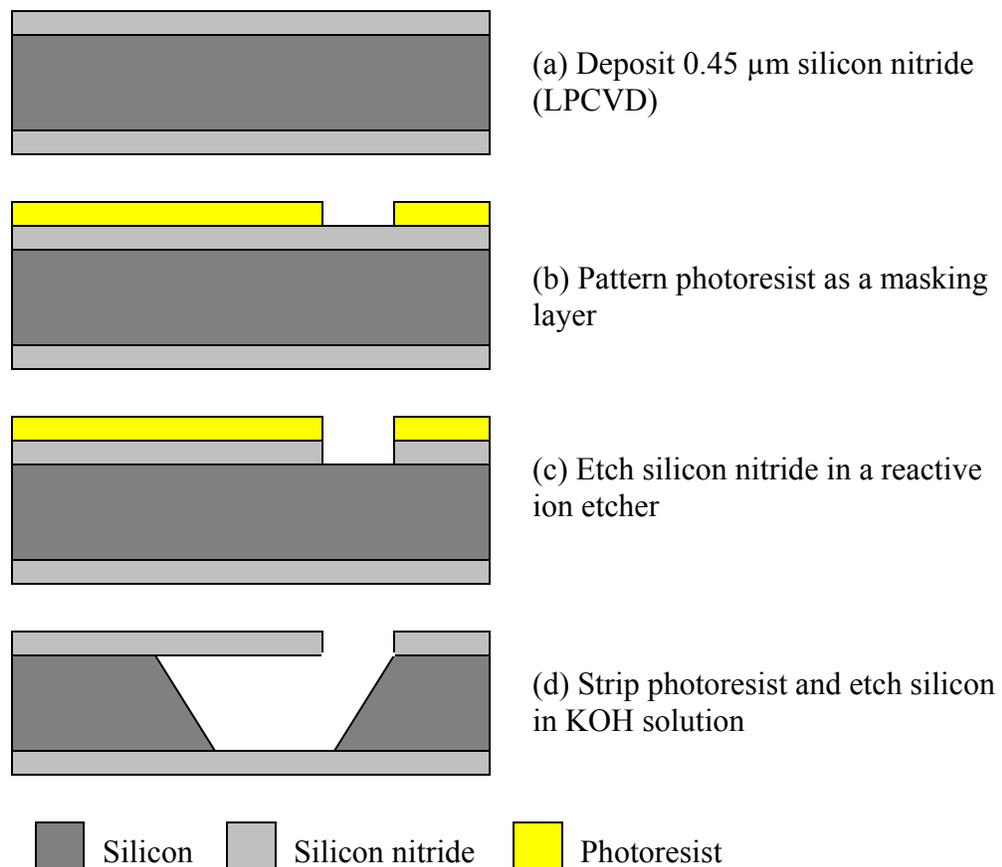
Figure 3.3: Process flow for T-shaped cantilever fabrication.

The release of the T-shaped cantilevers relies partially on the difference in the etch rates of silicon between {111} and {100} planes in alkaline liquids, as discussed in Chapter 1. More important in this case, the undercut of convex corners formed in the masking layer is the main mechanism to release the cantilever beams. When the opening in the masking layer has a convex corner, the {111} planes that initiate from the edges making up that corner are rapidly etched away, undercutting the convex corners of the mask. A plausible explanation for this behavior is that only two of the surface-atom bonds are directed into the silicon at a convex corner where two {111} planes meet, similar to atoms in {100} planes. Atoms exactly at such a boundary must have two dangling bonds, and thus are etched away, exposing fast-etching planes [32].

3.3 Young's modulus determination

3.3.1 Experimental techniques

As mentioned earlier, the resonant technique was used to determine the Young's modulus of silicon nitride thin films. To estimate the approximate resonant frequency, one cantilever was first pushed vertically with the micro-needle inside the focused-ion-beam (FIB) system and then released. The approximate resonant frequency was measured by pointing the electron beam in a fixed position where the vibrating cantilever moved in and out of the electron beam path. This modulated the secondary electron detector signal with the frequency of vibration. This signal was acquired with an oscilloscope and the approximate resonant frequency was determined. Subsequently, the micro-needle driven by the PZT translator contacted the chip and vibrated the cantilever near the frequency determined previously. The frequency was swept over a small range and the response was

48

monitored to determine the exact resonant frequency and the quality factor (resonant frequency divided by the bandwidth of half-power points). Figure 3.4 shows the schematic mechanism of the resonant test and Figure 3.5 is a scanning electron micrograph illustrating that each cantilever vibrates only when the driving frequency of the PZT translator matches with its resonant frequency.
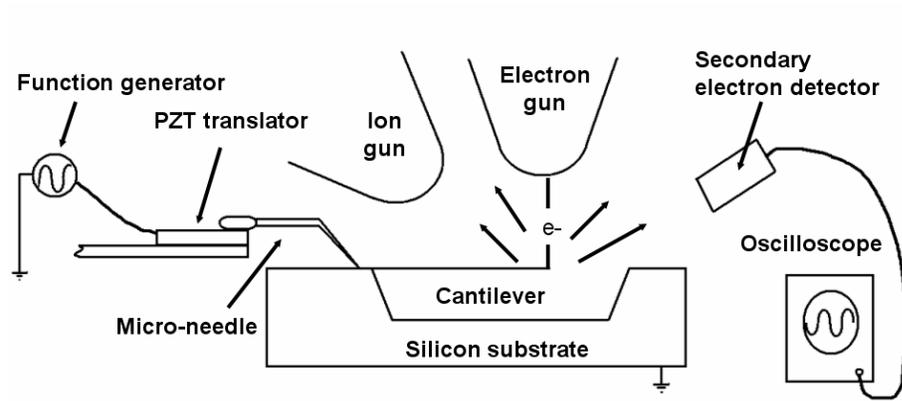
Figure 3.4: Schematic diagram of the mechanism for the resonant tests.
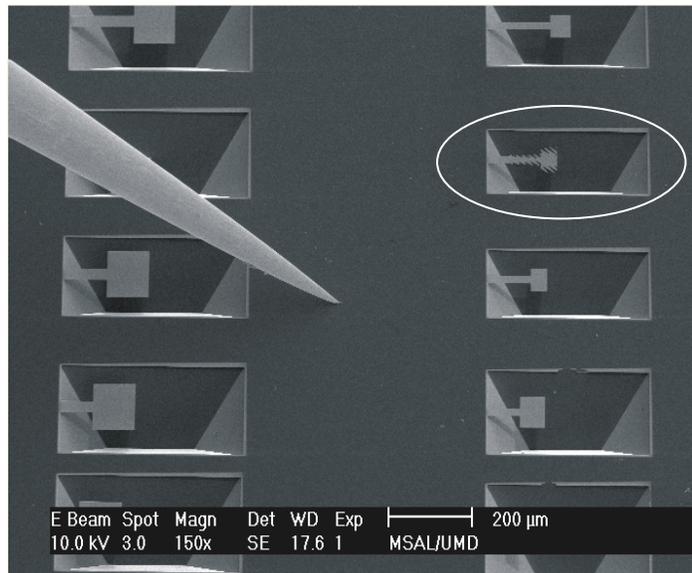
Figure 3.5: SEM picture of a vibrating cantilever. Only the second one from top on the right column vibrates because the driving frequency of the PZT translator is near its first resonant mode.

49

Once the first resonant frequency was determined, the Young's modulus from equation (3.1) was given by

$$E = \frac{4\pi^2 f^2 L^3 (m_b + c_1 m_a)}{3I}$$

(3.12)

which was expanded in terms of thickness as follows

$$E = \frac{16\pi^2 f^2 L^4 \rho}{t^2} (\frac{w_b}{w_a} \frac{L_b}{L} + c_1 \frac{L_a}{L})$$

(3.13)

where ρ is the mass density. From equation (3.13), the dimensions of T-shaped cantilevers are critical parameters to calculate Young's modulus. In general, the width and length of a cantilever are determined by layout design of the optical mask and can be measured directly inside the FIB system. On the other hand, the uncertainty of the thin film thickness is the primary source of error for the existing method. To solve this problem, previously the added mass method has been used to obtain the thickness of a cantilever [80, 81]. A small mass was added to a cantilever and the change in the resonant frequency due to an added mass was measured to calculate the thickness and Young's modulus. The disadvantage of this method is the difficulty to obtain the accurate mass added to the cantilever. Furthermore, to manipulate a bead (mass) on the microscale or nanoscale cantilever is a challenging task.

In contrast, the milling mass approach was introduced in our experiment. The area of the milling mass was determined precisely from the ion-milling pattern. The approximate thickness was estimated from the milling rate and the milling time, measured by the milling of test samples and End Point Detection (EDP) in the FIB system, respectively. If a mass m_i was milled away from the end of a cantilever, the first resonant frequency can be expressed as

$$(m_i - m_b - c_1 m_a) = -\frac{w_a t^3 E}{16\pi^2 L^3}\frac{1}{f_i^2} \tag{3.14}$$

The resonant frequencies f_i with different milling mass m_i were measured and the relation between m_i and $1/L^3 f_i^2$ was plotted. Here, the change of the effective cantilever length L was calculated by the shift of the center of the mass in region B (see Figure 3.1) due to the milling mass m_i. Consequently, the y-intercept yielded the effective mass $(m_b + c_1 m_a)$ and thickness of this T-shaped cantilever, and the slope gave the Young's modulus.

3.3.2 Experimental results

Since the KOH etching created an undercut of silicon (lateral etch), before the resonant test, ion milling was performed to obtain a fixed boundary of the cantilevers. The dimensions of these cantilevers were measured directly inside the FIB system using SEM capability. A T-shaped cantilever (cantilever 1) driven to its first resonant mode by the PZT translator is shown in Figure 3.6. The vibration amplitude of this cantilever near the resonant frequency was measured using the secondary electron detector and the resulting resonant spectrum is shown in Figure 3.7. The quality factor determined from the resonant spectrum is as high as 2050, which is expected due to the high vacuum inside the FIB system. Therefore, the damping effect for Young's modulus extraction can be neglected (the error is less than 3×10^{-6} %). Different masses at the end of the cantilever were milled away by the ion-milling function of the FIB system as shown in Figure 3.8 and the corresponding resonant frequencies were measured as shown in Table 3.3. Here, a density of $\rho = 3000$ kg/m^3 for LPCVD silicon nitride thin films [32] was used to calculate the milling mass m_i. The relation between m_i and $1/L^3 f_i^2$ was plotted and the equation of a straight line for best fitting was found using Mathematica (version 4.2,

Wolfram Research Inc.) as shown in Figure 3.9. Hence, the extracted thickness and Young's modulus were obtained from the y-intercept and the slope of this straight line, respectively. In our experiments, only one cantilever was milled away several times. For the other cantilevers, a single mass was milled away for the extraction of the thickness and Young's modulus due to nice linearity found in Figure 3.9. Table 3.4 presents the values of the extracted thickness of the cantilever and the Young's modulus of the LPCVD silicon nitride thin films.

From Table 3.4, the average Young's modulus of low-stress, LPCVD silicon nitride thin films at room temperature is 260.5 GPa with a standard deviation of 5.4 GPa. The Young's modulus of bulk silicon nitride is known to be in the range of 207 to 310 GPa [82]. Schneider and Tucker reported a Young's modulus of 230-265 GPa for 0.2-0.3 μm silicon nitride thin films [83], and Tabata *et. al.* obtained 290 GPa for 0.5 μm LPCVD silicon nitride thin films [84]. Therefore, the measured Young's modulus is certainly within the range of the reported values.
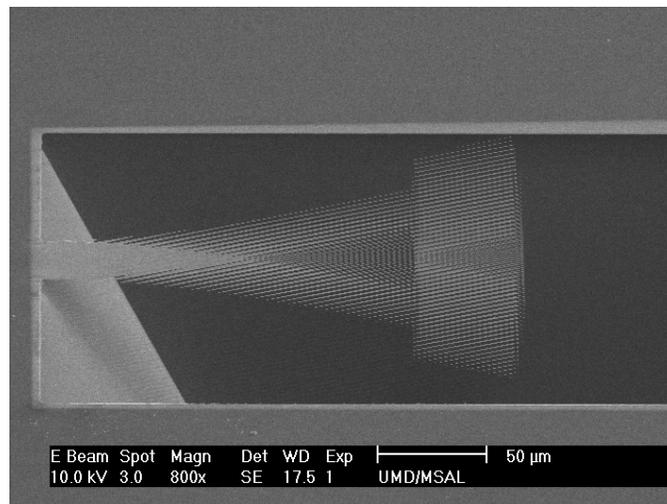
Figure 3.6: SEM picture of cantilever 1 at the first resonant mode.
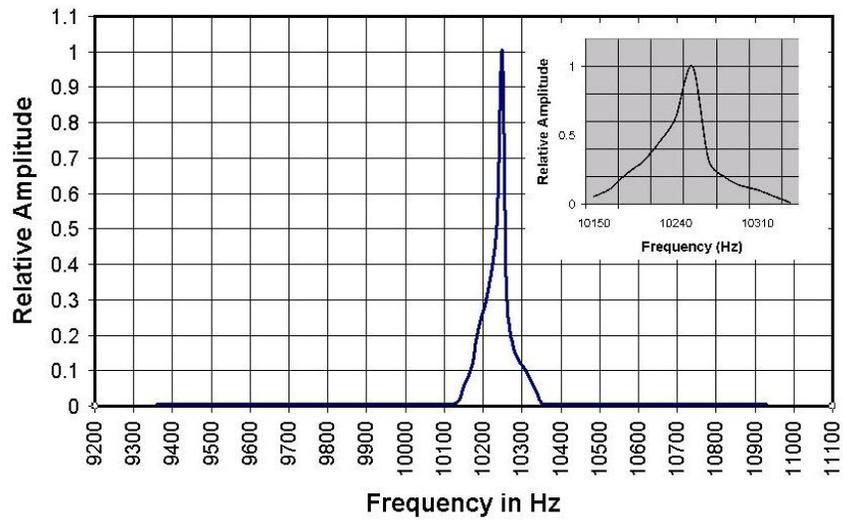
Figure 3.7: Resonant spectrum of cantilever 1. The insert is the close-up of the spectrum near the resonant frequency.
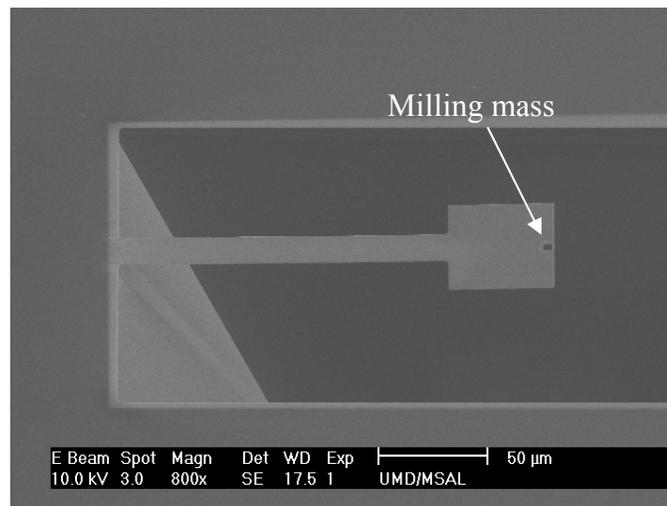
Figure 3.8: SEM picture of cantilever 1 with 12.15 pg milling mass.

Table 3.3: Dimensions of cantilever 1 with effective length and measured resonant frequency.

Dimensions (μm)	Milling Mass m_i (pg)	Effective Length L (μm)	Resonant Frequency f_i (Hz)
	0	180	10250
$L_a = 155$	12.15	179.929	10268
$W_a = 20$	33.75	179.811	10301
$L_b = 50$	48.6	179.733	10324
$W_b = 60$	109.35	179.431	10409
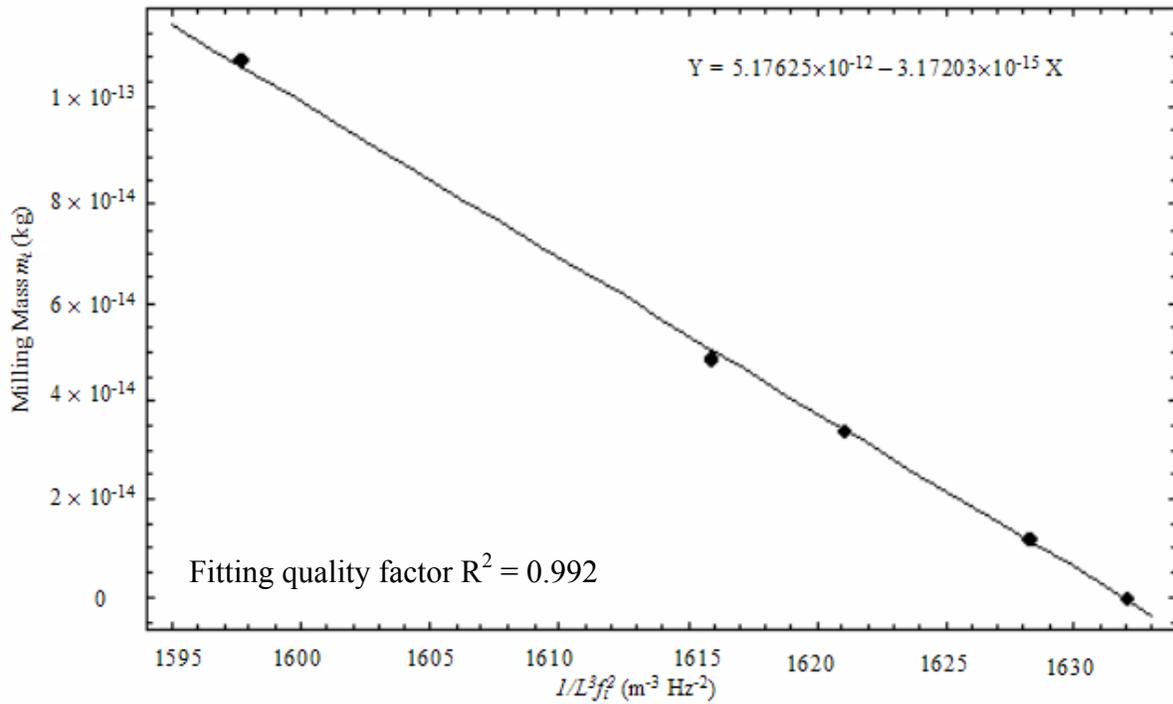
Figure 3.9: Linear plot of milling mass m_i versus $(L^3 f_i^2)^{-1}$ for cantilever 1.

Inside the plot:

$Y = 5.17625 \times 10^{-12} - 3.17203 \times 10^{-15} X$

Fitting quality factor $R^2 = 0.992$

Y-axis: Milling Mass m_i (kg)

X-axis: $1/L^3 f_i^2$ (m^{-3} Hz^{-2})

Table 3.4: Dimensions of cantilevers with extracted thickness and Young's modulus.

Cantilever Designation	Dimensions (μm)		Extracted Thickness t (μm)	Extracted Young's Modulus E (GPa)
1	$L_a = 155$ $L_b = 50$	$W_a = 20$ $W_b = 60$	0.4625	253.2
2	$L_a = 180$ $L_b = 20$	$W_a = 10$ $W_b = 40$	0.4867	268.8
3	$L_a = 149$ $L_b = 20$	$W_a = 10$ $W_b = 40$	0.4951	262.9
4	$L_a = 229$ $L_b = 50$	$W_a = 20$ $W_b = 100$	0.4800	265.4
5	$L_a = 178$ $L_b = 60$	$W_a = 20$ $W_b = 80$	0.4849	255.7
6	$L_a = 178$ $L_b = 50$	$W_a = 30$ $W_b = 75$	0.4572	258.9
7	$L_a = 129$ $L_b = 40$	$W_a = 20$ $W_b = 50$	0.4508	263.2
8	$L_a = 104$ $L_b = 40$	$W_a = 20$ $W_b = 60$	0.4491	256.2

After room temperature tests were finished, all cantilevers were cooled down to 30 K in the cryogenic setup and the resonant frequencies of these cantilevers were measured again. The Young's modulus calculated from (3.14) is shown in Table 3.5 and has an average of 266.6 GPa with a standard deviation of 4.1 GPa. Here, the value of 2.3×10^{-6} (K^{-1}) was used as the coefficient of thermal expansion (CTE) of silicon nitride for dimension modification. Although the reported values of CTE for silicon nitride varies from 1.67×10^{-6} to 2.3×10^{-6} (K^{-1}) [32, 85] and is also a function of temperature, less than 0.1% error was introduced in the calculation of the Young's modulus if only a single value was used because of the small absolute change in dimensions. The exact CTE

values at cryogenic temperatures will be discussed in Chapter 4. However, the variation of temperature will introduce thermo-mechanical stress and may cause local spring hardening or softening at the supporting boundary. The thermo-mechanical stress can be expressed as [32]

$$\varepsilon_{SiN} = (\alpha_{T_{SiN}} - \alpha_{T_{Si}})\Delta T \tag{3.15}$$

$$\sigma_{SiN} = (\frac{E}{1-v})\varepsilon_{SiN} \tag{3.16}$$

where ε_{SiN} is the thermal strain of silicon nitride, α_T is the CTE, σ_{SiN} is the thermo-mechanical stress of silicon nitride, and v is Poisson's ratio. If the value of 2.8×10^{-6} (K^{-1}) was used for the CTE of silicon [32], this thermo-mechanical stress was found to be -46.4 MPa at 30 K. Since the combination of this thermo-mechanical stress and the residual stress is still in a range of few hundred MPa, this effect can be ignored with negligible error.

Table 3.5: Resonant frequency and extracted Young's modulus at 298 K and 30 K.

Cantilever Designation	Resonant Frequency at 298 K (Hz)	Young's Modulus at 298 K (GPa)	Resonant Frequency at 30 K (Hz)	Young's Modulus at 30 K (GPa)
1	10409	253.2	10569	261.6
2	12781	268.8	12845	273.1
3	17222	262.9	17332	268.4
4	5096	265.4	5132	269.8
5	7080	255.7	7168	262.5
6	9006	258.9	9110	266.3
7	16221	263.2	16352	268.6
8	19945	256.2	20158	262.8

From our measurements, the Young's modulus increases from 260.5 GPa at 298 K to 266.6 GPa at 30 K. The student T test [86], a statistical method to compare two small sets of quantitative data, was performed on the measured Young's modulus, which showed that there is a "actual" change of the Young's modulus as temperature decreases (t = 2.55). The increase of the Young's modulus at low temperature can be explained by the fact that the distance of atom or ion separation decreases at low temperature (Figure 3.10) [87]. This distance is determined by the minimum potential energy, i.e. the first derivative of the potential energy is equal to zero. As temperature is decreased, inter-atomic force (second derivative of the potential energy) tends to increase because of the decrease of atomic distance. Since elastic reaction is due to the action of this force, the Young's modulus increases at lower temperatures.
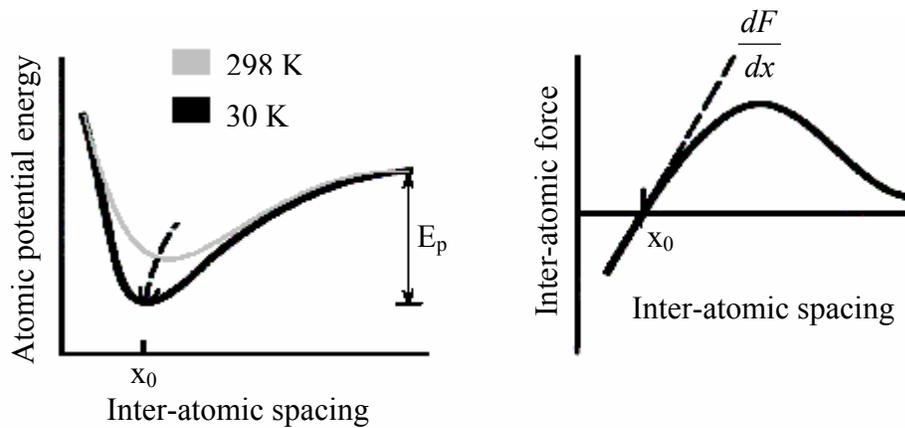
Figure 3.10: Variation of the atomic potential energy and inter-atomic force at cryogenic temperatures. The slope of the curve for inter-atomic force increases at low temperatures, which leads to a higher Young's modulus.

As discussed in Chapter 1, the operation of the microshutter array relies on "magnetic actuation" and "electrostatic hold" to open each microshutter element. The increase of the Young's modulus for silicon nitride thin films at 30 K may lead to failure as a result of

insufficient actuation and holding forces to turn on the microshutter element. Fortunately, the variation of the Young's modulus is only 2.3%, which is still in the range of tolerance when designing the actuation mechanism.

3.4 Poisson's ratio determination

The T-shaped cantilevers used for the Poisson's ratio measurement follows the same testing procedure as described in the previous section. The dimensions of the cantilevers used here are slightly modified to further reduce the torsional resonant frequency, which is estimated from an ANSYS finite element analysis (FEA) model. The micro-needle driven by the PZT translator contacted the device chip and vibrated the cantilever near the estimated torsional resonant frequency. The frequency was swept over a small range and the response was monitored to determine the exact torsional resonant frequency. Figure 3.11 shows a T-shaped cantilever vibrating at its torsional resonant frequency. In this experiment, the vibration amplitude of the T-shaped cantilevers was observed smaller than that in the Young's modulus measurement. This is due to the torsional motion of the T-shaped cantilever at the torsional resonant frequency, introducing smaller vertical movement (or displacement).

The Poisson's ratio of LPCVD silicon nitride thin films was calculated from equation (3.7) with the measured resonant frequency, and the measurement results are presented in Table 3.6. The average Poisson's ratio of LPCVD silicon nitride at 298 K was found to be 0.25 with a standard deviation of 0.02. In previous work, Coles *et al.* reported a Poisson's ratio of 0.23 [88] and Vlassak *et al.* obtained 0.28 [48]. The difference is mainly caused by different device preparation methods and testing techniques. Hence, the

measured Poisson's ratio is still within the range compared with the reported values.
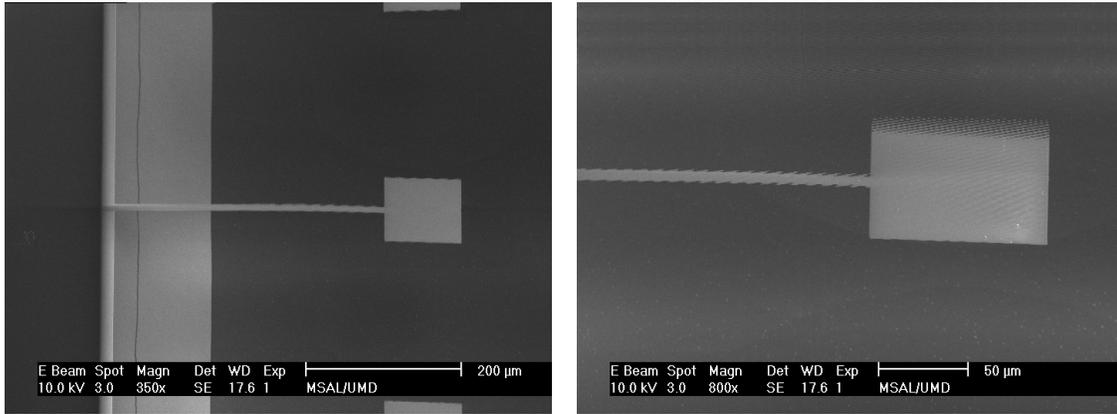
(a)

(b)

Figure 3.11: (a) SEM picture of a cantilever at the torsional resonant mode, and (b) close view of the cantilever.

Table 3.6: Measurement results for Poisson's ratio of LPCVD silicon nitride thin films at 298 K and 30 K.

Specimen	A	B	C	D	E	E
Dimensions (μm)	$La = 365$, $Wa = 20$, $Lb = 100$, $Wb = 100$ $t = 0.45$	$La = 365$, $Wa = 15$, $Lb = 100$, $Wb = 100$ $t = 0.45$	$La = 365$, $Wa = 10$, $Lb = 100$, $Wb = 100$, $t = 0.45$	$La = 365$, $Wa = 20$, $Lb = 100$, $Wb = 100$ $t = 0.45$	$La = 365$, $Wa = 15$, $Lb = 100$, $Wb = 100$ $t = 0.45$	$La = 365$, $Wa = 10$, $Lb = 100$, $Wb = 100$, $t = 0.45$
Test Temperature (K)	298 K	298 K	298 K	30 K	30 K	30 K
Measured Resonant Frequency (kHz)	18.238 - 18.310	15.828 - 15.880	12.930 - 12.885	18.428 - 18.487	15.966 - 16.015	13.017 – 12.966
Number of Test Samples	16	16	16	16	16	16
Average Poisson's Ratio	0.252	0.247	0.251	0.258	0.259	0.264
Standard Deviation	0.02	0.02	0.03	0.03	0.02	0.03

The average Poisson's ratio at 30 K was found using the same method to be 0.26 with a standard deviation of 0.03. The increase of the Poisson's ratio at low temperature is related to the change of atomic bonding of the silicon nitride atoms and molecules, which requires further investigation to understand the real mechanism. For the design of the microshutter array, the maximum operation stress occurs at the fixed ends of the torsion bar, which can be considered as a doubly-clamped beam. Therefore, the influence of a slight increase of the Poisson's ratio (less than 5%) at 30 K can be neglected.

3.5 Fracture strength determination

3.5.1 Experimental techniques

For the fracture strength measurement, bending tests of T-shaped cantilevers were performed in our study. The device stage where a device chip was mounted inside the FIB system was first tilted with an angle α. The purpose of this arrangement was to observe the bending angle of T-shaped cantilevers during experiment using an electron beam. The micro-needle was then positioned to contact the cantilever and gently pushed the blade of the cantilever down. The bending angle was carefully recorded until fracture. From equation (3.11), the fracture strength of the silicon nitride thin film can be obtained.

3.5.2 Experimental results

A bending T-shaped cantilever before and after fracture is shown in Figure 3.12. In our experiments, T-shaped cantilevers with larger region B were fabricated to make region B relatively rigid to region A and to minimize the measurement error of L_f. Although the deflection at the tip of a cantilever caused by the stress gradient is

proportional to the square of the beam length, no obvious bending curvature was found even in the longest cantilever. The dimensions of conventional cantilevers used in bending tests can vary over a large range from mm to nm [89-91], mainly determined by the considerations of measurement setups and stress gradients of the beams.

Several phenomena were observed in our bending tests. First, the cantilevers with L_a larger than 3 μm survived the bending force even when they reached the side walls of the v-grooves. Second, since the displacement of the cantilever was much larger than its thickness at the fracture point, in-plane stress cannot be neglected. Hence, equation (3.11) is not valid in this condition. Third, as mentioned in the section on device preparation, the boundary at the end of the cantilever was floating due to the undercut of silicon in the KOH solution. To accommodate these factors, an ANSYS finite element analysis (FEA) model was developed to obtain accurate fracture strength. In this model, the curvature of region A caused by the fabrication process was also measured and used to simulate the stress concentration of region A.

Instead of measuring fracture angle θ at $x = L_a$, the displacement at $x = L_t$ was determined and used as the input of the FEA model as shown in Figure 3.13. From the simulation results, the maximum stress occurs at the edge of region A. Here, the Young's moduli of 260.5 GPa and 266.6 GPa and the Poisson's ratio of 0.25 and 0.26 were used for 298 K and 30 K respectively in this model. The fracture strengths of LPCVD silicon nitride at 298 K and 30 K are presented in Table 3.7. From this table, the average fracture strength at 298 K was found to be 6.9 GPa with a standard deviation of 0.6 GPa. In previous work, Yang *et al.* reported a fracture strength of 12.1 GPa [93] and Coles *et al.* obtained 6.4 GPa [88], both for LPCVD silicon nitride thin films. The difference is

mainly caused by different fabrication processes and testing techniques. Hence, the measured fracture strength is still within the range compared with the reported values.

The average fracture strength at 30 K was found using the same method to be 7.9 GPa with a standard deviation of 0.7 GPa. The increase of the fracture strength at low temperature can be attributed to less thermal agitation. As the temperature is lowered, the atoms in the specimen vibrate less vigorously. A larger applied stress is required to initiate a crack to break the specimen, leading to a higher fracture strength. However, the above explanation is only valid for a defect-free material. For most brittle materials, the fracture strength is determined by stress concentrations from growth flaws, yet their variations at cryogenic temperatures are still not clear.

The minimum observed fracture strength of silicon nitride thin films (5.7 GPa) from the bending tests was used to design the microshutter array, and the expected operating stress of each microshutter element is 2.5 GPa [94], which is much lower than the observed fracture strength. As the temperature decreases to 30 K, the higher fracture strength of silicon nitride thin films will further reduce the probability of fracture failure of the microshutter array during operation.

(a)   (b)
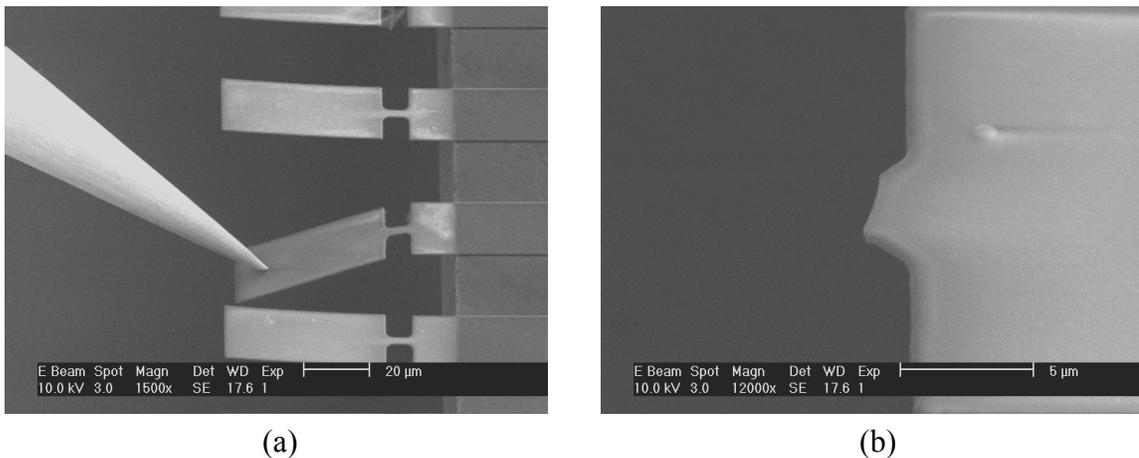
Figure 3.12: SEM pictures of a cantilever (a) before and (b) after fracture during the bending test.
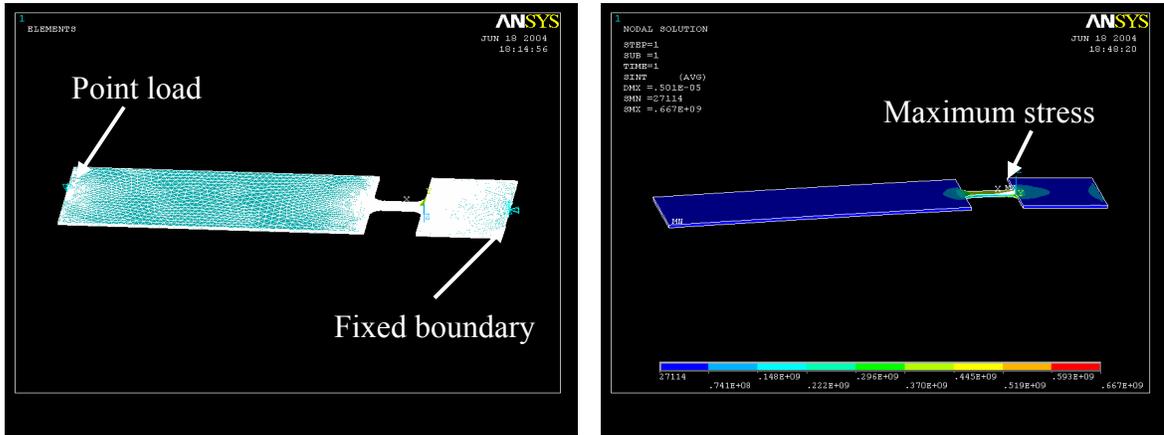
(a)   (b)

Figure 3.13: ANSYS finite element analysis model: (a) mesh of the test specimen using " solid 187" element, and (b) the stress distribution.

Table 3.7: Test results obtained using ANSYS FEA model with bending measurements as inputs at 298 K and 30 K.

Specimen	A	B	C	D	E
Dimensions (µm)	$La = 1.0$, $Wa = 5.0$ $Lb = 28$, $Wb = 28$ $t = 0.45$	$La = 1.3$, $Wa = 5.0$ $Lb = 28$, $Wb = 28$ $t = 0.45$	$La = 1.5$, $Wa = 15$ $Lb = 85$, $Wb = 85$ $t = 0.45$	$La = 1.0$, $Wa = 5.0$ $Lb = 28$, $Wb = 28$ $t = 0.45$	$La = 1.5$, $Wa = 15$ $Lb = 85$, $Wb = 85$ $t = 0.45$
Test Temperature (K)	298 K	298 K	298 K	30 K	30 K
Average Fracture Strength (GPa)	6.7	7.2	7.1	7.9	8.0
Standard Deviation (GPa)	0.7	0.5	0.6	0.7	0.6
Number of test samples	20	10	20	20	20

3.6 Discussion

From this study, the Young's modulus and the Poisson's ratio of LPCVD silicon nitride thin films increase by 2.3 % and 4 %, respectively, from 298 K to 30 K, while the fracture strength increases by 14.5%. Several uncertainties may cause errors in the extraction of these properties. First, even though the errors introduced from using a single value of CTE is small, the exact CTE values need to be measured at cryogenic temperatures to minimize these errors. Second, the cross sections of the test specimens are not perfectly rectangular due to the fabrication process, especially at the smaller widths. This will change the moment of inertia during the bending tests. This effect was not considered in the FEA model since the variation of the moment of inertia is negligible (less than 1%). Third, the end of the T-shaped cantilever beam was not perfectly clamped (fixed). Instead, in real structures, the beam supports tend to exhibit some compliance and the exact analysis of this effect is complicated. However, the influence of the support compliance is insignificant in the determination of the fracture strength since the maximum stress occurs at the end of region A, not at the end of the fixed boundary (Figure 3.13).

For designing MEMS devices operating at cryogenic temperatures using LPCVD silicon nitride thin films, one can use the values of the Young's modulus, the Poisson's ratio and fracture strength at room temperature as the first design parameters. This method is conservative and safe for the first device demonstration. However, for composite structures, the stress caused by the mismatch of CTE at cryogenic temperatures is more pronounced than the change of the Young's modulus, the Poisson's

ratio, and fracture strength, especially for optical MEMS devices requiring flat surfaces as discussed in section 2.5.

3.6 Summary

In this chapter, a new test device, T-shaped cantilever beams, is introduced for Young's modulus, Poisson's ratio, and fracture strength measurement. The concept of using these T-shaped cantilevers instead of conventional ones is discussed and the test devices are fabricated by bulk micromachining technique, which is a relatively simple process. Resonant testing is carried out to obtain the Young's modulus and the Poisson's ratio of LPCVD silicon nitride thin films. To determine the thickness of the cantilever, the variation of resonant frequencies with different milling masses is recorded and an analytic model is developed to extract the thickness and Young's modulus simultaneously. The fracture behavior of LPCVD silicon nitride is characterized using a bending test combined with an FEA model.

From the experiment, the Young's modulus of LPCVD silicon nitride thin films varies from 260.5 GPa at 298 K to 266.6 GPa at 30 K, and the Poisson's ratio increases from 0.25 at 298 K to 0.26 at 30 K. In addition, the fracture strength ranges from 6.9 GPa at 298 K to 7.9 GPa at 30 K. The increase of the Young's modulus and fracture strength is attributed to the decrease in thermal agitation between atoms at cryogenic temperatures. The coefficient of thermal expansion and fatigue property of LPCVD silicon nitride thin films at cryogenic temperatures will be discussed in Chapter 4 and Chapter 5 for further understanding of mechanical property behavior at cryogenic temperatures.

CHAPTER 4

HIGH SENSITIVITY MICROGAUGE SENSORS FOR RESIDUAL STRESS AND COEFFICENTS OF THERMAL EXPANSION CHARACTERIZATION

The design of mechanical structures in MEMS devices requires the characterization of the stress state in these structures under the combined influence of both loading and residual stresses. The values of residual stress are vital for accurately predicting maximum loads, resonant frequencies, and many other properties. Additionally, high residual stress may cause buckling, warpage, or dimensional variations. Therefore, knowledge about residual stress in deposited thin films is important for MEMS researchers. The microshutter arrays, as discussed in Chapter 1, consist of a 2 × 2 format mosaic of four 387 × 175 arrays and require a relatively large out-of-plane displacement during operation. To obtain reliable microshutter elements across the device, not only the values of the residual stress in silicon nitride thin films (the structural layers of the microshutter arrays) needs to be understood, but also the uniformity.

Additionally, a linear coefficient of thermal expansion (CTE), defined as the fractional change in length of a material for a unit variation in temperature, is a critical mechanical property in the design of MEMS devices, integrated circuits, and electronics packaging. For example, the mismatch of CTEs between attached films introduces residual stress, which results in a high density of imperfections in the interface [95]. Some MEMS devices use the difference in CTE to their advantage, such as in bimorph or

thermal actuators [96, 97]. Although there are well-documented thermo-physical properties of bulk materials, however, these may not be directly applicable to thin films; the mechanical properties of thin films are strongly dependent on the fabrication processes such as film deposition methods and parameters [98]. For the operation of the microshutter arrays at 30 K, the mismatch of CTEs among the silicon nitride, aluminum, and cobalt/iron thin films will cause an out-of-plane curvature and increase leakage light, as discussed in Chapter 2. The thermal stresses of these thin films at 30 K must be balanced with the residual stresses to obtain a flat surface of each microshutter element in the outer space environment. Hence, a technique to measure the CTEs of these thin films at cryogenic temperatures is required.

This chapter presents a new microgauge sensor for residual stress and CTE characterization with an expected resolution as high as 5 $\mu\varepsilon$ [99]. In this study, $\mu\varepsilon$ is used as a unit for differential deformation in length and is defined as 10^{-6} strain. The micrgauge sensor, made of the same silicon nitride thin film as the microshutter array, is fabricated using bulk micromachining technique. The residual stress of the silicon nitride thin film is studied by measuring the displacement of the microgauge sensor when the sensor is released from a substrate. To characterize the CTE of the silicon nitride thin film at cryogenic temperatures, the microgauge sensor is cooled down using the cryogenic measurement setup described earlier and the displacement of the sensor is measured again. In the experiments, all displacements are measured using the SEM function provided by the FIB system. An analytic model based on beam theory is developed to calculate the residual stress and CTE values from the measured

displacements. At the end of this chapter, the test results of the residual stress and CTE are reported for the low-stress silicon nitride thin film.

4.1 Design of microgauge sensor

A variety of methods have been developed to measure residual stresses and CTE of thin films. A conventional approach to measure the average residual stress is using the Stoney's equation [100]. This method requires knowledge of the curvature of a substrate after depositing a thin film, the biaxial elastic modulus of the substrate, and the thickness of the thin film and the substrate, which may introduce significant errors in the extraction of residual stress. Additionally, two main assumptions for this technique are that the film is very thin compared to the substrate, and the deformations are infinitesimally small. A detailed discussion of limits for the Stoney's equation was described in the literature [101].

In order to obtain local stress information, passive strain sensors using a buckling technique have been developed [102]. This approach is based on proof structures in which a beam's maximum length remains unbuckled under a compressive strain. Previous efforts have modified these proof structures as ring or diamond structures for measuring tensile strain [103]. However, the disadvantages in using the buckling technique are that an entire array of the microstructures is needed, and the boundary condition (such as support compliance) can be a factor influencing the accuracy of strain measurement.

Other types of passive strain sensors use only one microstructure. The so-called T-shaped or H-shaped microstructures provide the displacement of a junction between wide

and narrow beams [104, 105]. However, such structures yield extremely small displacements, thereby making an accurate measurement difficult. Recently, an improved micro strain gauge with mechanical amplifier has been developed to magnify this small displacement of a long test beam through the use of a sloped beam [106]. The strain level in the test beam is deduced by measuring the free end movement of the third beam connecting to the sloped beam. Unfortunately, this technique is limited due to the out-of-plane deformation.

For CTE measurements, a conventional thermal-stress approach using optical beam techniques is widely adopted [107, 108]. The principle of this method is to measure the change in the curvature of a wafer induced by a deposited film using an optically levered laser beam technique in conjunction with a thermally-controlled hot stage. However, this technique requires knowledge of the exact physical values of thin films such as the biaxial elastic modulus, which may not be readily available.

Presently, other approaches for CTE measurements using microstructures are being studied extensively. A buckling of clamped square plates has been reported to measure CTEs of thin films [109]. The buckling is investigated numerically using an energy minimization method and finite element simulations. Similar to the buckling technique for residual stress measurement, the disadvantage of this method is that it is extremely sensitive to the geometry and boundary conditions of the microstructures and exact analysis of these effects can be complicated. The micro strain gauge mentioned previously has also been utilized to measure the CTE of polysilicon thin films [110]. However, there are limits to this method. For example, it is only applicable to conductive thin films so that enough Joule heating can be generated at the microgauge. Besides, the

average temperature of the microgauge is determined from the experimental parameters such as measured current, applied voltages and the thermal conductivity of the microgauge, which may induce significant errors in the temperature measurement.

In our study, two types of new microgauge sensors with mechanical amplification are designed to characterize the residual stress and the CTE of silicon nitride thin films as shown in Figure 4.1(a). These two microgauge sensors are the same except the structures of vernier gauges. The design principle is to magnify the tiny displacement caused by the residual strain or the thermal strain between anchors. The shrinkage/expansion of the test beam due to the residual/thermal strain causes the slope beam to rotate slightly. The indicator beam magnifies the slope and a large displacement is generated at the site of the vernier gauge, which can be easily measured using a scanning electron microscope or an optical microscope. Figure 4.1(b) is a schematic diagram of the designed microgauge sensors under tensile residual/thermal strain. The significance of this design is that this microgauge sensor gives a strain reading which is independent of the thin film thickness (discussed in the next section), a key factor of error for other methods. In addition, this reading is independent of process variations, which may result in irregular beam cross section; for example, a trapezoidal shape. Therefore, this kind of process imperfection is not a problem for the strain gauge presented here. Moreover, the symmetry design of the microgauge sensor can minimize the influence of the out-of-plane curvature on the indicator beams.
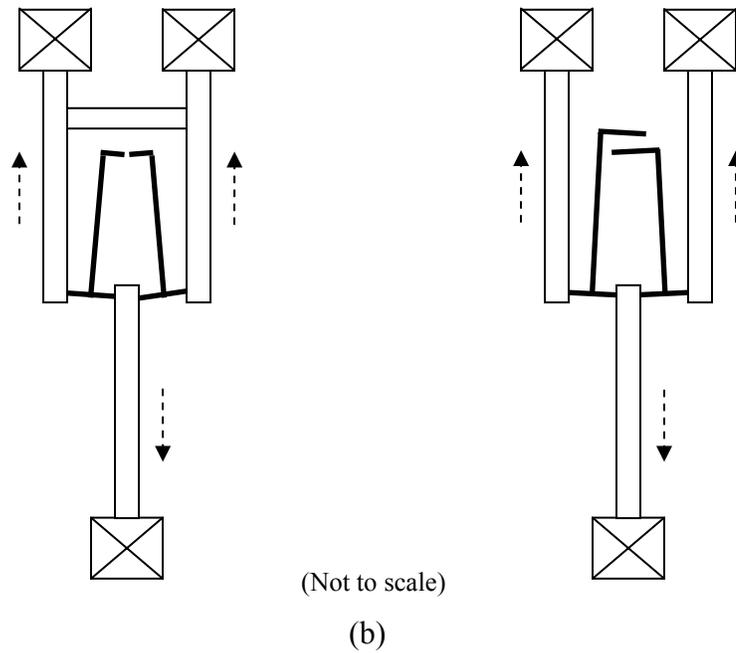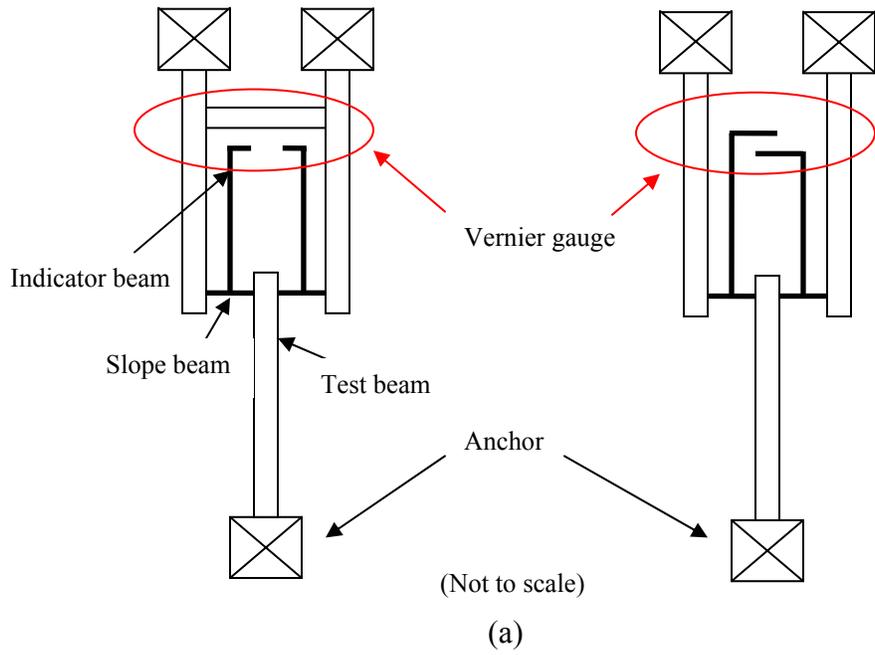
Figure 4.1: Schematic diagram of the designed microgauge sensors: (a) without residual/thermal strain, and (b) with tensile residual/thermal strain. The dash lines represent the shrinkage of the test beams.

4.2 Analytic model

An analytic model for the microgauge sensors is developed based on beam theory. As shown in Figure 4.2 (a), the slope beam between two test beams is a doubly-clamped cantilever and can be theoretically modeled as two simple cantilever beams connected together (Figure 4.2(b)). Therefore, the maximum angular deflection θ at the midpoint of the slope beam in a small angle approximation can be expressed as [78]

$$\theta \approx \tan\theta = \frac{F_t L_s^2}{8EI} \tag{4.1}$$

where F_t is the tangential force at the fixed boundary, L_s is the length of the slope beam, E is the Young's modulus, and I is the moment of inertia. Also, the movement of the test beam δ is derived as [78]

$$\delta = \frac{F_t L_s^3}{12EI} \tag{4.2}$$

The maximum angular deflection θ can then be rewritten in terms of the movement of the
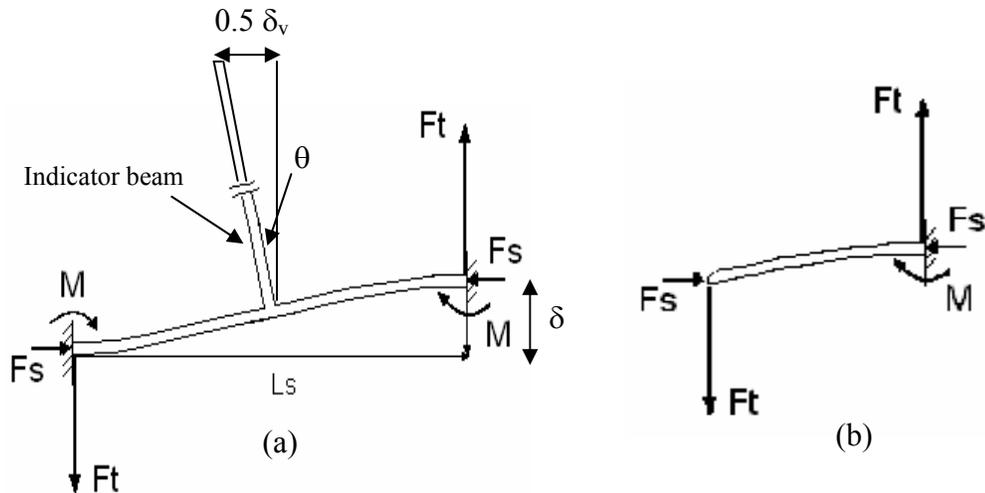
Figure 4.2: Force and moment free body diagram of the slope beam: (a) the entire slope beam, and (b) a simple cantilever beam representing the right-half the entire beam.

72

test beam δ as follows

$$\theta = \frac{3\delta C_f}{2L_s}$$
(4.3)

In equation (4.3), C_f is a correction factor due to the presence of the indicator beam and is derived as [106]

$$C_f = \frac{1-d^2}{1-d^3}$$
(4.4)

where d is the ratio of the width of the indicator beam W_i over the length of the slope beam L_s. If the measured displacement of the vernier gauge from one indicator beam is assumed to be 0.5 δ_v, the mechanical amplification by which the tiny movement of δ is magnified to a value of δ_v can be found as

$$\frac{\delta_v}{\delta} = \frac{3L_i C_f}{L_s}$$
(4.5)

where L_i is the length of the indicator beam. The residual/thermal strain ε, by definition, is the ratio of δ over double the length of the test beam (2 L_t) and can be represented as

$$\varepsilon = \frac{L_s \delta_v}{6L_i L_t C_f}$$
(4.6)

Therefore, the residual stress σ is

$$\sigma = \frac{EL_s \delta_v}{6L_i L_t C_f}$$
(4.7)

and the coefficient of thermal expansion α is

$$\alpha = \frac{L_s \delta_v}{6L_i L_t C_f \Delta T}$$
(4.8)

where ΔT is the temperature variation during experiments. From (4.7) and (4.8), the measured residual stress and CTE are independent of the thin film thickness.

In the design of the microgauge sensors, the stiffness of the slope beam K_s in the direction of displacement due to the residual stress in the test beam is not considered in the analytic model. This effect can be evaluated by the ratio of K_s to the stiffness K_t of the test beam in the direction of the displacement:

$$\frac{K_s}{K_t} = \frac{L_t W_s^{\ 3}}{L_s^{\ 3} W_t} \qquad (4.9)$$

where L_t and W_t are the length and width of the test beam, and L_s and W_s are the length and width of the slope beam. In the mask design of the microgauge sensors, the dimensions of these sensors (Table 4.1) are varied to measure different stress conditions with different mechanical amplifications defined in (4.5). Since the ratio of (4.9) can be shown to be much less than one, this effect can be neglected.

Table 4.1: Dimensional design of the microgauge sensors.

Test beam		Slope beam		Indicator beam	
L_t (μm)	W_t (μm)	L_s (μm)	W_s (μm)	L_i (μm)	W_i (μm)
100 - 510	30	20 - 40	1.5 - 2	100 - 350	2

A first-order error analysis can be carried out by examining (4.6) with an assumption that δ_v, the reading of the vernier gauge, is the only source of error while other dimensions have negligible error effects. The resolution of δ_v is mainly determined by the design of the vernier gauge. In our design of the vernier gauge, the minimum spacing

74

between two vernier fingers with sharp tips is 1 μm. Therefore, it is fair to say that the maximum uncertainty of the measurement from the vernier gauge is 0.25 μm. The strain reading with error bound can be represented as

$$\varepsilon = \frac{L_s \delta_v}{6 L_i L_t C_f} (1 \pm \frac{0.25}{\delta_v}) \tag{4.10}$$

and the best resolution in the strain measurement for the designed microgauge sensors listed in Table 4.1 is 5 με, which has double sensitivity compared with the previous work [106].

An ANSYS finite element model (Figure 4.3) was developed not only to perform strain-displacement analysis of the microgauge sensors, but also to check the analytical theories. Strain was introduced in the model by applying a uniform temperature change to the microgauge sensor with a specified coefficient of thermal expansion. Figure 4.4 compares the displacement of the vernier gauge obtained by the analytic model with the ANSYS model. It is found that the theoretical model matches well with the ANSYS
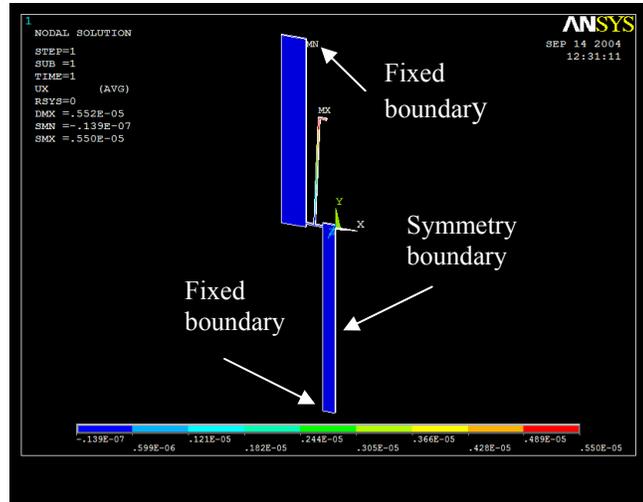
Figure 4.3: ANSYS finite element model for the microgauge sensor. Only half of the structure is used due to its symmetry. ($L_t = 250$ μm, $W_t = 30$ μm, $L_s = 20$ μm, $W_s = 2$ μm, $L_i = 150$ μm, $W_i = 2$ μm, thickness = 0.5 μm)

75

simulation results and there is no nonlinear effect even with a high strain value of 0.0025, which corresponds to a large displacement of more than 25 µm. For the same movement at the vernier gauge, the theoretical model underestimates the real strain. However, the maximum discrepancy is only 3.1%.
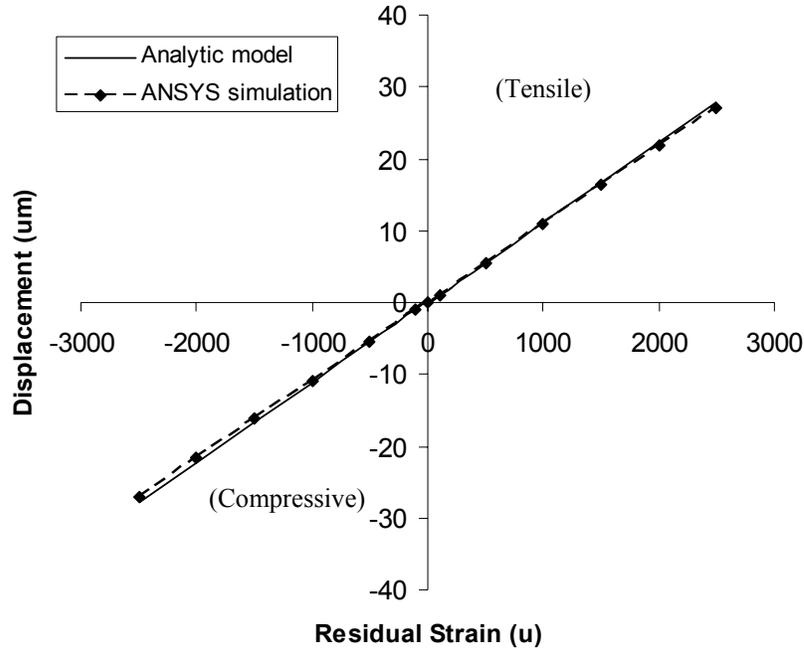
Figure 4.4: Comparison of the displacement obtained by the analytic model and the ANSYS simulation results.

4.3 Device preparation

The microgauge sensors have been fabricated using bulk micromachining technique. The fabrication processes are similar to those for the T-shaped cantilevers discussed in Chapter 3. First, a layer of LPCVD silicon nitride thin film with an approximate thickness of 0.5 µm was deposited on a 500 µm thick n-type silicon substrate. A standard

lithography process was performed, and the patterned photoresist was used as a masking layer for silicon nitride etching. The silicon nitride thin film was etched in a reactive ion etcher (RIE). Next, the wafer was placed into a 20%, 72°C potassium hydroxide (KOH) solution for 2 hours with uniform agitation to release the microgauge sensors. The depth of etched v-groove was 95 μm. The detailed process parameters can be found in section 3.2.

After completing the fabrication processes, most devices were found to have "stiction" problems as shown in Figure 4.5. This is mainly caused by capillary forces arising as a result of the surface tension of the liquid-vapor interface during the rinsing and drying steps in the fabrication processes. A supercritical point CO_2 dryer (Tousimis[TM], Model: Autosamdri®-815, series B) was used to solve the stiction problem. The supercritical CO_2 drying makes use of the supercritical point of carbon dioxide in the phase diagram at $T_C = 31.1°C$ and $P_C = 72.8$ atm [111]. At this point, both liquid and gas
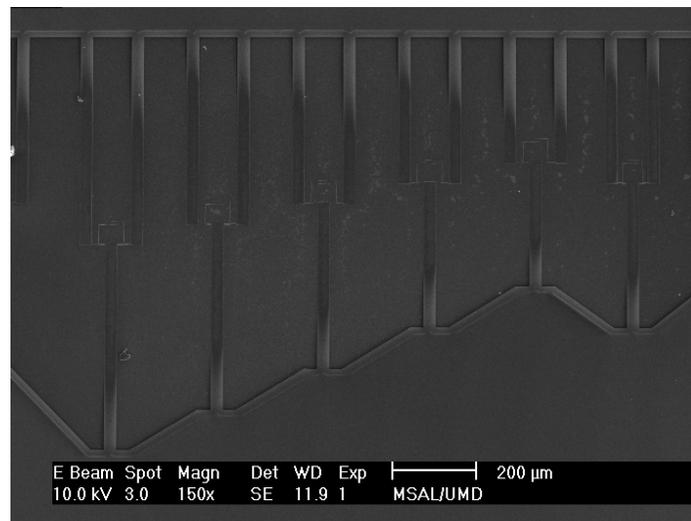
Figure 4.5: SEM picture of microgauge sensors after fabrication. All devices shown in the picture stick to the substrate.

properties exist simultaneously with no surface tension. The microgauge sensors released

in this manner are shown in Figure 4.6.
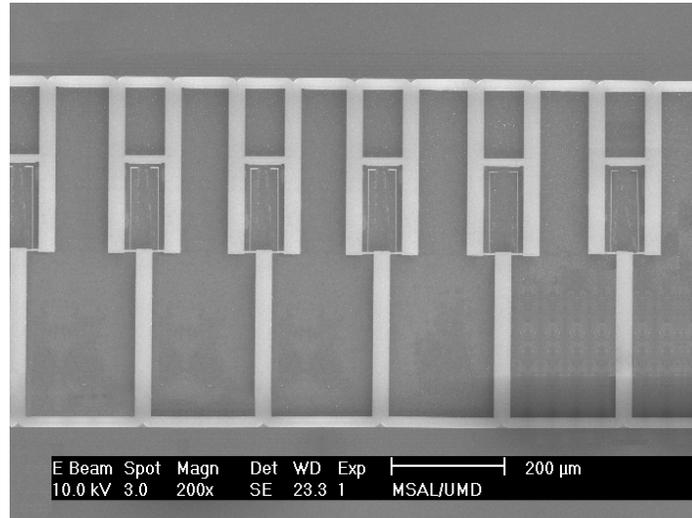
Figure 4.6: SEM picture of microgauge sensors after supercritical CO_2 drying. All devices shown in the picture are released from the substrate.

4.4 Residual stress characterization

Two LPCVD silicon nitride thin films were deposited on silicon substrates with different process parameters from two vendors and utilized as the structural layers of the microgauge sensors. The fabricated microgauge sensors were placed inside the FIB system (see Chapter 2). The displacement of the vernier gauge was then determined by using the SEM function provided by the FIB. Figure 4.7 and Figure 4.8 show the displacements of the vernier gauges for characterizing these two silicon nitride thin films. From equation (4.6), the strains for these two types of silicon nitride thin films are 708.1 $\mu\varepsilon$ and -135.1 $\mu\varepsilon$, respectively. The corresponding residual stresses are 184.5 MPa and -35.3 MPa if the value of 260.5 GPa is used as the Young's modulus (Chapter 3) for these

silicon nitride thin films. Here, a positive value represents a tensile residual stress, while a negative value means a compressive residual stress.
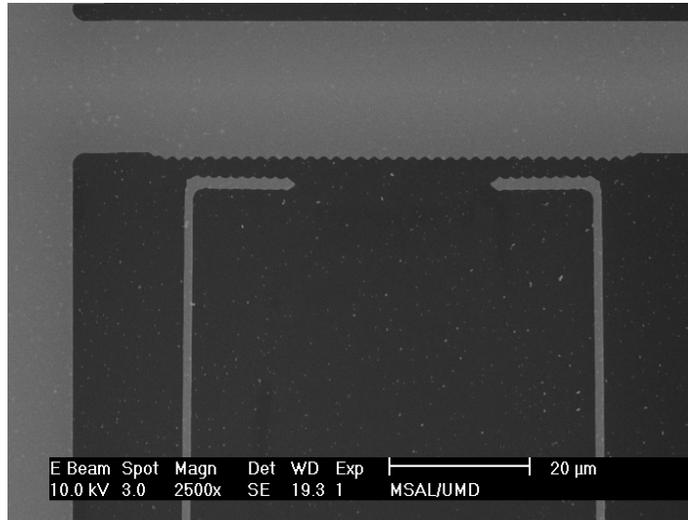
Figure 4.7: SEM picture of the vernier gauges for characterizing the first silicon nitride thin film. (Measured displacement δ_v = 5.6 μm, dimensions: L_t = 265 μm, W_t = 30 μm, L_s = 20 μm, W_s = 2 μm, L_i = 100 μm, W_i = 1.5 um, calculated residual strain = 708.1 με)
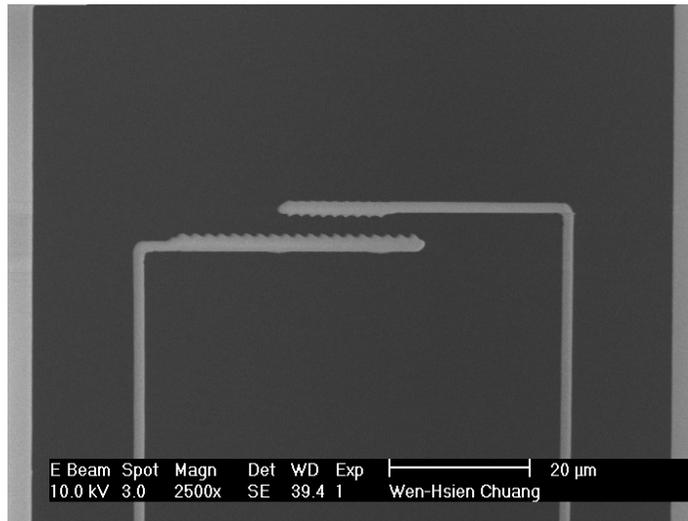
Figure 4.8: SEM picture of the vernier gauges for characterizing the second silicon nitride thin film. (Measured displacement δ_v = 2.5 μm, dimensions: L_t = 400 μm, W_t = 30 μm, L_s = 20 μm, W_s = 2 μm, L_i = 150 μm, W_i = 2 um, calculated residual strain = -135.1 με)

With the measurements of the microgauge sensors, a local knowledge of residual stress distribution is possible. Table 4.2 shows the measurement results of the entire wafers for these two silicon nitride thin films. The standard deviations of the residual stresses are 8.0% (Type A) and 9.6% (type B) of the average values, and the stresses at the edges of the wafers are found to have larger deviation than the centers. If the measured stress values on the edges, defined as the distances larger than 3 cm from the center of the wafers, are not considered, the standard deviations can be reduced to 3.9% (Type A) and 5.2% (Type B) of the average values. These variations are acceptable for the microshutter arrays since small changes of the stiffness of the microshutter devices across the whole array due to the residual stresses can be compensated with higher magnetic actuation forces.

Table 4.2: Test results of residual stresses in different silicon nitride thin films.

Type	A	B
Number of tests	30	30
Average residual stress (MPa)	183.4	-38.6
Standard deviation (MPa)	14.7	-3.7

However, the compressive residual stress may cause buckling on the torsion bars of the microshutter devices (Chapter 1). This effect can be examined by the Euler buckling limit, given by [32]

$$\sigma_{Euler} = -\frac{\pi^2}{3}\frac{Et^2}{L^2}$$

(4.11)

where E is the Young's modulus, t is the thickness, and L is the length of the doubly-supported beam. The Euler buckling limit of the torsion bar can be found to be -5.4 MPa with the given Young's modulus (260.5 GPa), thickness (0.5 μm), and beam length (200 μm). This value is approximately seven times smaller than the residual stress of the second (type B) silicon nitride thin films, which will lead to buckling on the torsion bars. Therefore, the first silicon nitride thin films (type A) are used in the fabrication of the microshutter arrays.

4.5 Coefficient of thermal expansion (CTE) characterization

The CTEs of silicon nitride thin films at cryogenic temperatures were characterized with the microgauge sensors inside the FIB system. These sensors were cooled down using the designed cryogenic measurement setup mentioned in Chapter 2. The temperature of the devices was determined by an integrated resistive temperature sensor, and the displacement at the vernier gauge was measured by using the SEM function provided by the FIB. To prevent the charging effect on the silicon nitride thin films during experiment, electron beam of the FIB system was turned on for taking scanning micrograph only when the sensors reached desired temperatures.

Since the microgauge sensors were fabricated on silicon substrates, it is inevitable that the contraction of silicon at cryogenic temperatures will influence the measurement results. The analytic model for CTE characterization can be modified with the consideration of this effect and expressed as

$$\Delta\alpha = \alpha_{SiN} - \alpha_{Si} = \frac{L_s \delta_v}{6 L_i L_t C_f \Delta T} \tag{4.12}$$

where α_{SiN} is the CTE of the silicon nitride, and α_{Si} is the CTE of the silicon. Hence, the measured thermal strain is caused by the difference of CTEs between the silicon nitride structural layer and the silicon substrate.

Figure 4.9 and Figure 4.10 are SEM pictures of a vernier gauge at room temperature (298 K) and 20 K. The results for CTE measurements of the microgauge sensor are shown in Table 4.3. Here, the values of α_{Si} at cryogenic temperatures are obtained from previous study [112], while the values of α_{SiN} are determined by equation (4.12). The average CTE values of silicon nitride thin films from twenty measurements at cryogenic temperatures are shown in Figure 4.11. In comparison with the existing results, the CTEs of LPCVD silicon nitride thin films at room temperature, 1.6×10^{-6} K^{-1} [113] and 2.3×10^{-6} K^{-1} [114], have been reported. The lower measured CTE value at cryogenic temperatures can be explained through a consideration of the intermolecular forces of a material [72]. The intermolecular potential-energy curve, as shown in Figure 4.12, is not symmetrical. Therefore, as the temperature of the molecules is decreased, its mean position relative to its neighbors becomes smaller; that is, the material contracts. The rate at which the mean spacing of the atoms decreases with temperature decreases as the temperature of the silicon nitride decreases; thus, the CTE decreases as the temperature decreases.

To solve the curvature problem of the microshutter devices caused by the mismatch of CTEs, one possible solution is to tune parameters in microfabrication steps as discussed in Chapter 2. The principle is to compensate the thermal stress at 30 K with induced residual stress during fabrication. The other possible solution is to deposit a material with a similar CTE value as silicon nitride as a top layer on the microshutter

82
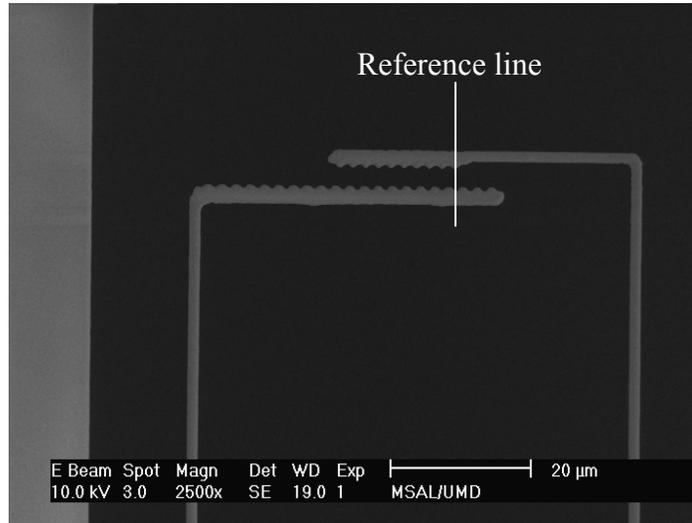
Figure 4.9: SEM picture of a vernier gauge for CTE measurement at 298 K.
(Dimensions: $L_t = 510$ μm, $W_t = 30$ μm, $L_s = 20$ μm, $W_s = 2$ μm, $L_i = 300$ μm, $W_i = 2$ μm)
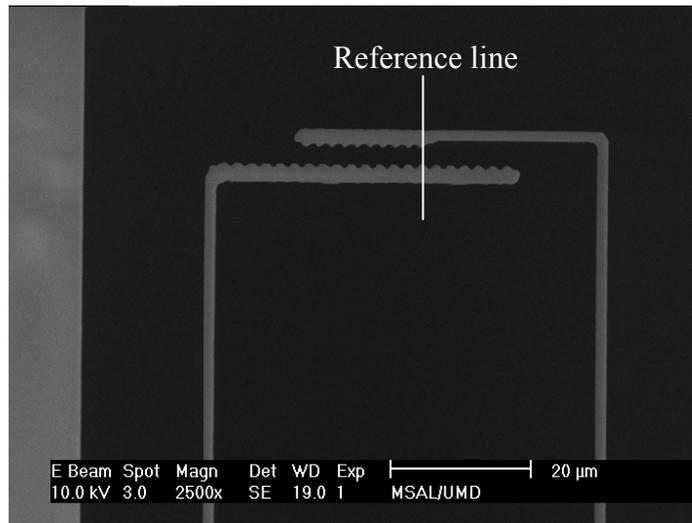
Figure 4.10: SEM picture of the same vernier gauge shown in Figure 4.9 at 20 K.
(Measured displacement $\delta_v = 4.8$ μm)

device, which will form a "sandwich" composite structure. Since the top layer and the bottom layer (silicon nitride) of the microshutter device have similar CTE values, it can keep flat surface at 30 K even though the CTEs of intermediate layers (aluminum and cobalt/iron) are different. One important criterion for the selection of this material is that it should be compatible with the fabrication processes of the microshutter device.

Table 4.3: CTE measurement results of silicon nitride thin films. (L_t = 510 µm, W_t = 30 µm, L_s = 20 µm, W_s = 2 µm, L_i = 300 µm, W_i = 2 µm)

T_1 (K)	T_2 (K)	$T = (T_1 + T_2)/2$	ΔT	Displacement δ_v (µm)	α_{Si} ($\times 10^{-6}$ K^{-1})	α_{SiN} ($\times 10^{-6}$ K^{-1})
298	200	249	98	-0.25	2.05	1.99
200	100	150	100	2.55	0.53	1.09
100	50	75	50	2.25	-0.52	0.47
50	20	35	30	0.25	-0.04	0.14
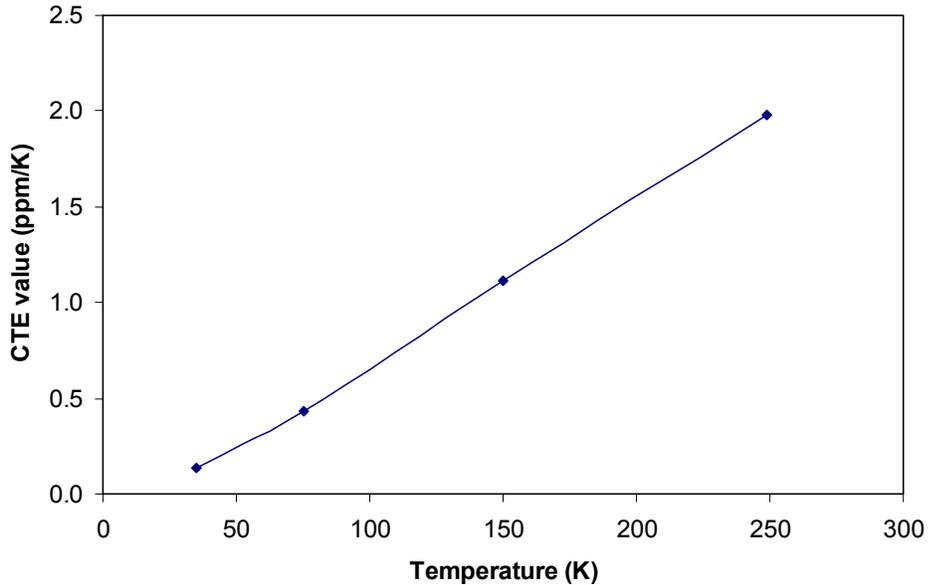
Figure 4.11: Coefficients of thermal expansion of silicon nitride thin films at cryogenic temperatures.
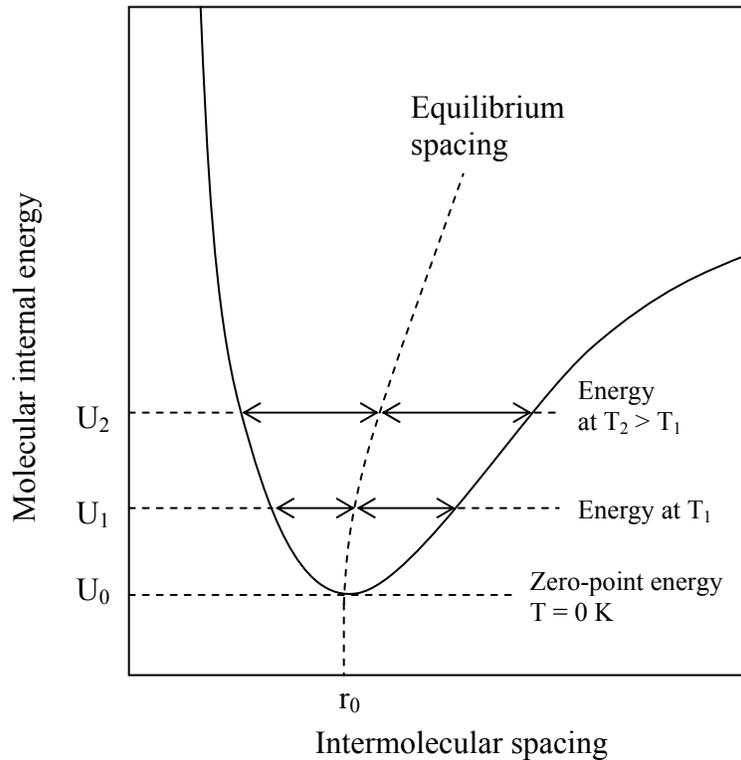
Figure 4.12: Variation of the intermolecular potential energy for a pair of molecules.

4.6 Discussion

The thickness of the thin film will not influence the measurement results as discussed in the design of the microgauge sensor. However, it has been found that the microgauge sensors with thickness less than 0.2 μm tend to break or stick to substrates even after supercritical drying. Apparently, these structures have small mechanical restoring forces to the disturbance of rinsing liquids, which produce relatively large surface-tension forces during the drying process.

The lateral etching of silicon (undercut) in KOH solution during the fabrication processes will change the effective lengths of the test beams and induce measurement

errors. The variations in the beam lengths depend on the etching time in KOH solution and are less than 10 μm in the fabricated microgauge sensors. To minimize this error, the effective lengths of the test beams utilized in the analytic model are measured directly by the SEM function. Even so, the undercut regions, unlike the beam structures of the microgauge sensors, will undergo biaxial stresses after release or during cryogenic tests. However, since the lengths of these undercut regions are much smaller compared with the designed lengths of the test beams, this effect is neglected.

4.7 Summary

A novel passive microgauge sensor based on the mechanical amplification technique is designed, fabricated, and characterized to measure the residual stress and the CTE for LPCVD silicon nitride thin films. Not only the average value but also a local knowledge of the residual stress can be obtained using the microgauge sensor. Furthermore, the measurement result is independent of thin-film thickness and process variations, which are key limiting factors for other techniques. An analytic model based on beam theory is developed to analyze the measurement results. Compared with ANSYS simulations, this model has negligible errors in a small strain region and only underestimates the real stress by 3.1% in a high strain region.

The residual stresses of two LPCVD silicon nitride thin films are characterized to determine the appropriate one for the fabrication of the microshutter arrays. From the test results, even though the second type (type B) of the silicon nitride thin film demonstrates a lower stress value, buckling of the torsion bar on the microshutter device may occur due to its compressive residual stress. To solve the curvature problem of the microshutter

devices, the CTEs of the silicon nitride thin film at cryogenic temperatures are studied and reported for the first time. The measurement results can be used to understand the thermal stress of this silicon nitride thin film at 30 K, and strategies to compensate this thermal stress are also discussed in this chapter.

CHAPTER 5

MECHANICAL-AMPLIFIER ACTUATORS FOR FATIGUE STUDY OF LPCVD SILICON NITRIDE THIN FILMS

Due to the rapid innovation of MEMS technologies over the last few decades, a variety of novel micro-scale machines and sensors have been developed. Associated with these advances in design, fabrication, and packaging of microsystems is an expansion of the set of materials available to MEMS designers. In order to ensure performance and reliability of MEMS devices over long periods of time, it has become increasingly important to understand the time- and cycle-dependent degradation of MEMS materials in their operating environment.

Fatigue, the failure of a material at less than its ultimate strength after a number of cyclic loadings, is the most important and commonly encountered mode of failure in structural materials. Mechanisms for the fatigue of ductile and brittle materials at macro-scale have been generally established after a century of research. However, the study of bulk materials in fatigue failure can not be directly applied to MEMS thin film structures [115-117].

The characterization of fatigue properties on the micro-scale is challenging due to the small dimensions of test devices. In previous research, several test devices were designed and fabricated. Sharpe *et al* [118] developed a 3.5 μm thick and 50 μm wide tensile specimen under tensile cyclic loadings to study reliability of polycrystalline silicon. Similar micro-structures were adopted for tensile cyclic loadings of LIGA (a German

acronym for lithography, electroplating, and molding) nickel films [119]. Although the direct tension test is an effective method for fatigue characterization, the requirements for strain measurement and sample alignment are stringent. Another approach is to integrate test specimen and setups with electrostatic actuation on the same chip. Ballarini *et al* fabricated arrays of comb actuators with a notch, operating at their resonant modes during the test [120]. The deformation of the specimen, which would be converted into propagation of the crack at the notch, was recorded during the experiment. Their analysis was based on measured deformations and extensive finite-element-analysis (FEA) modeling. Van Arsdell and Brown used resonating circular comb drive actuators with a notch to detect damage under repeated loadings according to the same operation principle [121]. However, all these techniques mainly focused on conductive polycrystalline silicon thin films and are difficult to utilize in a cryogenic environment with their designed setups.

The elements of the microshutter arrays are made of LPCVD silicon nitride thin films with suspended torsion beams, as discussed in Chapter 1. Since the microshutter arrays must operate in outer space (a cryogenic vacuum environment) reliably over a 10 year mission lifetime without repair after launch, it is critical to understand the fatigue failure of the silicon nitride thin films at cryogenic temperatures during expected operating cycles.

This chapter presents a novel design of electrostatic MEMS devices (mechanical-amplifier actuators) with dimensions similar to the elements of the microshutter arrays to emulate torsional operating stress for fatigue study of the silicon nitride thin films [122, 123]. In order to obtain different stress levels without high applied voltage, mechanical

amplification of mechanical-amplifier actuators is achieved based on a resonant technique. The test devices are fabricated using surface micromachining technique in combination with deep reactive ion etching (DRIE). Additionally, all experiments are performed inside the focused-ion-beam (FIB) system with the cryogenic measurement setup as discussed in Chapter 2. In the end of this chapter, the fatigue test results of mechanical-amplifier actuators at room and cryogenic temperatures are reported, and followed by a discussion.

5.1 Actuation mechanisms in MEMS devices

In MEMS device, the forces required for mechanical movement can be obtained using electrostatic, thermal, magnetostatic, or piezoelectric actuation. To date, an electrostatic actuation is the most prevalent technique due to its virtually zero power consumption, possible small electrode size, and relatively short switching time. However, in many cases, it requires an actuation voltage of $30 - 80$ V even to achieve a small movement distance (~ 1 μm). Conversely, thermal actuation relies on the thermal expansions of thin film materials at high temperatures. This design generally needs to consume relatively high power for Joule heating and the response is slow. The advantage of this actuation mechanism is the low required input voltage ($3 - 5$ V), which can be easily achieved using CMOS technology. For magnetostatic and piezoelectric actuations, the actuation voltages can be small ($3 - 20$ V) with relatively low power consumption. The only disadvantage is that the deposition of magnetic or piezoelectric materials may lead to complicated fabrication processes. Table 5.1 is a comparison of these actuation mechanisms.

Table 5.1: Comparison of actuation mechanisms in MEMS devices.

	Voltage	Current	Power consumption	Switching time	Contact force	Fabrication method
Electrostatic	High	Low (~zero)	Low (~zero)	Short	Medium	Simple
Thermal	Low	High	High	Long	Large	Simple
Magnetostatic	Low	High	High	Long	Small	Complex
Piezoelectric	Medium	Low (~zero)	Low (~zero)	Medium	Small	Complex

5.2 Design of mechanical-amplifier actuator

For most MEMS devices, the maximum stress level during operation is usually kept low to prevent fracture or fatigue failure at an early stage. However, to study fatigue properties of structural materials, the stress level must be large and controllable. Among different actuation mechanisms in MEMS devices, electrostatic actuation is utilized in this study since it can provide fast response and relatively simple fabrication processes. The use of electrostatic actuation to achieve high stress levels is challenging due to the limitation of applied voltage across a fixed gap. If the gap between two electrodes in a parallel-plate actuator (capacitor) is large, the actuation voltage becomes extremely high. On the other hand, if the gap is small, there is insufficient room for movement to introduce the required high stress levels on the structures.

Thus, a new mechanical-amplifier actuator based on a resonant concept is proposed to study fatigue properties of the microshutter arrays. The design principles are to separate the location for applying electrostatic energy with the location for creating physical movement, and to utilize the maximum response in a physical system (mechanical,

electrical, electromagnetic…) at its resonant frequency. In our device design, as shown in Figure 5.1, two resonators are connected serially with a common torsion bar. When operating, electrostatic energy is applied to *resonator 1* using a small gap between two electrodes. This energy is transferred to *resonator 2* via the common torsion bar. The vibration amplitude of *resonator 2* is then amplified by its quality factor when the frequency of pumped energy matches its resonant frequency, inducing high stress levels on the torsion bar. Based on this operation principle, the vibration amplification and amplitude of *resonator 2* can be controlled by the frequency and amplitude of the input electrostatic energy to *resonator 1*. In this design, *fixed beam 1* is used to increase lateral stiffness to prevent non-torsional movement on the torsion bar without significant energy loss during operation, and the rotation of *resonator 2* will cause a maximum torsional stress at the fixed end. The dimensions of the mechanical-amplifier actuators are presented in Table 5.2.
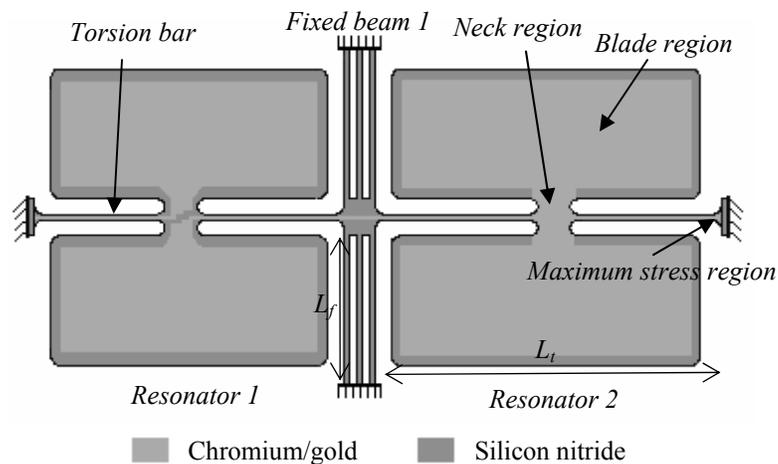
Figure 5.1: Schematic diagram of a mechanical-amplifier actuator for fatigue testing.

Table 5.2: Dimensions of mechanical-amplifier devices.

Torsion bar (μm)		Blade region (μm)		Neck region (μm)		Fixed-beam 1 (μm)		Thickness (μm)
L_t	W_t	L_b	W_b	L_n	W_n	L_f	W_f	T
108	2	95	35	15	5	40.5	0.8	0.5

An analytic model is developed to estimate the stress level on a mechanical-amplifier actuator. For a given torque T applied to a torsion bar, the maximum shear stress can be expressed as [124]

$$\tau_{\max} = \frac{3T}{8ab^2}[1+0.6095\frac{b}{a}+0.8865(\frac{b}{a})^2-1.8023(\frac{b}{a})^3+(\frac{b}{a})^4] \quad \text{for } a \geq b \qquad (5.1)$$

where a is half the long edge of the rectangular section, and b is half the short edge. The torque T is related to the twist angle θ by

$$T = \frac{\theta KG}{L} \qquad (5.2)$$

and

$$K = ab^3[\frac{16}{3}-3.36\frac{b}{a}(1-\frac{b^4}{12a^4})] \qquad (5.3)$$

Here, L is the torsion bar length, and G is the modulus of rigidity. The above equations neglect the stress concentration at the end of the torsion bars, and are only applied to predict maximum shear stress of *resonator 2* as shown in Figure 5.1. However, this model provides important guidelines for the design of the mechanical-amplifier actuator.

5.3 Device preparation

Fabrication of the mechanical-amplifier actuators began with a double-polished, thin silicon wafer (250μm) coated with 0.5 μm thermal oxide and 0.5 μm low-stress LPCVD

silicon nitride (residual stress of silicon nitride: 183.4 ± 14.7 MPa) on both sides. The basic process steps are shown in Figure 5.2, and specific details are described below. Prior to metal deposition, the wafer was cleaned two minutes in a sputtering chamber (AJA^{TM} ATC-1800) with flow rate of 20 sccm for argon gas, pressure of 28 mTorr, and RF power of 18 Watt. A layer of 100 Å chromium and a layer of 500 Å gold were then deposited using the sputtering system. The process parameters for chromium and gold deposition were flow rate of 20 sccm for argon gas, pressure of 5 mTorr, and DC power of 200 Watt. In this step, the wafer was rotated in the chamber to obtain better uniformity. The measured deposition rates were 2.0 Å/sec and 8.1 Å/sec for chromium and gold, respectively.

(a)Chromium/gold deposition and patterning for the electrodes of resonator 1 (first mask)

(b) Define the test structure on SiN using reactive ion etching (second mask)

(c) Pattern the backside and use DRIE to etch through thin silicon substrate (Third mask)

(d) Remove the oxide layer (etch stop of DRIE)
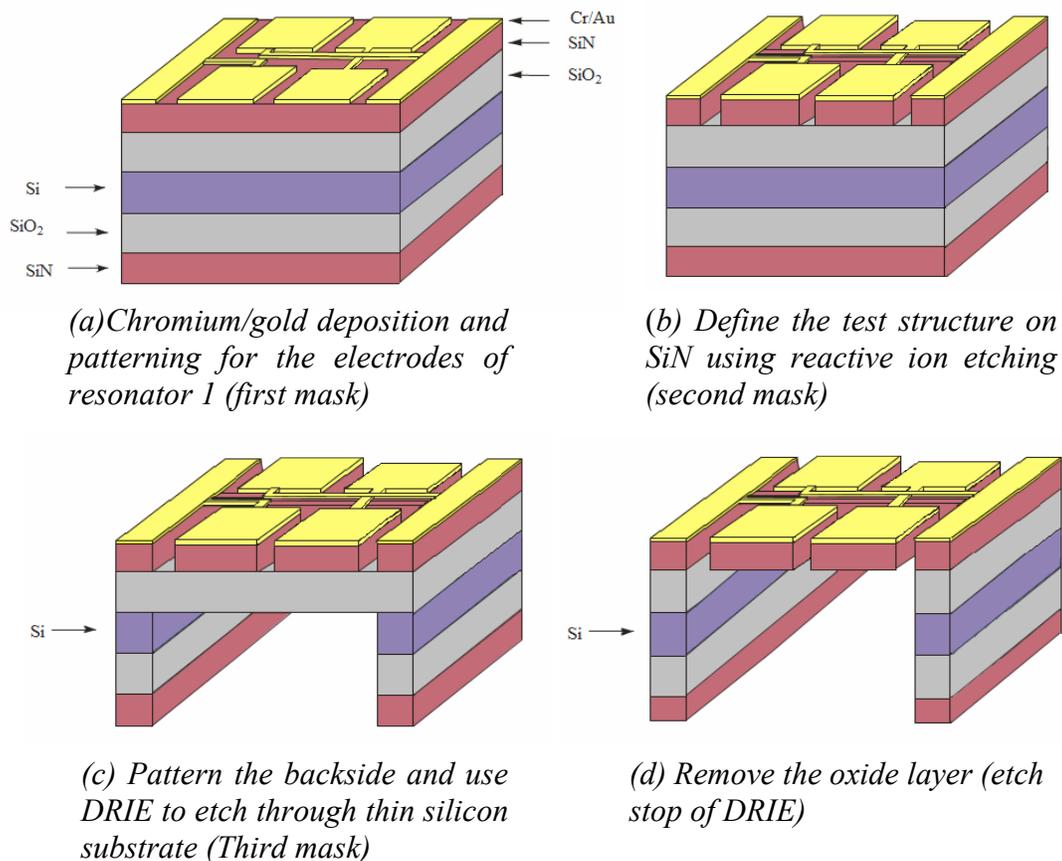
Figure 5.2: Basic process flow for mechanical-amplifier actuators.

A standard lithography process (Table 3.2) was then performed, and the patterned photoresist with a thickness of 5.7 μm was used as a masking layer for chromium and gold etching. The chromium and gold layers were etched using Transene[TM] TFD chromium etchant and Transene[TM] TFA gold etchant with the etch rate of 25.0 Å/sec and 57.5 Å/sec, respectively, to form the electrodes on *resonator 1*. After this step, the photoresist was removed using a photoresist stripper (Baker Aleg-625) heated to 45 °C.

Next, the standard lithography process was performed again to form a masking layer for patterning the silicon nitride structural layer. The silicon nitride thin film was etched in a reactive ion etcher (Trion[TM] Minilock RIE system) using CF_4 and O_2. The process parameters were pressure of 250 mTorr, flow rates of 50 sccm and 5 sccm for CF_4 and O_2, respectively, and a RF power of 100 Watt. The silicon nitride etch rate was 180 nm/min, and the photoresist etch rate was around 80 nm/min. After etching the silicon nitride, the photoresist was kept to protect the underneath chromium/gold layers for further processes.

Once the processes for the front side were finished, a thick photoresist (10 μm) was spun on the backside of the wafer, followed by a lithography step (Table 5.3) to pattern open windows on the photoresist for subsequent deep reactive ion etching (DRIE). In this process, front-to-back (wafer) alignment was performed using the feature of infrared (IR) backside alignment in the contact aligner (Quintel[TM] Q4000). The front side of the wafer was then bonded to a handle wafer using an adhesive (Crystalbond[TM] 555). The silicon nitride and the thermal oxide in the open windows on the backside were removed by the RIE system and buffered oxide etchant (J.T.Baker[TM] Buffered Oxide Etch), respectively.

Table 5.3: A lithography process for using thick photoresist.

Step	Recipe
Photoresist coating	Photoresist: AZ 9245 (Clarinet[TM]) Spin coating: 300 rpm for 5 seconds, then 1000 rpm for 40 seconds Soft bake: 110 °C for 120 seconds
Exposure	Dose: 720 mJ Contact aligner: Quintel[TM] Q4000
Photoresist development	Developer: AZ 400 K mixed with DI water (1:3) Developing time: 3 minutes

The silicon substrate was etched through from the open windows on the backside using DRIE in Integrated Sensing Systems, Inc. (ISSYS). This step is critical due to the requirement of keeping vertical etching profiles in DRIE [125]. In principle, DRIE relies on generation of high plasma densities to achieve a high etch rate while operating at low pressure to increase ion directionality. When etching silicon trenches with depths in excess of 300 μm, the neutral flow conductance decreases drastically according to the standard vacuum theory [126, 127]. This impedes both the transport of etchant species to the surface bottom and the removal of etching byproducts. Therefore, as the depth of etched trenches increases, the trench profile (verticality) and silicon etching rate can deteriorate quickly. To alleviate this effect, a thin silicon substrate (250 μm) was used in the fabrication of the mechanical-amplifier actuators. A comprehensive study of DRIE processes parameters for anisotropy and profile control can be found in [125, 128, 129].

During the DRIE step, the thermal oxide on the front side was used as an etch stop. The selectivity of silicon to silicon oxide is usually greater than 100. This oxide layer was then removed with buffered oxide etch (BOE) and the wafer was released from the handle wafer with de-ionized (DI) water heated to 60 °C. Finally, the photoresist on both

sides of the wafer was stripped using acetone, followed by a methanol cleaning and drying process. The mechanical-amplifier actuator after fabrication is shown in Figure 5.3.
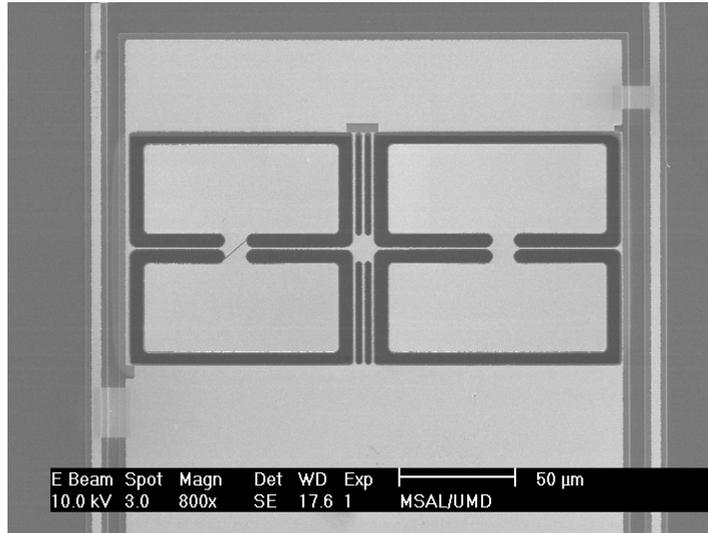
Figure 5.3: Micrograph of a mechanical-amplifier actuator after fabrication.

5.4 Experimental techniques

5.4.1 FIB system with a cryogenic measurement setup

In Chapter 2 and Chapter 3, a cryogenic measurement setup installed inside a FIB system was introduced to characterize the Young's modulus and fracture strength of LPCVD silicon nitride thin films at room and cryogenic temperatures [76, 77]. The FIB system with the cryogenic measurement setup was also used in the study of the fatigue property of silicon nitride thin films and the key components of this system are briefly reviewed below. (The detail can be found in Chapter 2) The FEI 620 FIB used in our experiment is a dual beam system, with ion and electron columns, permitting ion milling

and *in situ* scanning electron microscopy (SEM). This system also has the ability to deposit platinum (Pt) by ion-induced metal-organic-chemical-vapor deposition (MOCVD)[130].

Figure 2.3 (in Chapter 2) shows the configuration of the measurement setup inside the FIB system. A lead-zirconate-titanate (PZT) translator powered by a DC voltage was attached on a 3-D stage controlled by three stepper motors. A micro-needle, for use as a ground electrode in actuating mechanical-amplifier actuators (discussed in the next section), was then mounted on the PZT translator with a copper wire as an electrical conduction path. The combination of the PZT translator and the 3-D stage provides the capability to manipulate the micro-needle. In addition, the device stage shown in Figure 2.3 can be rotated and tilted.

5.4.2 Vibration frequency determination

In the FIB system, an SEM image is formed by collecting the secondary electron signal when a fine electron beam is scanned over the surface of a specimen. The collected secondary electron signal varies with the topography and composition of the specimen. As discussed in Chapter 3, this principle can be applied to measure vibrating frequencies of a mechanical-amplifier actuator. Instead of scanning over the whole surface, a point electron beam was placed in a fixed position where the vibrating blade of a mechanical-amplifier actuator moved in and out of the electron beam path. This modulated the secondary electron signal with the frequency of vibration and this signal was acquired with an oscilloscope to determine the vibrating frequency. The mechanism of the vibration frequency determination inside the FIB system is shown in Figure 3.4.

5.4.3 Micro-needle ground electrode

In the configuration of a mechanical-amplifier actuator, a ground electrode under or above the electrodes of *resonator 1* is required to actuate this device. One possible solution to fabricate this ground electrode is to utilize the silicon substrate under *resonator 1*. In this case, the DRIE etching step mentioned in Figure 5.2 would only remove the silicon from under *resonator 2*. The thermal oxide under *resonator 1* is utilized as a sacrificial layer and could be etched away using a surface micromachining technique to release the structure of *resonator 1*. However, the disadvantages of this method are a more complicated fabrication process (including sacrificial layer etching and supercritical drying for stiction release) and a fixed electrode gap.

An alternative approach is to use a micro-needle ground electrode as shown in Figure 5.4. The technique to make the micro-needle ground electrode is similar to the micro-repair technique for the microshutter arrays mentioned in Chapter 2. The micro-needle was first positioned to contact with a silicon nitride membrane coated with a chromium/gold layer. The needle was then welded to the membrane using ion-induced platinum deposition. The micro-needle with membrane was released from a substrate by milling away the connecting parts of the membrane to the substrate to form a ground electrode. The advantages of this method are the freedom to move the ground electrode, which can prevent the pull-in phenomenon during operation, and a relatively simple fabrication process of the mechanical-amplifier actuators.
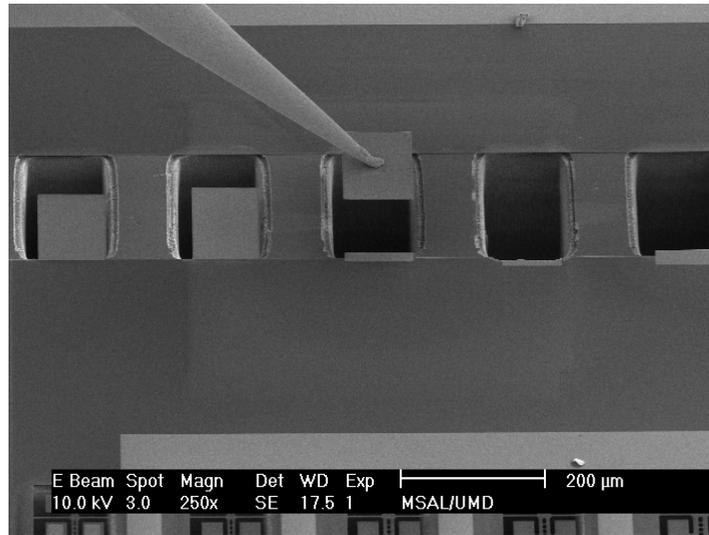
Figure 5.4: SEM picture of a micro-needle welded to a nitride membrane coated with a chromium/gold layer.

5.4.4 Testing procedure

When testing a mechanical-amplifier actuator, the micro-needle ground electrode was positioned above *resonator 1* with an appropriate height (approximately 5-8 μm) and connected to electrical ground as shown in Figure 5.5. Two AC voltages (sinusoidal waveforms) with 90° phase difference were applied to the electrodes on *resonator 1*, causing the blades of *resonator 1* to alternately move up and down. The pumped electrostatic energy was then transferred to *resonator 2* via the common torsion bar and driving *resonator 2* at its first resonant mode. The first resonant mode was determined by sweeping a range of frequencies around the expected value and monitoring the vibrating amplitude of *resonator 2*. Once the resonant mode was obtained, the device was excited at this frequency with fixed input voltage amplitude for a set period of time. Afterwards, the frequency response was again evaluated by sweeping around the excitation frequency. Over time, this permitted measuring any change in resonant frequency due to the

100

accumulation of fatigue damage. Since the vibrating amplitude of *resonator 2* is large to introduce high stress level on the torsion bar, the relationship between the twist angle of the torsion bar and the blade displacement is not linear. In this region, the beam theory is not applicable. Therefore, the twist angle can not be obtained by measuring the blade displacement, leading to the equation (5.1) useless in determining the maximum shear stress. To solve this geometric nonlinearity, an ANSYS FEA model was built. Given the well-established properties (Young's modulus, Poisson's ratio, and density) of low-stress LPCVD silicon nitride thin films and the measured vibrating amplitude of *resonator 2*, the maximum stress on the structure can be determined from this model. Therefore, the relationship between fatigue life and stress was obtained.

Resonator 1   Resonator 2

Chromium/gold   Silicon nitride
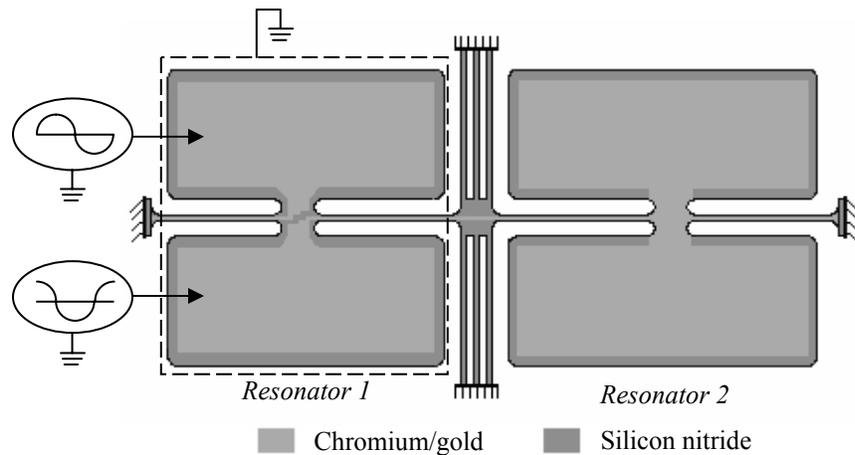
Figure 5.5: Schematic diagram for actuation of a mechanical-amplifier actuator. The rectangular with a dashed line represents the micro-needle ground electrode positioned above *resonator 1*.

During the testing of the mechanical-amplifier actuator, *resonator 1* did not operate at its first resonant mode since the first resonant frequencies of both resonators are not the same (the difference is from the metal layer patterns and process variations). Furthermore,

the up-and-down movements of the blades of *resonator 1* can not match its resonant mode, which is a pure rotational movement. For a given twist angle θ of *resonator 2*, the maximum shear stress can be increased by varying the dimensions of a torsion bar as shown in (5.1). However, the mechanical-amplifier actuators were designed to emulate the operation of the microshutter devices with similar dimensions and without size effect [131]. Therefore, instead of having a short and thick torsion bar, a mechanical-amplifier actuator with a notch structure was adopted in this study to further increase the stress level (Figure 5.6). The notch structure used here was defined using ion milling with low ion energy of 5 KeV and small milling current of 4 pA.
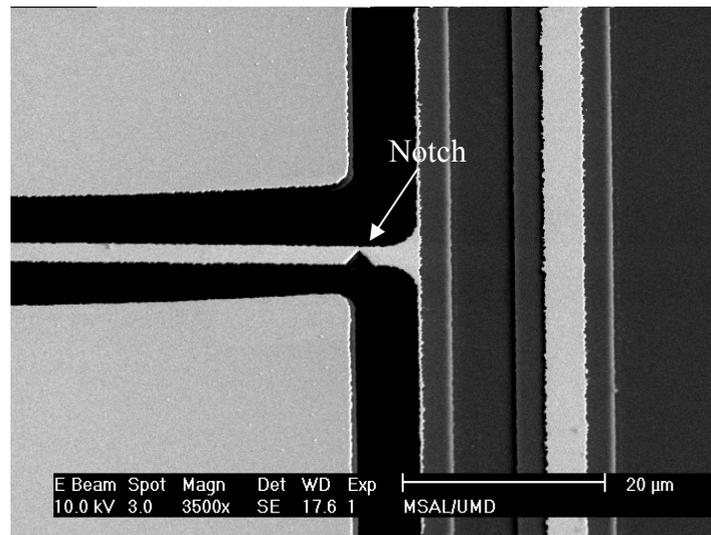
Figure 5.6: SEM picture of a mechanical-amplifier actuator with a notch on the torsion bar.

5.5 Experimental results

5.5.1 Room temperature measurements

All devices were tested in a room-temperature environment (Pressure: 10^{-6} Torr, Temperature: 23 ± 1 °C) first with input voltages varied from 8.8 V_{rms} to 28.3 V_{rms} using the testing procedure described above, while the test duration ranged from 5 seconds to 8.5 hours, or 10^5 to 10^9 cycles. Figure 5.7 shows a mechanical-amplifier actuator with *resonator 2* at its first resonant mode. In this experiment, the input voltages to *resonator 1* were 10.6 V_{rms} and the resonant frequency of *resonator 2* was found to be 33.258 KHz. The corresponding resonant spectrum of *resonator 2* is presented in Figure 5.8. In addition, mechanical amplification between *resonator 1* and *resonator 2* is shown in Figure 5.9. In this figure, small movement of *resonator 1* introduces large vibration of *resonator 2* based on the principle described previously. ANSYS FEA models (Figure
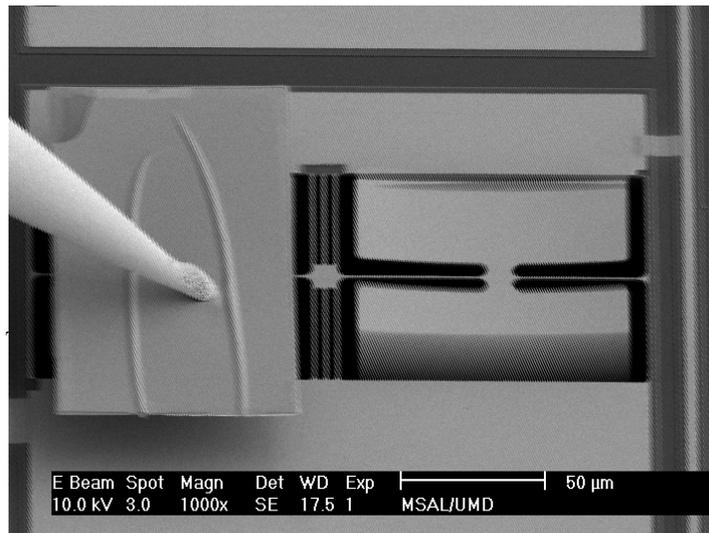
Figure 5.7: SEM picture of a mechanical-amplifier actuator under testing at room temperature with *resonator 2* at its first resonant mode.

5.10) with dimensions of the mechanical-amplifier actuator were built to calculate the maximum stress on a torsion bar for a given blade displacement, measured directly inside the FIB. The elements and parameters utilized in these models are presented in Table 5.4. Here, the stress concentration at the ends of a torsion bar with a radius of curvature r = 1.5 μm was simulated. Similarly, the notch tip radius was measured using SEM function and represented by a radius of curvature r = 0.2 μm in the FEA model. Linear and nonlinear analyses with different mesh sizes were performed for each data point to verify that there is no geometric effect in these models. The simulation results showed a linear increase of stress amplitude at small displacement (within 12 μm) and both linear and nonlinear analyses gave the same results. At higher blade displacement, the stress amplitude from the nonlinear analysis is larger than that from the linear analysis, which is in agreement with the nonlinear stiffening effect. Figure 5.11 presents the maximum operating stress on a torsion bar for different blade displacements according to these ANSYS models. From this figure, the mechanical-amplifier actuator with a notched torsion bar shows higher stress amplitude as a result of the introduced notched stress concentration.

Table 5.4: Elements and parameters of the mechanical-amplifier actuator utilized in ANSYS FEA model. The Young's modulus and the residual stress of the silicon nitride thin films are obtained from Chapter 3 and Chapter 4.

Element	Density (kg/m^3)	Young's Modulus (GPa)	Poisson's ratio	Residual stress (MPa)
Solid–92/Solid-187	3000 [32]	260.5	0.25	183.4
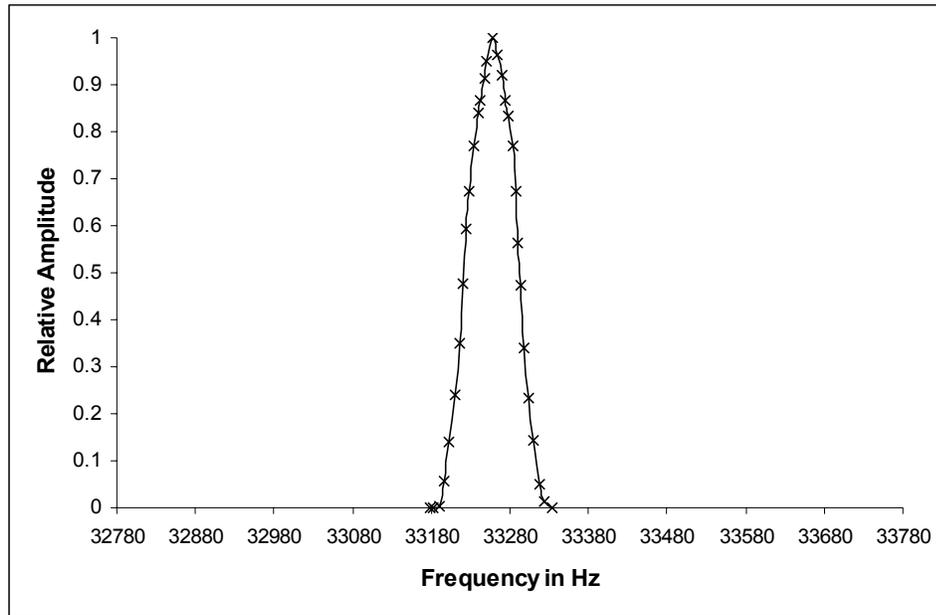
Figure 5.8: Resonant spectrum of *resonator 2* shown in Figure 5.7.
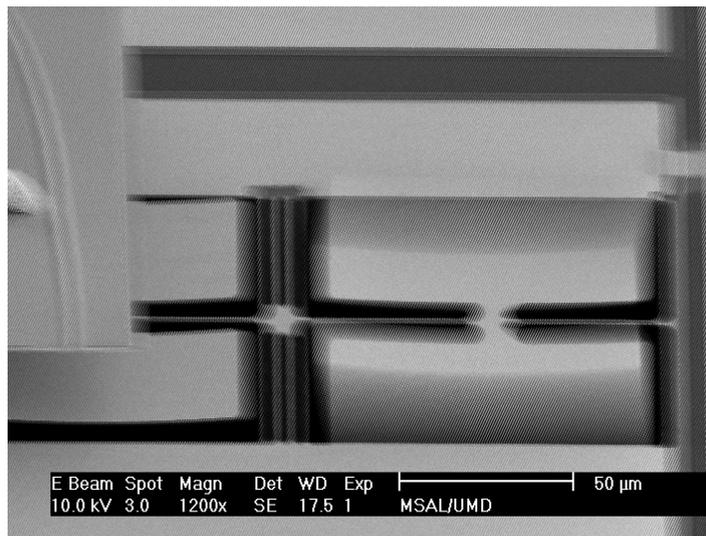
Figure 5.9: SEM picture of a mechanical-amplifier actuator to demonstrate mechanical amplification. *Resonator 1* (left) has small vibration while *resonator 2* vibrates largely at its first resonant mode.
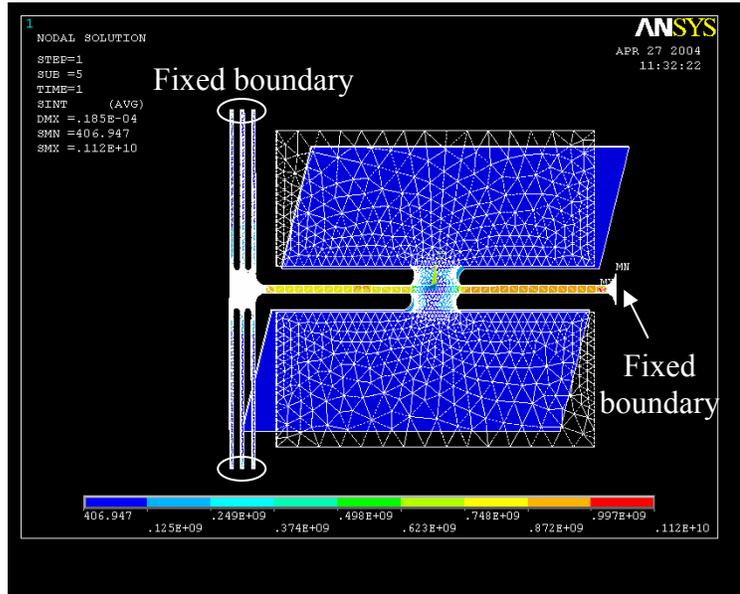
Figure 5.10: ANSYS FEA model used to calculate maximum stress on a torsion bar for a given blade displacement. Circles in this figure represent a fixed boundary.
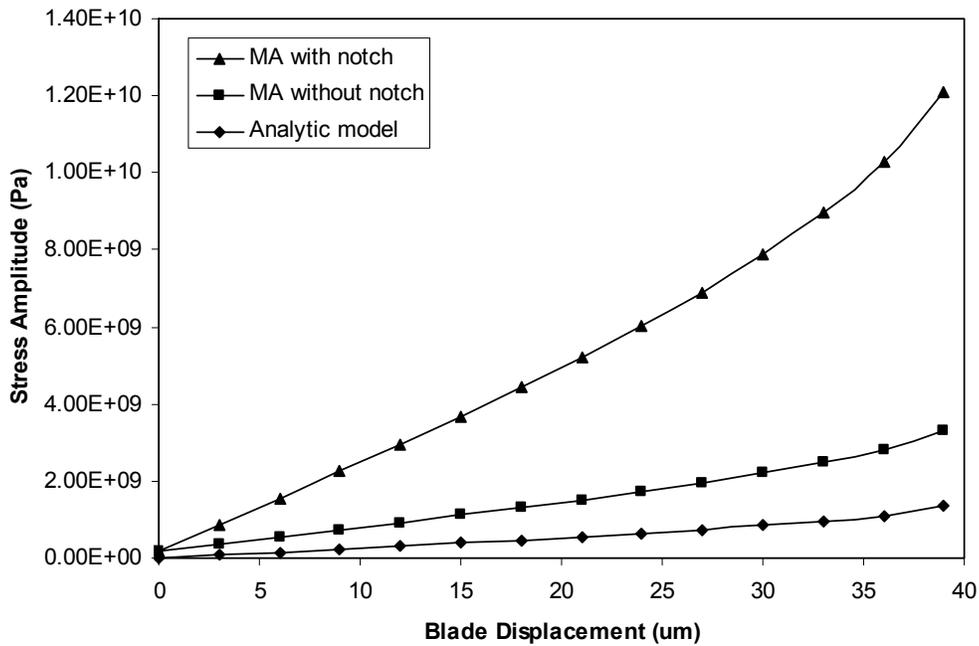
Figure 5.11: Maximum operating stress of the mechanical-amplifier actuator (MA) with different blade displacements at 298 K from ANSYS FEA model and analytic model.

Results from the stress-life testing of low-stress LPCVD silicon nitride are shown in Figure 5.12. When testing at the maximum operating stress over 6.6 GPa, the mechanical-amplifier devices exhibited time-delay failure. On the other hand, the mechanical-amplifier devices survived cyclic loadings even up to 10^9 cycles at lower operating stress. The resonant frequencies of these devices (at lower stress amplitude) were used to monitor variation of stiffness but no deviation of these frequencies was observed during experiment. Therefore, when subjected to sinusoidal, cyclic stress with amplitude below 5.8 GPa and a load ratio of 0.03, the low-stress LPCVD silicon nitride thin films did not display time-dependent degradation or failure up to 10^9 cycles in the testing environment.
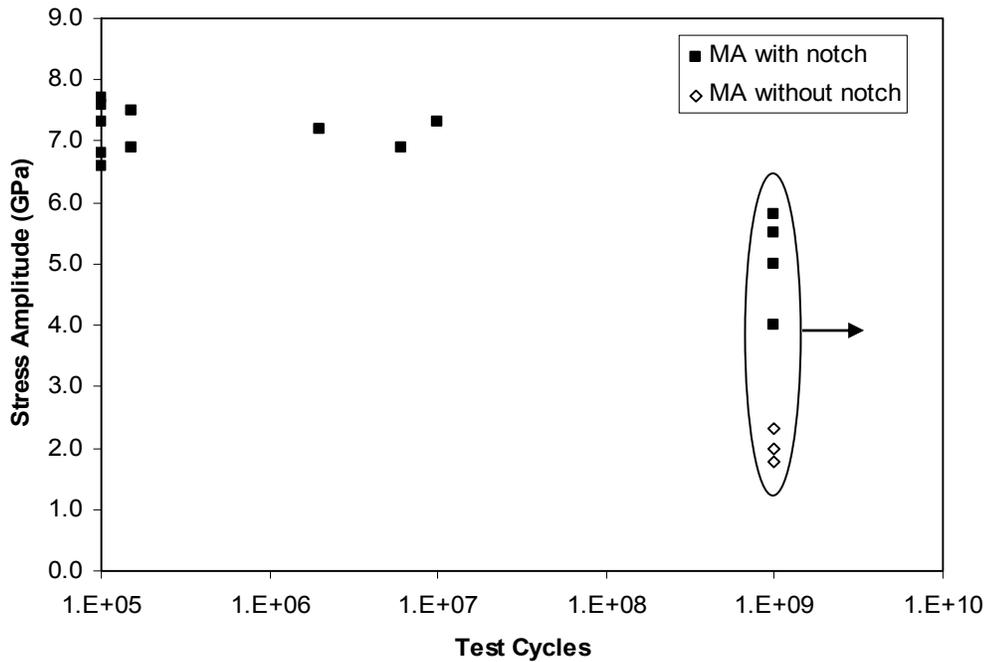
Figure 5.12: Stress-life testing data for low-stress LPCVD silicon nitride at 298 K. When testing at high stress level, test devices exhibited time-delayed failure. Conversely, the circle with a horizontal arrow indicates devices that did not fail under cyclic loadings up to 10^9 cycles when testing at lower stress amplitude.

The microstructure of a fatigue specimen (Figure 5.13) using low voltage SEM was used to establish the mode of crack advance without altering the surface by coating with conductive layers. The crack was observed to initiate at the notch tip and propagate along the remaining ligament of the notched torsion bar. Layer structures parallel to the direction of crack propagation and unidentified debris were found on the fracture surface, which are the proof of cyclic damage. An additional thin silicon dioxide layer was observed at the bottom of the cross-section due to incomplete etching of the etch stop after DRIE process.

(a)   (b)
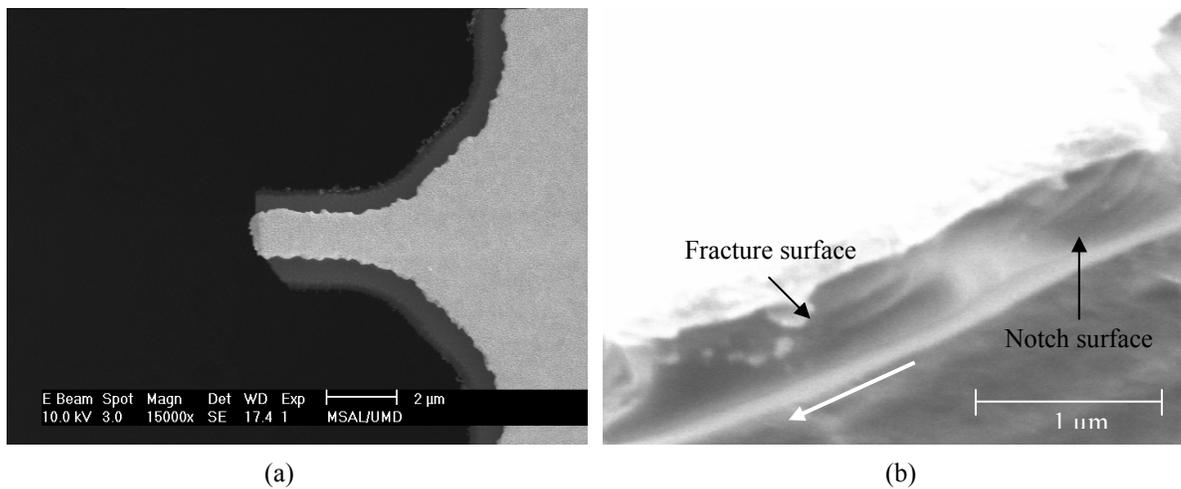
Figure 5.13: (a) Micrograph of a notched torsion bar that failed after ~6 million cyclic loadings at stress amplitude of 6.8 GPa. (b) Micrograph of the fracture surface. The arrow (white color) indicates the direction of crack propagation.

5.5.2 Cryogenic temperature measurements

After room temperature experiments were finished, the mechanical-amplifier actuators were cooled down to 30 K with the cryogenic measurement setup. Due to the mismatch of CTEs among silicon nitride, chromium, and gold layers, the blades of the mechanical-amplifier actuator curled up at cryogenic temperatures as shown in Figure 5.14. The micro-needle ground electrode was then carefully positioned above *resonator 1* with an appropriate gap to prevent contact between the ground electrode and the blades. In addition, a copper wire connecting to the helium exhausted tube (Figure 2.3) was used as a thermal path to cool down the micro-needle ground electrode.
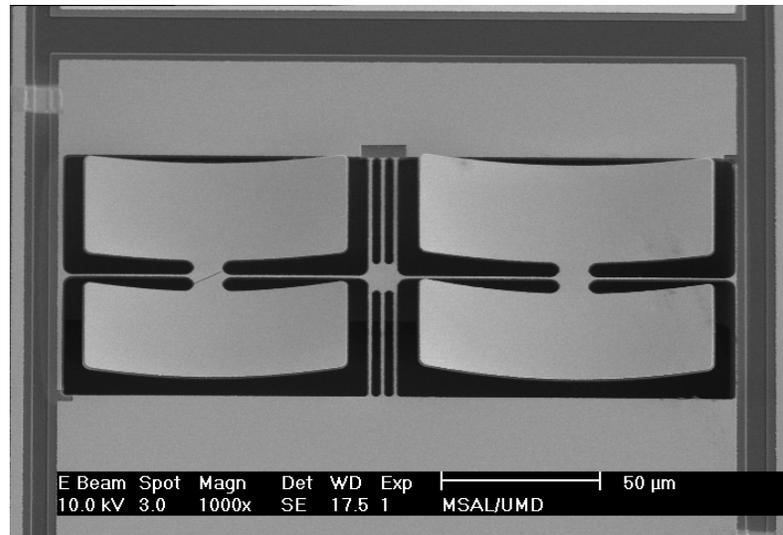
Figure 5.14: Micrograph of a mechanical-amplifier actuator cooled down to 30 K. The blades curl up due to the mismatch of CTEs among silicon nitride, chromium, and gold layers.

The cryogenic fatigue tests of the mechanical-amplifier actuators follow the same testing procedure as discussed in the previous sections, and all devices were tested in a cryogenic-temperature environment (Pressure: 10^{-8} Torr, Temperature: 30 ± 3 K) inside

the FIB system. In order to maintain constant helium flow during experiments, the test duration for each device ranged from 5 seconds to 50 minutes, or 10^5 to 10^8 cycles. A testing mechanical-amplifier actuator at 30 K with *resonator 2* at its first resonant mode is shown in Figure 5.15. In this experiment, the input voltages to *resonator 1* were 13.4 V_{rms} and the resonant frequency of *resonator 2* was found to be 35.156 KHz. Compared to the testing results at room temperature, the resonant frequency of *resonator 2* is increased at 30 K as a result of a higher value of the Young's modulus for silicon nitride thin films at cryogenic temperatures. The maximum operating stress on the torsion bar was determined from ANSYS FEA nonlinear models with a measured blade displacement. These analyses were based on the model in Figure 5.10 but also included thermal stress due to different CTE values of the composite structures on the torsion bar. The elements and parameters utilized in these models are presented in Table 5.5, and the simulation results are shown in Figure 5.16. In this figure, there is an existing pre-stress on the torsion bar even without any blade displacement. This pre-stress is mainly caused by the residual stress and the thermal stress of silicon nitride thin films at cryogenic temperatures.

Table 5.5: Elements and parameters of the mechanical-amplifier actuator utilized in ANSYS FEA model at 30 K. The properties of the silicon nitride thin films are obtained from the previous chapters.

	CTE value (K^{-1})	Young's modulus (GPa)	Residual stress (MPa)	Element
Silicon	1.30×10^{-6} [112]	125 [42]	0	
Silicon nitride	0.84×10^{-6}	266.6	183.4	Solid-92 / Solid-187
Chromium	3.74×10^{-6} [132]	279 [133]	-	
Gold	12.13×10^{-6} [132]	70 [42]	-	
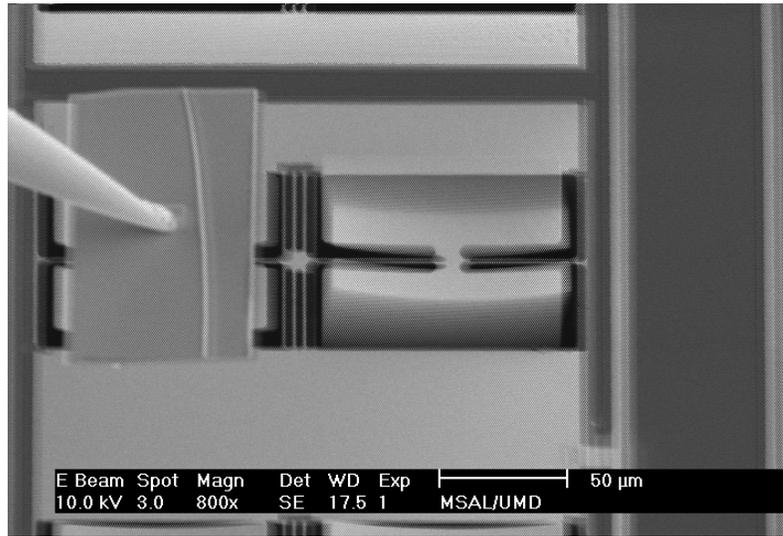
Figure 5.15: Micrograph of a mechanical-amplifier actuator under testing at 30 K with *resonator 2* at its first resonant mode.
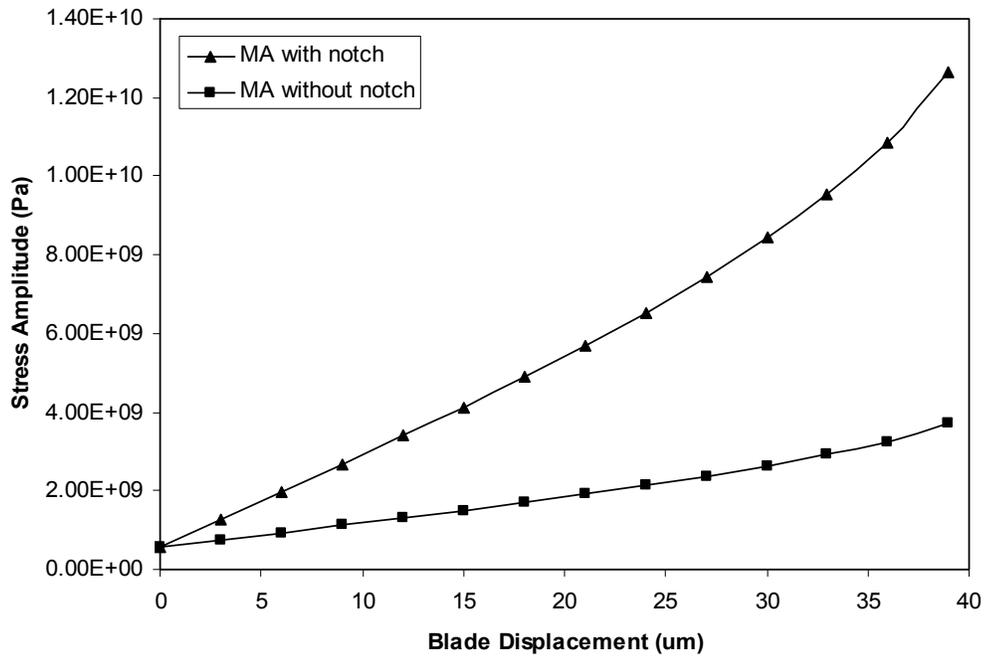
Figure 5.16: Maximum operating stress of the mechanical-amplifier actuator (MA) with different blade displacements at 30 K from ANSYS FEA model.

The stress-life testing results of the mechanical-amplifier actuators at cryogenic temperatures are shown in Figure 5.17. From these results, the specimen exhibited fatigue failure when testing at stress amplitude over 5.6 GPa at 30 K, and the lifetime of the silicon nitride thin films was found to increase monotonically with decreasing stress amplitude. With a 25% reduction in stress amplitude, the lifetime of the test devices can increase three orders in magnitude. Conversely, when testing at operating stress lower than 5.0 GPa with a load ratio of 0.11, the mechanical-amplifier actuators survived the cyclic loadings up to 10^8 cycles.
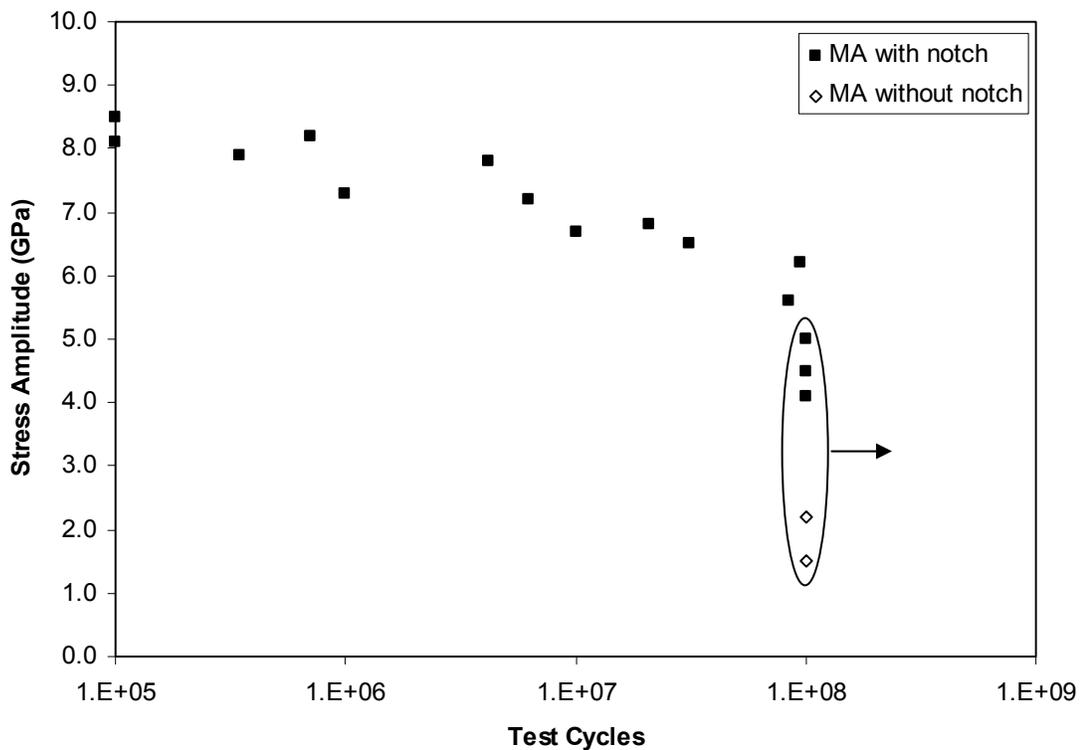

Figure 5.17: Stress-life testing data for low-stress LPCVD silicon nitride at 30 K. When testing at high stress level, test devices showed fatigue failure. On the other hand, the circle with a horizontal arrow indicates devices that did not fail under cyclic loadings up to 10^8 cycles at lower operating stress amplitude.

The resonant frequency of the test device was used to monitor the stiffness variation during cyclic loadings in the controlled cryogenic environment, and was observed to decrease monotonically before the device finally failed as shown in Figure 5.18. The change in resonant frequency means that the torsion bar of the mechanical-amplifier actuator becomes more compliant during the test. This behavior strongly suggests that the failure of silicon nitride thin films occurs as a result of damage accumulation.
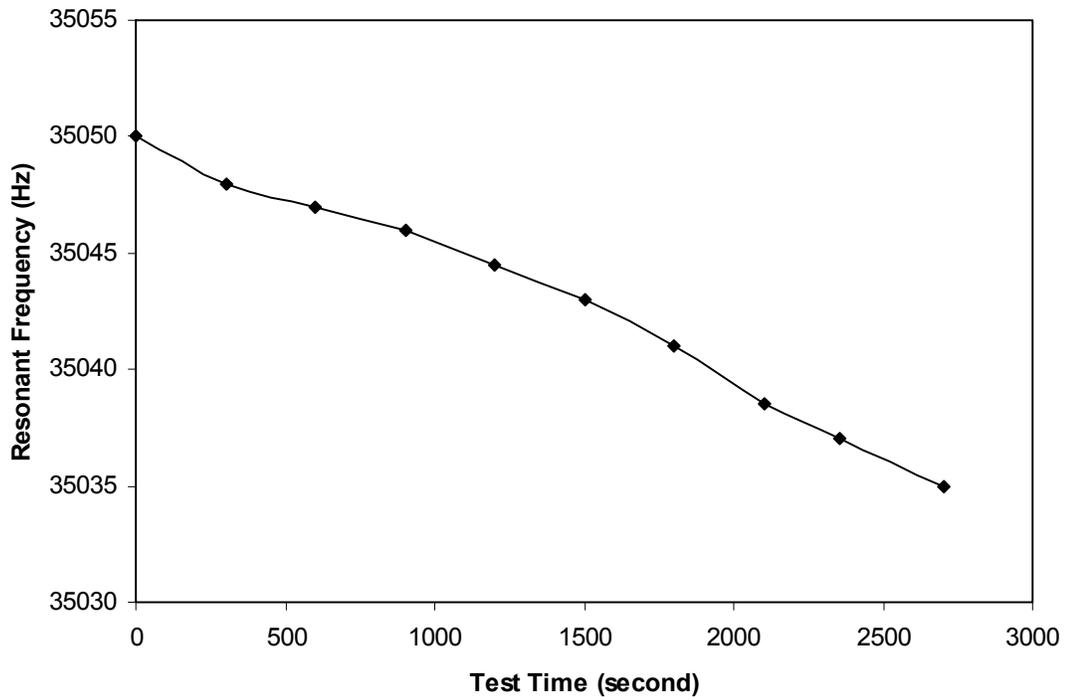
Figure 5.18: Variation of resonant frequency with time for a mechanical-amplifier actuator during cryogenic fatigue testing (Test cycles: 10^8 cycles at stress amplitude 6.2 GPa).

5.6 Discussion

According to the design of the mechanical-amplifier actuators, the vibration of *resonator 2* can be controlled by the frequency and amplitude of the applied electrostatic energy. However, the maximum blade displacement of *resonator 2* was found to be 32

μm during experiment. The limitation was caused by pull-in energy loss and intrinsic material damping. For high input voltages, the blades of *resonator 1* tried to pull in with the micro-needle ground electrode. Instead of making torsional motion on a torsion bar, most energy was used to create up-and-down movement which was compensated by *fixed-beam 1* and became ineffective in actuating *resonator 2*.

Several uncertainties may cause errors in the determination of maximum operating stress from the ANSYS FEA models. First, the cross sections of torsion bars are not perfectly rectangular due to the fabrication process. The curvature of these bars is difficult to measure, especially for thin film materials. Second, the small variation of curvature at the notch tip during each ion milling process, and the residual stress of chromium/gold thin films were not considered in these models. Third, *resonator 1* was neglected in the FEA model for simplicity due to its relatively small movement. In addition, the applied voltages to the test devices disturbed electron beam signals and caused distortion of scanning electron micrographs. This may introduce errors in the measurements of blade displacements. However, based on the current design of the mechanical-amplifier device, *resonator 2* vibrates only when the frequency of the applied voltages is close to its resonant mode. This mechanism can be utilized as a calibration method by measuring the blade displacement of a static *resonator 2* with the same applied voltages (but not at the resonant frequency). Furthermore, the test devices were titled with an angle (52°) for better observation of vibration amplitude during experiments. The corresponding error in stress measurement due to the distorted images is estimated to be less than 0.4 GPa.

The fracture strength of silicon nitride thin films varies from 6.9 GPa at 298 K to 7.9 GPa at 30 K as discussed in Chapter 3. However, no fracture failure was observed even when the devices were tested at stress amplitude higher than the fracture strength. This can be explained by the increase of the fracture strength of the silicon nitride composite structure (silicon nitride coated with chromium and gold) due to incorporation of surface damage into coating layers and crack healing effects during deposition process [134]. The usage of low ion energy and chromium or gold protective layers during ion milling process has been demonstrated to minimize FIB-induced damage [135, 136]. Even so, it is inevitable to introduce gallium implantation and surface damage on the notched torsion bars, which may decrease fatigue resistance at high operating stress. However, the test results in our study can provide conservative stress amplitude for reliability design of a microstructure using silicon nitride thin films in a vacuum environment.

From this work, the mechanical-amplifier actuators displayed time-delayed failure in a vacuum environment at both room temperature and cryogenic temperatures. In previous study, the fatigue failure of polycrystalline silicon in ambient air was observed [137], and it is attributed to a mechanism involving the environmentally-assisted cracking of the surface oxide film. Although similar phenomena may exist for premature failure of silicon nitride materials, this mechanism is not applicable to our work since our experiments were performed inside a vacuum chamber. As the surface condition of test structures is a critical factor to induce premature failure, the observed damage on the notched torsion bar after ion milling can increase local stress amplitude and initiate a crack, which may explain the short lifetime of the test devices.

Comparing the test results at room temperature and cryogenic temperatures, the mechanical-amplifier actuators exhibit lower fatigue resistance at 30 K. Several mechanisms may be involved for this phenomenon. First, a non-zero pre-stress on the torsion bar at 30 K increases the mean stress, an average of the minimum and maximum operating stress, during the tests. Fatigue life has been demonstrated to decrease with high mean stress value, and can be estimated by several analytic models [138, 139]. Second, the tensile pre-stress and torsional operating stress form complex strain states during cyclic loadings. These multi-axial cyclic loadings also decrease fatigue life according to the previous experimental studies and modeling [140, 141]. Third, the residual gas inside the FIB chamber condensates on the test devices when these devices are cooled down to 30 K. The vacuum gauge of the FIB system indicates that the chamber pressure decreases two orders in magnitude when reducing temperatures from 298 K to 30 K. The condensated residual gas may initiate corrosion-fatigue failure of the mechanical-amplifier actuators during cyclic loadings. Further analysis and examination must be performed to understand this mechanism.

The number of cycles expected in the lifetime of the JWST microshutter arrays is 10^5 [142], three orders of magnitude less than our test cycles, and the maximum operating stress of the microshutter arrays is less than 3.5 GPa based on the current dimensional design [94]. From this study, even though the FIB-induced damage may reduce fatigue lifetime, the mechanical-amplifier devices with notch structures still survived 10^8 cyclic loadings at a maximum operating stress of 5.0 GPa. Therefore, the microshutter devices are not expected to display fatigue failure during their operation. However, the mechanical-amplifier actuators were fabricated separately from the micro-shutter arrays

using similar fabrication processes. To eliminate the influence of process variations to the fatigue life, an integrated mechanical-amplifier actuator has been fabricated with the micro-shutter arrays as shown in Figure 5.19. In this device, two electrodes above *resonator 1* were included to avoid usage of the micro-needle ground electrode. In addition, a thin cobalt/iron layer was deposited on the blades of *resonator 2* to perform static fracture tests with an external magnetic field. The asymmetric torsion bar of *resonator 2* used here was to increase the maximum operating stress without the notch structure. Furthermore, two bonding pads were utilized to monitor the variation of resistivity of aluminum interconnection on the torsion bar during the cyclic cryogenic fatigue tests. This device is currently being tested to verify the previous test results.
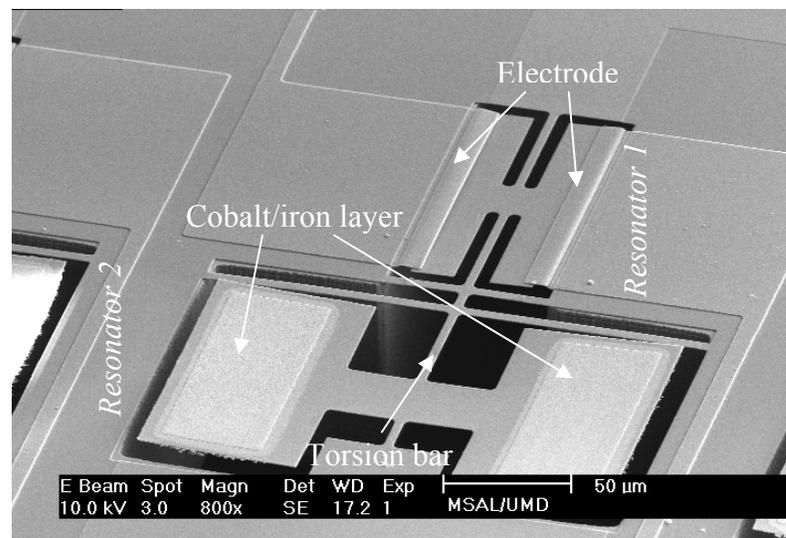
Figure 5.19: Micrograph of a mechanical-amplifier actuator fabricated with the micro-shutter arrays. This device includes two electrodes above *resonator 1,* a cobalt/iron thin layer on the blades of *resonator 2*, and an asymmetric torsion bar.

5.7 Summary

In this chapter, a novel test device, the so-called mechanical-amplifier actuator, is designed, fabricated, and tested to study fatigue properties of silicon nitride thin films at room temperature and at 30 K. In the device design, the mechanical-amplifier actuator has dimensions similar to the microshutter elements to emulate their torsional operating stress. A mechanical amplification based on a resonant technique is introduced to achieve high, controllable stress amplitude without high actuation voltages. The designed mechanical-amplifier actuator is fabricated using surface micromachining technique in combination with deep reactive ion etching (DRIE). All experiments are performed inside the FIB system with the cryogenic measurement setup and the micro-needle ground electrode.

From the experiment, the mechanical-amplifier actuators display fatigue failure when testing in a vacuum environment at both room temperature and cryogenic temperatures. However, the fatigue life for a given operating stress is found to decrease at cryogenic temperatures, which is attributed to a non-zero pre-stress, multi-axial cyclic loadings, and condensation of residual gas inside the FIB chamber. Based on the test results, the current microshutter array design will not suffer fatigue failure during its operation lifetime of 10^5 cycles at outer space.

CHAPTER 6

NANO-SCALE TENSILE TESTS USING MECHANICAL-AMPLIFIER ACTUATORS

Along with rapid development of microelectronics technologies into the submicron regime, nanoelectromechanical systems (NEMS) have attracted much interest due to their unique capabilities, such as: extremely high resonant frequencies, ultra-fine detection resolution, ultra-low power consumption, and extremely high mechanical compliance. Current reported applications include VHF (very high frequency) mechanical resonators [143], mechanical electrometers yielding sensitivity below a single electron charge [144], measurement of the quantum of thermal conductance [145], and nanorobots [146]. However, the extremely high surface-to-volume ratios and the unconventional operation conditions have become the critical issues to realize the full potential of NEMS applications since the fundamental material behaviors on a nano-scale will be determined by atomistic properties. Therefore, they may be completely different from the theories for bulk materials.

Understanding mechanical properties of materials on a nano-scale is important for the design of electronic devices and NEMS, as these devices may suffer thermal or mechanical stress during operation. Tests of MEMS materials (on a micro-scale) have been carried out for evaluating their mechanical properties since 1990 [147, 148], though the values for some materials are still not available. Conversely, characterization of mechanical properties on a nano-scale is challenging and the reported data are extremely

limited due to difficulties in making nano-scale test specimens and problems associated with measuring ultra-small physical phenomena during experiments.

This chapter presents a nano-scale tensile test with a modified mechanical-amplifier actuator to study the fatigue properties of LPCVD silicon nitride thin films [149]. In order to obtain tensile stress on the nano-scale test specimens, the mechanical-amplifier actuator is different from the one used previously for fatigue study of the microshutter array (Chapter 5). Here, the modified mechanical-amplifier actuator consists of two torsion bars (instead of one) and three suspended supporting beams to convert torsional stress into tensile stress. This device is fabricated using the same process flows discussed in Chapter 5, with an extra ion-milling step to obtain nano-scale test samples. All experiments were performed inside the focused-ion-beam (FIB) system with the micro-needle ground electrode (Chapter 5). At the end of this chapter, the test results of fatigue properties for nano-scale LPCVD silicon nitride thin films are reported.

6.1 Device design

In previous studies, nano-scale single-crystal silicon and silicon dioxide doubly-clamped beams, with the smallest dimension of 200 nm, were fabricated by field-enhanced anodization with an atomic force microscope (AFM) [150-153]. Bending tests for these beams were performed using the AFM with a diamond tip mounted on a stainless steel rectangular cantilever to obtain Young's modulus, fracture strength, and fatigue properties. This technique utilizes the high-resolution capability of an AFM in combination with a laser reflection setup to measurement the deflection of the bent stainless steel cantilever. However, preparation of the test specimens using this technique

is only suitable for single-crystal silicon and silicon dioxide, and the high facture strength of nano-scale thin films may introduce significant deformation on the diamond tip, which is not considered in their analytic model.

A novel electrostatic mechanical-amplifier actuator with dimensions similar to the microshutter array is proposed to study the fatigue properties of LPCVD silicon nitride thin films; the test results at room temperature (298 K) and at 30 K are discussed in Chapter 5. According to the same operation principle, this device can be used for nano-scale tensile tests with appropriate modifications. A schematic diagram of the modified mechanical-amplifier actuator is shown in Figure 6.1.
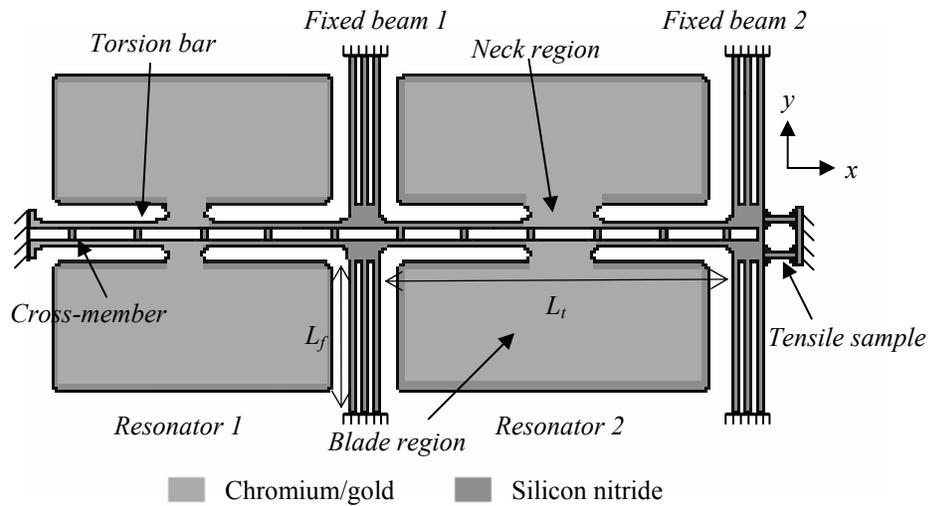
Figure 6.1: Schematic diagram of a mechanical-amplifier actuator for nano-scale tensile tests.

In this device design, two resonators are connected serially with two common torsion bars to solve the limitation of limited displacement amplitude with electrostatic actuation at limited applied voltages, as discussed in chapter 5. When operating, electrostatic energy is applied to *resonator 1* and this energy is transferred to *resonator 2* via the

common torsion bars. The vibration of *resonator 2* is then amplified by its quality factor when the frequency of pumped energy matches its resonant frequency. Based on this operation principle, the vibration amplification and amplitude of *resonator 2* can be controlled by the frequency and amplitude of the input electrostatic energy, respectively. In order to prevent non-torsional movement on the torsion bars without significant energy loss during operation, *fixed-beam 1* (three suspended beams) is utilized to increase lateral stiffness.

Compared with the mechanical-amplifier actuator used in Chapter 5, this device consists of two torsion bars and *fixed-beam 2* (three suspended beams) to achieve high axial stress on tensile samples. The design principles of the torsion bars and *fixed-beam 2* are discussed as follows. Consider a circular bar subjected to a pure torque *T* as shown in Figure 6.2. The bar twists and each section rotates about the longitudinal axis, which induces a shear stress at any point on the plane of the section. The magnitude of this stress is proportional to the distance from the center of the section, and its direction is perpendicular to the radius drawn through the point.
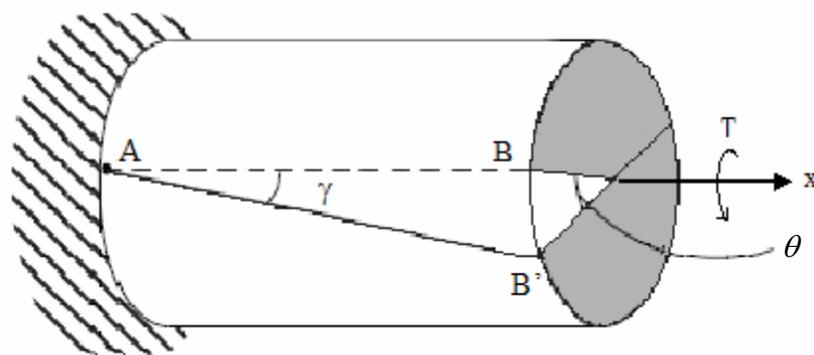
Figure 6.2: A circular bar with left end fixed subjected to a pure torque *T*. The free end twists through an angle *θ* with point B on the surface moving to B', which introduces a shear strain *γ*.

In addition to the shear stress, it has been proved that there is also longitudinal strain and stress and a solid circular cylinder tends to lengthen at the free end under twist [154]. For most applications of circular bars, neither longitudinal deformation nor stress is likely to be large enough to have engineering significance. However, in the case of a bar with a rectangular cross section, this longitudinal stress may become large (depending on the dimensions), and the stresses in the bar have components normal to the axis of rotation after twisting, which increases the torsional resistance and causes a "stiffening" effect. The maximum tensile stress σ_t and the total applied torque T for a twisted bar can be expressed as [124]

$$\sigma_t = \frac{E\tau_{max}}{12G^2}(\frac{a}{b})^2 \tag{6.1}$$

$$T = KG\frac{\theta}{L} + \frac{8}{45}E(\frac{\theta}{L})^3 ba^5 \tag{6.2}$$

where a is half the long edge of the rectangular section, b is half the short edge, E is the Young's modulus, G is the modulus of rigidity, and θ is the twist angle. In these equations, τ_{max} is the maximum shear stress as discussed in (5.1), while K is a factor representing the effective polar moment of inertia and shown in (5.3). The first term on the right side of (6.2) represents the applied torque T resisted by torsional shear stress and the second term represents the resistance by the tensile stress. It can be seen that the stiffening effect due to the tensile stress is negligible for small twist angle but increases rapidly as θ/L increases.

The torsion bar used in the mechanical-amplifier actuator has a rectangular cross section with a fixed thickness of 0.5 µm after fabrication. The width of the torsion bar can be designed to increase the maximum tensile stress σ_t with an appropriate twist angle

θ for a given torque T. From the equations (5.1), (5.3), and (6.1), the relationship between σ_t and a, and the relationship between K and a, can be plotted in Figure 6.3 and Figure 6.4, respectively. The maximum tensile stress σ_t of the torsion bar is found to increase with a larger dimension in width (i.e. a in (6.1)) for a given torque T. However, a larger width also increases rotational stiffness significantly due to the higher values of K and a on the right side of (6.2) and leads to a small twist angle θ, which is difficult to measure during experiments.

To increase the maximum tensile stress σ_t of the torsion bar and the twist angle θ simultaneously, a dual-bar configuration is utilized in the design of the mechanical-amplifier actuator as shown in Figure 6.1. Two torsion bars are connected parallel via small cross-members. The width and the length of each cross-member are 2 μm and 4 μm, respectively, with a separation distance of 17 μm. This configuration increases the effective value of a in (6.1), while reducing the effective rotational stiffness since there is less material between these torsion bars to be twisted.

The function of *fixed-beam 2* is to "convert" torsional stress into tensile stress to tensile samples as shown in Figure 6.1. The principle is to increase the rotational stiffness for twisted motion but lower the longitudinal stiffness (in x-direction) for tensile stress. The rotational stiffness of *fixed-beam 2* is complicated since the motion of *fixed-beam 2* is a combination of elongation/contraction (in y-direction) and bending movement during the twist of the torsion bars. Even so, the "efficiency" of *fixed-beam 2* can still be evaluated by assuming that most of the rotational stiffness is from the elongation/contraction of the fixed beams and expressed as
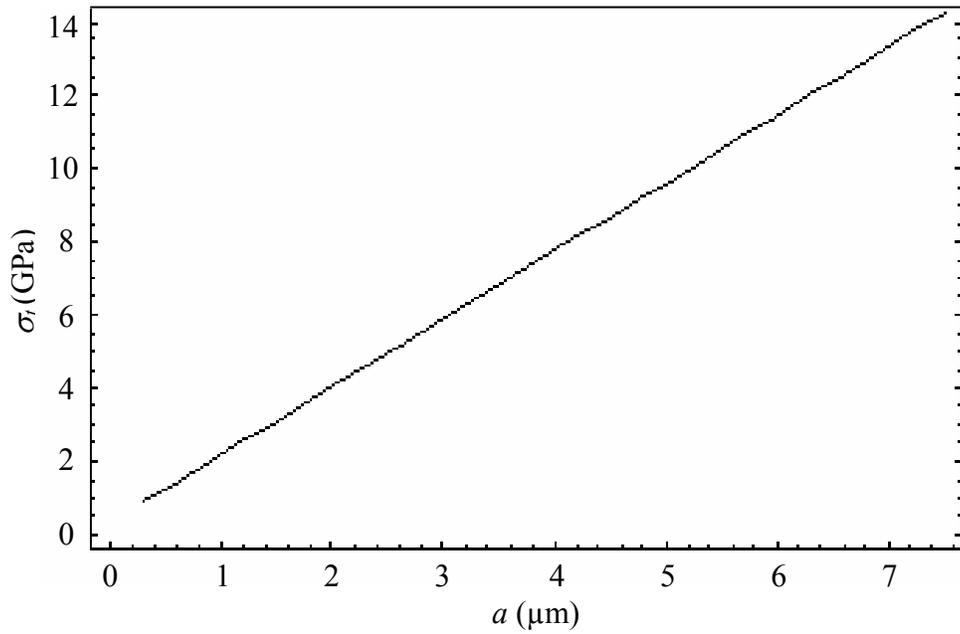
Figure 6.3: The relationship between σ_t and a from the equations (5.1) and (6.1). In this figure, the applied torque T is assumed to be 0.01 N·m and the value of b is equal to 0.25 μm.
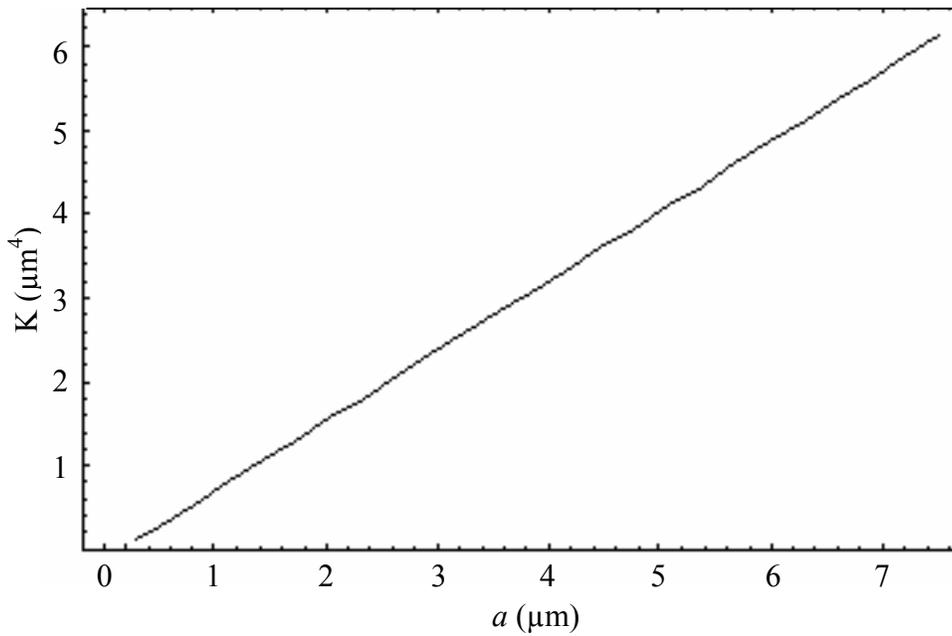
Figure 6.4: The relationship between K and a from the equation (5.3). Here, the value of b is equal to 0.25 μm.

$$\frac{K_{tensile}}{K_{rotational}} = \frac{W_f{}^2}{4L_f{}^2} \qquad (6.3)$$

where $K_{tensile}$ is the longitudinal stiffness, $K_{rotational}$ is the rotational stiffness, W_f is the width of *fixed-beam 2*, and L_f is the length of *fixed-beam 2*. The ratio of (6.3) can be found to be 9.8×10^{-5} with the dimensions of the mechanical-amplifier actuator presented in Table 6.1. Therefore, the torsional component can be filtered out with *fixed-beam 2*, and only tensile stress is expected to be applied to the tensile samples.

Table 6.1: Dimensions of mechanical-amplifier actuators for nano-scale tensile tests.

Torsion bar (μm)		Blade region (μm)		Neck region (μm)		Fixed-beam 1&2 (μm)		Tensile sample (μm)		Thickness (μm)
L_t	W_t	L_b	W_b	L_n	W_n	L_f	W_f	L_s	W_s	T
108	2	95	35	25	4	40.5	0.8	8	0.2	0.5

6.2 Device preparation

In section 5.3, the fabrication processes of the mechanical-amplifier actuator for the fatigue study of the microshutter array was discussed. In principle, the mechanical-amplifier actuator used for nano-scale tensile tests follows the same fabrication process, with an extra nanomachining step for tensile sample preparation.

The nanomachining of the tensile samples was carried out using the FIB system. In recent years, FIB instruments have become more prevalent for specimen preparation and inspection in microelectronics and MEMS fabrication. This is mainly because the FIB instruments permit microscopic inspection of the sample under consideration before, during, or after the ion-milling process via scanning ion microscopy (SIM) or scanning

electron microscopy (SEM). The direct write capability of FIB milling allows nano-scale fabrication without the requirement of an etch mask [155, 156].

The FEI 620 FIB system used in our experiment is a dual beam system with ion and electron columns as discussed in Chapter 2. This system uses a scanning 5-30 KV Gallium (Ga) ion beam for milling and imaging, with a current varying from 1 pA to 1150 pA and a spot size ranging from 8 nm to 500 nm. The tensile samples shown in Figure 6.1 are 1.6 µm in widths after microfabrication. A milling pattern with a desired width of 200 nm on the tensile samples was defined using a computer-generated machining template in the FIB software. The nanomachining was carried out at the ion-beam current of 11 pA with a nominal spot size of 15 nm. The milling depth was 0.5 µm. The mechanical-amplifier actuator after fabrication is shown in Figure 6.5, and close views of the tensile samples are shown in Figure 6.6 and Figure 6.7.
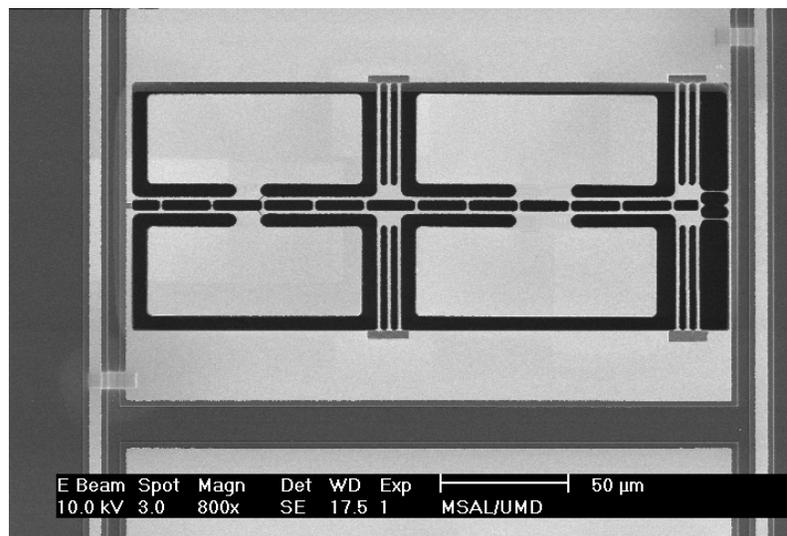
Figure 6.5: Micrograph of a mechanical-amplifier actuator for nano-scale tensile tests after fabrication.

E Beam	Spot	Magn	Det	WD	Exp		5 µm
10.0 kV	3.0	10000x	SE	17.4	1	MSAL/UMD	
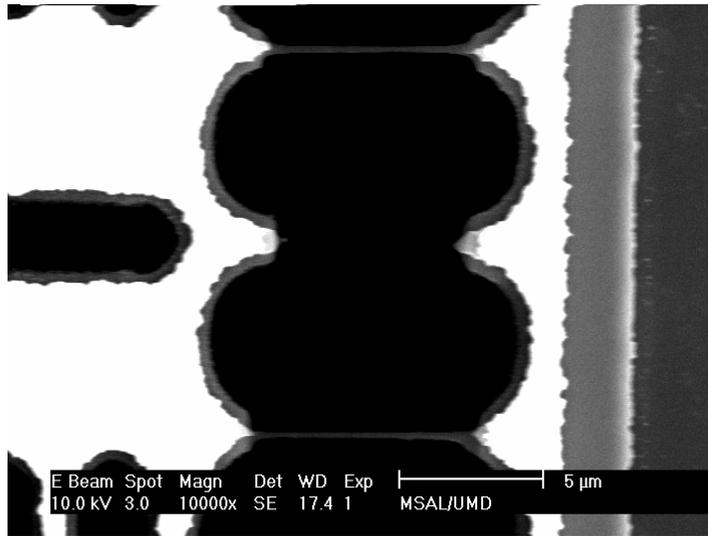
Figure 6.6: Close view of the tensile samples after ion milling. The milling current was 11 pA with a nominal spot size of 15 nm.

E Beam	Spot	Magn	Det	WD	Exp		2 µm
10.0 kV	3.0	25000x	SE	17.4	1	MSAL/UMD	
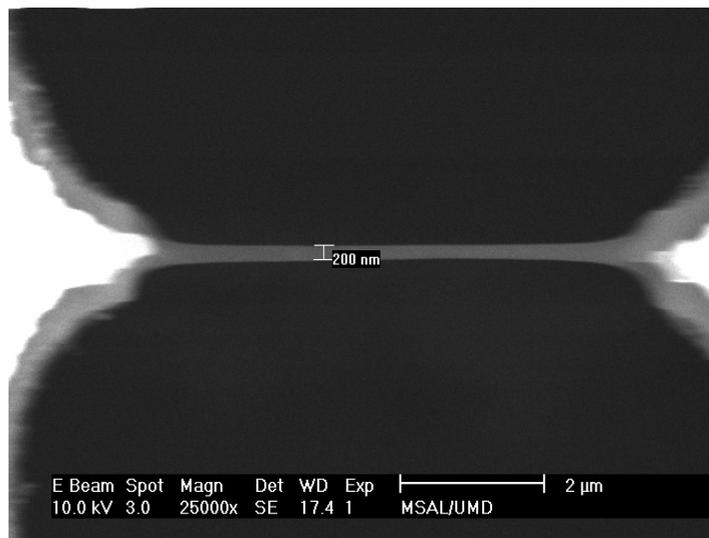
Figure 6.7: Close view of a tensile sample after ion milling. The milling current was 11 pA with a nominal spot size of 15 nm.

6.3 ANSYS finite-element-analysis model

The analytic model presented in section 6.1 is valid only for a single torsion bar under a pure torque. However, the configuration of the mechanical-amplifier actuator contains two torsion bars and *fixed-beam 2* to convert torsional stress into tensile stress. Therefore, an ANSYS finite-element-analysis (FEA) model is required to determine the stress amplitude of the tensile samples during experiments.

The ANSYS nonlinear models created for this work are shown in Figure 6.8 and Figure 6.9. The first model simulates the stress distribution of the device for a given blade displacement with only one suspended beam as *fixed-beam 2*, while the second model uses three suspended beams as *fixed-beam 2*. The elements and parameters utilized in these models are presented in Table 6.2. Here, the stress concentrations at the ends of the torsion bars and tensile samples were simulated with a radius of curvature $r = 2.5$ μm, which was measured using the SEM function provided by the FIB system. Figure 6.10 presents the maximum operating stress on the tensile samples for different blade displacements according to these ANSYS models. From this figure, the tensile samples can be considered as structures under only axial stress and less than 1% of stress on these samples is not tensile even at high stress amplitude. Additionally, the stress amplitude on the tensile samples increases if one suspended beam is used as *fixed-beam 2*.

Table 6.2: Elements and parameters of the mechanical-amplifier actuator utilized in ANSYS FEA model. The Young's modulus and the residual stress of the silicon nitride thin films are obtained from Chapter 3 and Chapter 4.

Element	Density (kg/m^3)	Young's Modulus (GPa)	Poisson's ratio	Residual stress (MPa)
Solid–92/Solid-187	3000 [32]	260.5	0.25	183.4
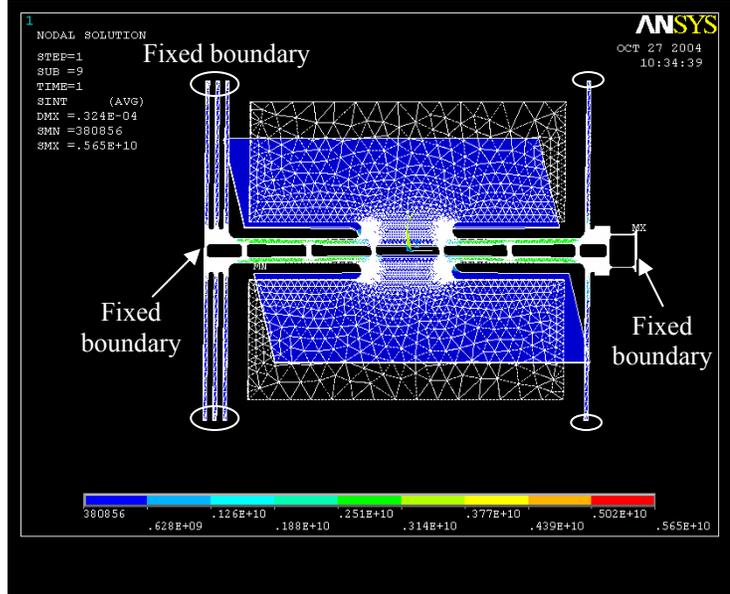
Figure 6.8: ANSYS FEA model used to calculate maximum stress on tensile samples with one suspended beam as *fixed-beam 2* for a given blade displacement. Circles in this figure represent a fixed boundary.
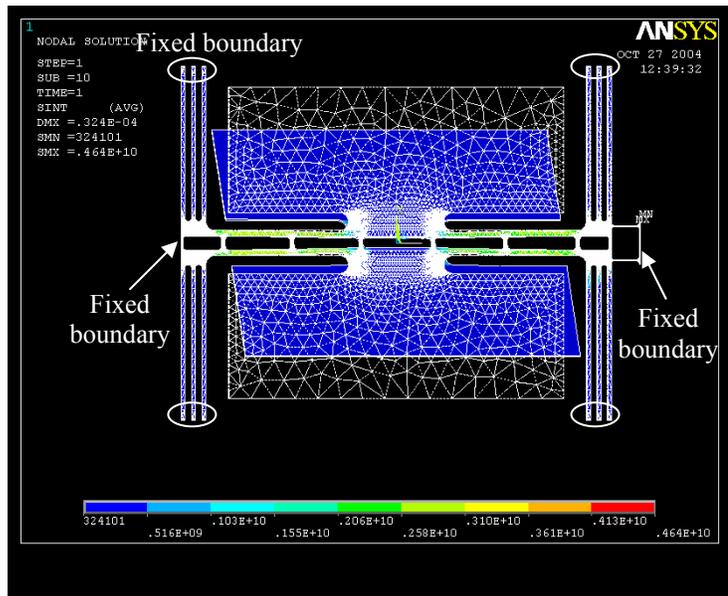
Figure 6.9: ANSYS FEA model used to calculate maximum stress on tensile samples with three suspended beams as *fixed-beam 2* for a given blade displacement. Circles in this figure represent a fixed boundary.
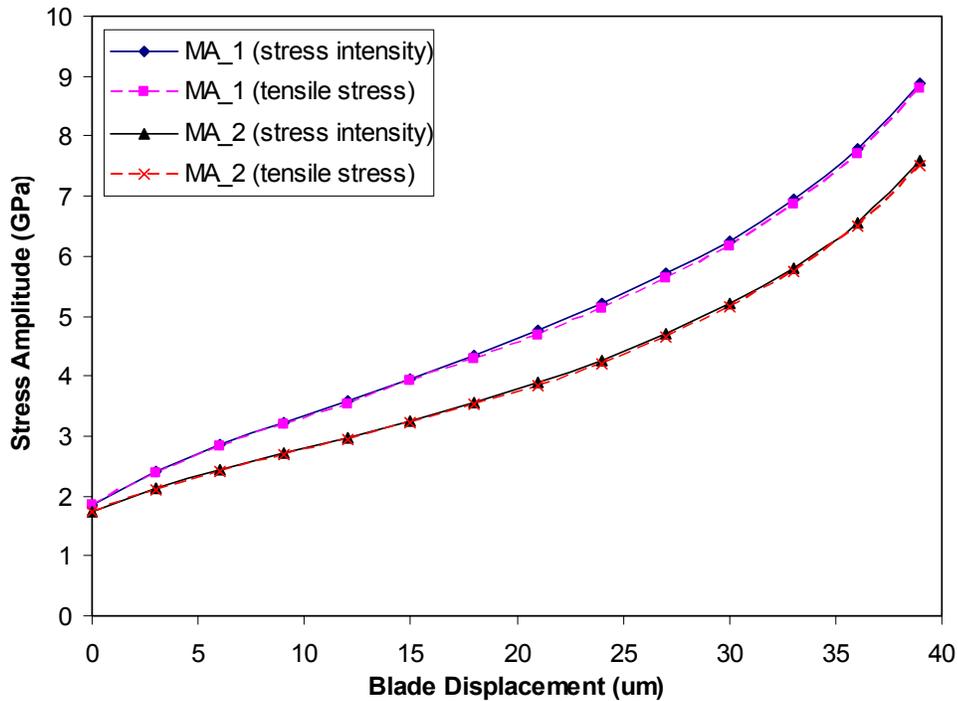
Figure 6.10: Maximum operating stress of the mechanical-amplifier actuator (MA) on the tensile samples with different blade displacements from ANSYS FEA models. MA_1 represents the MA with one suspended beam as *fixed-beam 2* and MA_2 is the MA with three suspended beams as *fixed-beam 2*. Stress intensity in the legend is the total stress applied to the tensile samples, while tensile stress includes only the longitudinal stress.

One important phenomenon shown in Figure 6.10 is that the tensile samples are under longitudinal stress even without any blade displacement. This behavior can be explained by the balance of residual stress/force on asymmetric structures after release. A simplified analytic model can be established for further understanding. Figure 6.11 illustrates an asymmetric structure with a wider strip connected with two narrow necks. Once the structure is released from a substrate, the forces due to residual tensile stress are not equal at the interface of these two widths and the wide suspended strip (width W_1) will pull on the thinner necks (total width W_2), resulting in a deflection δ to the left. The

tensile stress σ_t on the neck regions can be calculated based on the balance of the forces

after the deflection δ on the structures and expressed as

$$\sigma_t = \frac{(W_1 - W_2)}{(\frac{W_1}{L_1} + \frac{W_2}{L_2})}(\frac{\sigma}{L_2}) \qquad (6.4)$$

where W_1 and L_1 are the width and length of the wide strip, W_2 and L_2 are the width and

length of the narrow neck, and σ is the residual tensile stress. One assumption in this

model is that it neglects the influence of the Poisson's ratio on the wide strip, which may

not be valid for the structure with dimensions similar in width and length.
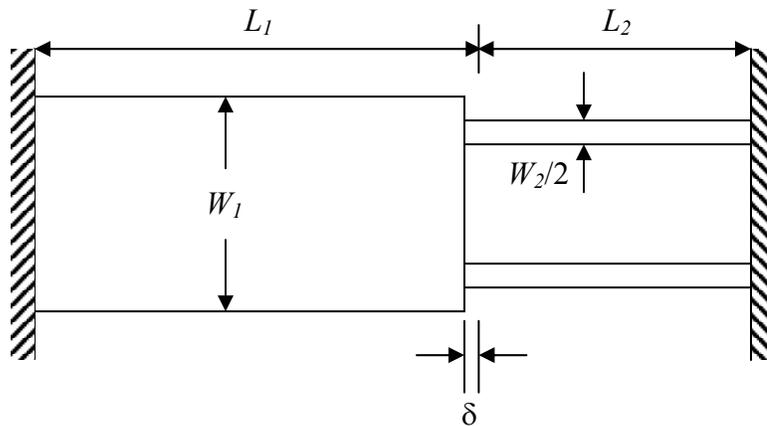
Figure 6.11: Asymmetric structure with a wider strip on the left side and two narrow necks on the right side.

6.4 Experimental results

Before testing the mechanical-amplifier actuator, ion milling was performed to

remove two suspended beams and keeping only one as *fixed-beam 2* (Figure 6.12) since

this configuration can increase stress amplitude on the tensile samples. The mechanical-

amplifier actuator used in this chapter follows the same testing procedures; the detailed
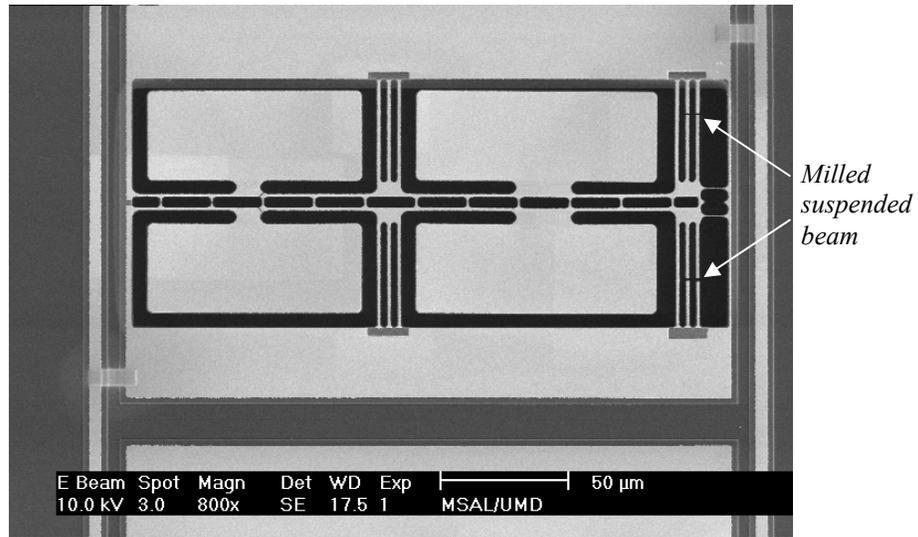
Figure 6.12: Micrograph of a mechanical-amplifier actuator for nano-scale tensile tests with one suspended beam as *fixed-beam 2*.

experimental techniques can be found in Chapter 5. Figure 6.13 shows a mechanical-amplifier actuator with *resonator 2* at its first resonant mode. In this experiment, the input voltages to *resonator 1* were 14.1 V_{rms} and the resonant frequency of *resonator 2* was found to be 38.09 KHz. The experimental results from the stress-life testing are shown in Figure 6.14. When the maximum operating stress exceeded 4.3 GPa, the mechanical-amplifier actuators exhibited time-delayed failure. On the other hand, tensile samples with testing stress amplitude below 3.8 GPa survived cyclic loadings up to 10^8 cycles. An example of broken tensile samples after cyclic loadings is shown in Figure 6.15. A crack initiated at the center of the upper *tensile sample* in this figure. Once the upper *tensile sample* was broken, all axial stress was applied to the lower *tensile sample* and broke it immediately. The curl-down broken *tensile sample* is due to release of residual stress, causing a non-zero axial stress before testing as discussed in the last section.
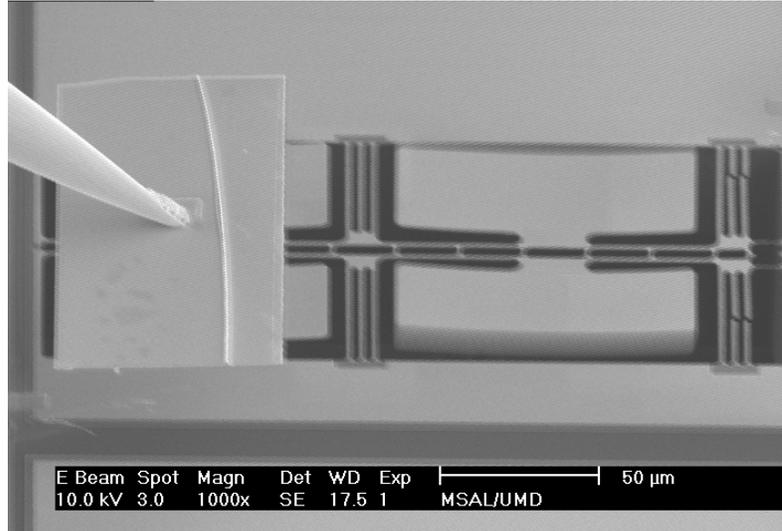
Figure 6.13: Micrograph of a mechanical-amplifier actuator for nano-scale tensile tests with *resonator 2* at its first resonant mode.
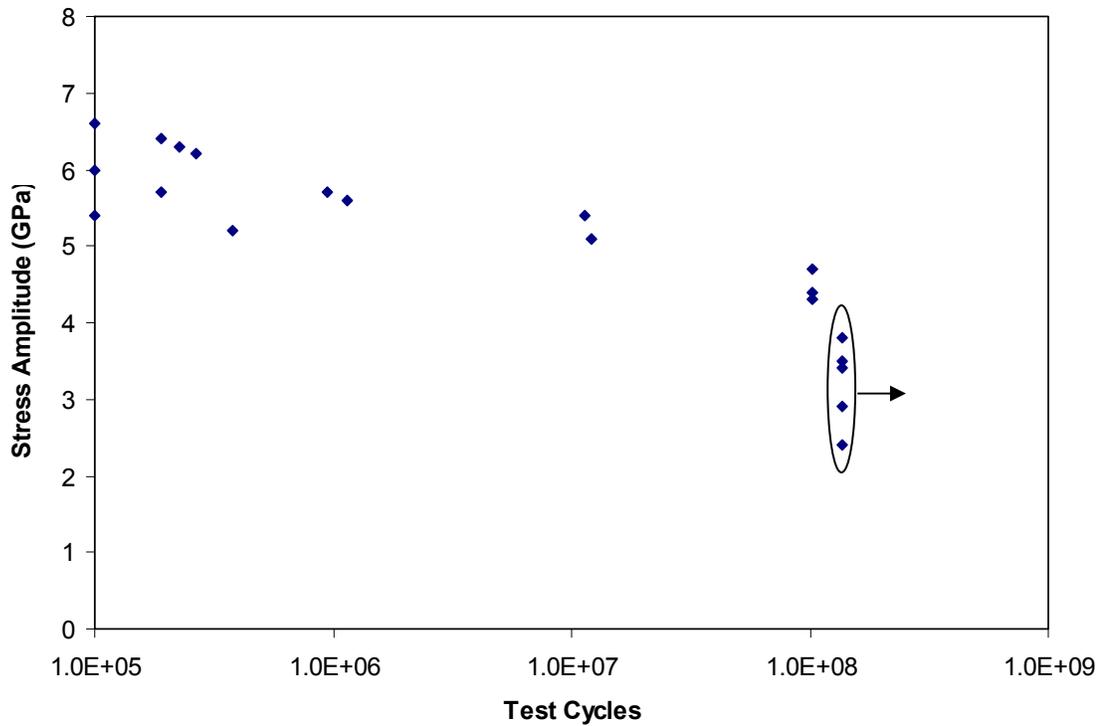
Figure 6.14: Stress-life testing data for nano-scale tensile samples. The circle with a horizontal arrow indicates devices that did not fail under cyclic loading up to 10^8 cycles.
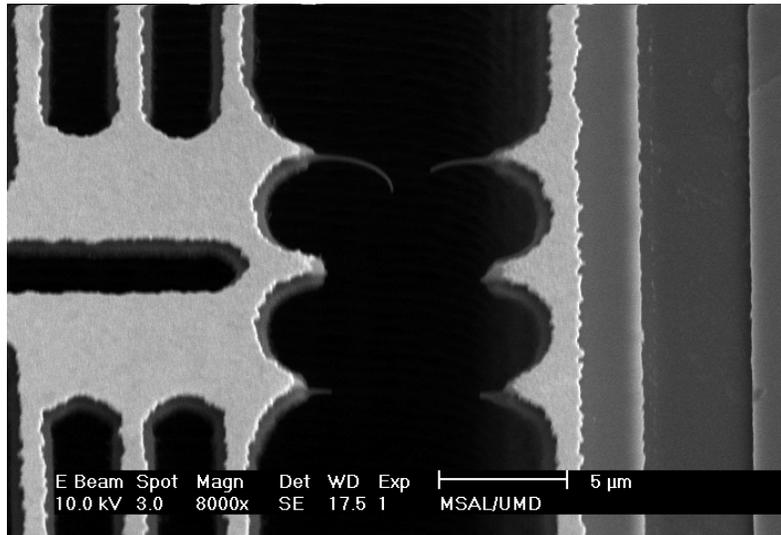
Figure 6.15: Micrograph of tensile samples after cyclic loading.

The resonant frequency of the mechanical-amplifier actuator was used to monitor the stiffness of the tensile samples during cyclic loadings, and was observed to decrease monotonically with test time as shown in Figure 6.16. The change in resonant frequency indicates that the tensile samples become more compliant during the test. This behavior strongly suggests that the failure of the tensile samples occurs as a result of the progressive accumulation of damage. In addition, a significant decrease of the resonant frequency was found at the time of failure due to decrease of the effective spring constant of *resonator 2*.
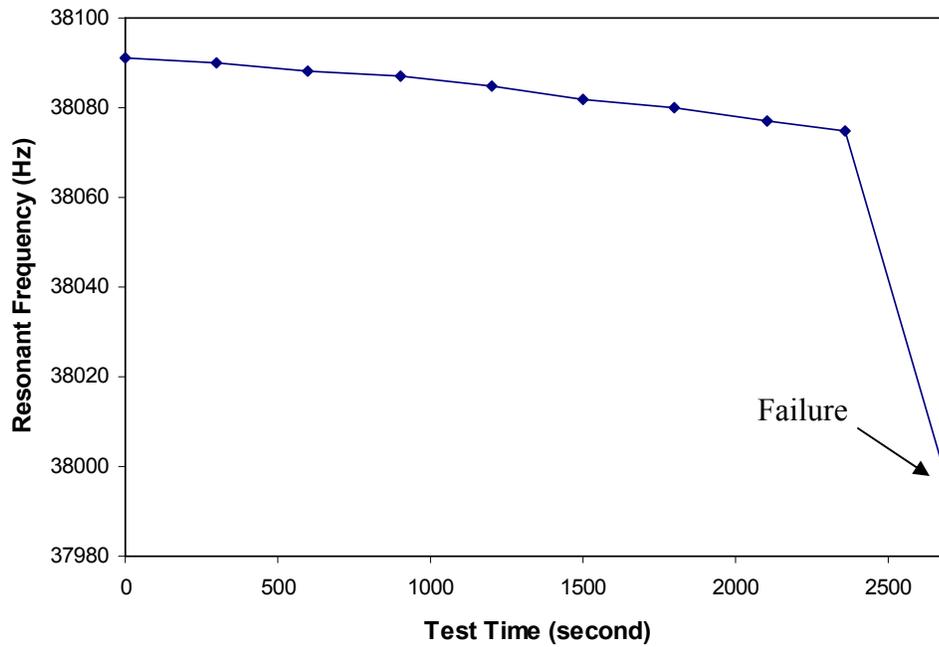
Figure 6.16: Variation of resonant frequency with time for a mechanical-amplifier actuator during fatigue testing (Test cycle: 10^8 cycles at stress amplitude 4.4 GPa).

6.5 Discussion

The mechanical-amplifier actuators used in this chapter were tested in the same condition (Pressure: 10^{-6} Torr, Temperature: 23 ± 1 °C) as the ones utilized in Chapter 5. Comparing both test results, the nano-scale tensile samples displayed lower fatigue resistance. However, it is difficult to conclude any size effect on the fatigue property at this point since the difference of pre-stress status, loading mechanisms, and surface conditions between these two devices can have a significant effect on the test results.

The residual tensile stress of the silicon nitride thin films induced a 1.85 GPa tensile stress on the nano-scale tensile samples before any blade displacement. The existing pre-stress enhances the average stress amplitude and the tensile samples did not return to zero-stress state during experiments. Two analytic models proposed by Gerber and

Goodman [78, 124] point out that the fatigue strength can be reduced significantly due to a nonzero mean stress. In addition, different loading (torsional versus axial) mechanisms may also change the fatigue life of the test structures. The surface condition of test structures is another critical factor that has been demonstrated to induce premature failure [138]. Different device preparation methods will change the surface roughness, which can locally increase the stress amplitude. This situation becomes severe on a nano-meter scale since the test structure in this region has higher surface-to-volume ratio. As the nano-scale tensile samples in this study were fabricated using ion milling instead of microfabrication, damages and gallium implantation on the surfaces and the sidewalls of the tensile samples are inevitable. Therefore, the fatigue life testing results in this chapter may not represent the natural behavior of nano-scale silicon nitride thin films. Further study on the size effect can be performed using the modified mechanical-amplifier actuators prepared by micro-/nano-fabrication with tensile samples ranging from micro-meter scales to nano-meter scales to eliminate these factors.

6.6 Summary

The chapter presents the design, fabrication, and testing of a modified mechanical-amplifier actuator for fatigue study of LPCVD silicon nitride thin films on a nano-meter scale. The design principle is to utilize a longitudinal stress produced from two rotated torsion bars. The dual-bar configuration used here can increase the longitudinal stress while reducing the rotation stiffness at the same time. To obtain tensile stress on the tensile samples, one suspended beam (*fixed-beam 2*) is connected between the torsion

bars and the tensile samples. The high rotational spring constant of this beam can then be used to eliminate the torsional stress. Therefore, only tensile stress is applied to the tensile samples, and the amplitude of this stress can be controlled by the frequency and the amplitude of the input electrostatic energy.

The modified mechanical-amplifier device is tested inside the FIB system and a time-delayed failure is observed on the tensile samples with stress amplitude over 4.3 GPa. Comparing the experimental results on the nano-meter and micro-meter scales, the lower fatigue resistance of the nano-scale tensile samples is attributed to a higher pre-stress and FIB-induced damage on the test structures.

The advance of MEMS and NEMS technologies has given impetus for researchers to develop new devices and systems for different applications. Unfortunately, the earlier success of these technologies has led the designers to a misconception that the most important failure mode for design is based on the fracture behavior of structural materials. Due to this effect, all kinds of reliability problems have been recognized during the operation of these devices, and become an important factor that hinders the commercialization of MEMS/NEMS products. Design for reliability, actually, is a critical concern that needs to be considered at the early stage of MEMS/NEMS designs. From the studies of Chapter 5 and Chapter 6, operating environment, device preparation methods, pre-stress status, and loading conditions are found to have considerable influence on the time-dependence degradation of structural materials. Clearly, the availability of stress-life fatigue data and an understanding of fatigue mechanisms at different testing conditions remain important to improving the performance of these

devices and to evaluating their long-term durability. More research work for different

MEMS/NEMS materials is expected to be done to address this problem.

CHAPTER 7

CONCLUSIONS

7.1 Summary of current research

This thesis presents new test devices (T-shaped cantilevers, microgauge sensors, and mechanical-amplifier actuators) to characterize mechanical properties and reliability of silicon nitride thin film materials at room and cryogenic temperatures using FIB-based measurement techniques for the first time. This research includes design, modeling, fabrication, and (electrostatic, mechanical, and thermal) testing of these devices. Furthermore, a helium-cooled cryogenic measurement setup installed inside a FIB system is developed to provide cryogenic temperatures down to 20 K. As the uncertainty of mechanical properties and reliability of MEMS-based thin film materials is still a critical factor that hinders the commercialization of MEMS products, the research results of this thesis are crucial not only for the development of MEMS devices in space applications but also for other MEMS devices operating in both room-temperature and low-temperature environments.

This thesis research can be summarized and significant contributions of each chapter are described accordingly. A comprehensive review of MEMS technologies is presented in Chapter 1 with emphasis on the development of microshutter arrays, reliability and failure mechanisms in MEMS devices, as well as the current techniques for mechanical property characterization. Based upon information available in the literature, this thesis

provides a new methodology for understanding mechanical behaviors of MEMS devices at cryogenic temperatures where the objectives of this research are stated.

A cryogenic measurement setup installed inside a FIB system, which can provide cryogenic temperatures down to 20 K, is discussed in Chapter 2. To obtain accurate temperature measurement, a thin-film thermal resistor with a sensitivity of 7.85 Ω/K is fabricated with the test devices as an integrated temperature sensor, and an equivalent thermal model is established according to the temperature measurement and thermal capacity of each component utilized in this setup. Combined with the unique capabilities of the FIB system, a micro-repair technique for the microshutter arrays and stress analysis of multilayer structures are also demonstrated.

In Chapter 3, a new test device, T-shaped cantilever beam, is introduced for Young's modulus, Poisson's ratio, and fracture strength measurement at room temperature and at 30 K. Resonant frequencies of the T-shaped cantilever with different "milling masses" are measured to obtain the Young's modulus and the beam thickness simultaneously. The "milling-mass" approach used here improves the accuracy for measuring the thin-film thickness, which is a critical parameter for such a resonant technique. The fracture behavior of silicon nitride thin films is characterized using a bending test combined with a finite-element-analysis model.

Chapter 4 presents a passive microgauge sensor to characterize residual stress and coefficients of thermal expansion (CTE) for silicon nitride thin films. Based on the mechanism of displacement amplification, this sensor can enhance the capability for measuring tiny residual/thermal strains. Both the average value and a local knowledge of the residual stress and CTE can be obtained using the microgauge sensor. Furthermore,

141

the measurement result is independent of thin-film thickness and process variations, which are key limiting factors for other measurement methods and techniques reported previously.

Chapter 5 presents a novel electrostatic actuator, the so-called mechanical-amplifier actuator, with dimensions similar to the microshutter element to understand the fatigue property of the microshutter array. This device is operated based on the mechanism of vibration amplification to avoid high actuation voltages. The stress level on the test device can be easily controlled by the frequency and amplitude of the input voltages. Furthermore, unlike the slow magnetic actuation of the microshutter arrays, an accelerated fatigue test can be performed due to the relatively high resonant frequency of the mechanical-amplifier actuator.

In Chapter 6, the mechanical-amplifier actuator is modified to perform direct tensile tests on nano-scale silicon nitride test structures. The design principle is to utilize a longitudinal stress produced from two rotated torsion bars. The dual-bar configuration used here is to increase the longitudinal stress while reducing the rotation stiffness at the same time. In addition, one suspended beam (*fixed-beam 2*) is connected between the torsion bars and the tensile samples, which can eliminate the torsional stress on the tensile samples.

The microshutter array, a programmable aperture mask on NASA's James Webb Space Telescope, will be the first MEMS device operating in outer space, and require reliable cryogenic operation at 30 K over a 10 year mission lifetime without repair after launch. Therefore, the challenges facing the development of the microshutter array are to understand the mechanical behaviors and the possible failure mechanisms at this reduced

temperature. This thesis investigates the mechanical properties and reliability of low-stress LPCVD silicon nitride thin films, the structural materials of the microshutter arrays, at cryogenic temperatures. The research results provide important parameters for the design, fabrication, and characterization of the microshutter array. The presented device design and experimental techniques in this thesis are suitable for measurement in a large range of temperatures (from room to 20 K) and can be easily extended to characterize a series of MEMS-based thin film materials.

7.2 Future work

The current study focuses on the development of new test devices and experimental techniques for mechanical property and reliability characterization. Further investigations on fundamental material properties, such as defect distributions in thin films, are required to understand their influence on the measurement results. Moreover, statistical modeling providing a prediction of probability on mechanical properties needs to be developed. In Chapter 6, we present a test device (modified mechanical-amplifier actuator) to perform direct tensile tests on nano-scale silicon nitride test structures at room temperature. This device can also be used to study the fatigue properties of nano-scale silicon nitride thin films at cryogenic temperatures. For the testing of the mechanical-amplifier actuator, the usage of the micro-needle ground electrode limits its applications to other researchers. A new test device with an integrated ground electrode was designed and fabricated as shown in Figure 5.19. Further research effort can made to include a sensing mechanism in this device to measure the displacement of *resonator 2*.

Based on this research, fracture and fatigue failures of the torsion bar on the microshutter array are not expected to occur during its mission lifetime. From the magnetic actuation testing of the microshutter array conducted at NASA Goddard Space Flight Center, the dominant failure mode was found to be the missing of the shutter blades from the neck regions, where the maximum stress is not anticipated for the designed actuation movement (pure rotation of the shutter blades). Figure 7.1 is a micrograph showing the microshutter elements before actuation. This failure has been recognized as a result of in-plane twisted motion of the shutter blades during the magnetic actuation. Further analysis of the direction of magnetic field on the cobalt/iron thin films is required to eliminate unwanted non-torsional movement. Stiction between the shutter blades and the side-wall vertical electrodes was another observed failure mechanism, which leads to the shutter elements in a permanent-open status. Dielectric charging of the silicon nitride thin films and residual magnetic field on the cobalt/iron materials may be the causes of such "failed closed" cases. Process-related failures and packaging-related failures definitely still need to be carefully monitored through the whole process. Extensive testing and failure analysis will be performed before the final deployment of the microshutter array to outer space.

For the mechanical property and reliability characterization of thin film materials, several testing apparatuses and techniques have been proposed. However, there are no standard testing methods that can provide accurate and easy measurements yet. In addition, the influence of fabrication processes, size effect, and stress/loading conditions to the mechanical properties of test structures is not clear. Current solution to address these uncertainties is to conduct the measurement on test devices with similar fabrication

processes, element sizes, and stress conditions to the proposed MEMS devices. As a result, the measurement data is only valid for the development of a specific device and is difficult to be applied for other designs in most cases. To understand the influence of these factors, more experimental works need to be done with careful design of test devices to eliminate other unknown properties. Standard testing methods, which may integrate MEMS sensors and actuators with test devices to form a complete system, must be developed. Through standardized testing procedures, measured data can be shared and advances in MEMS applications will thereby be accelerated.
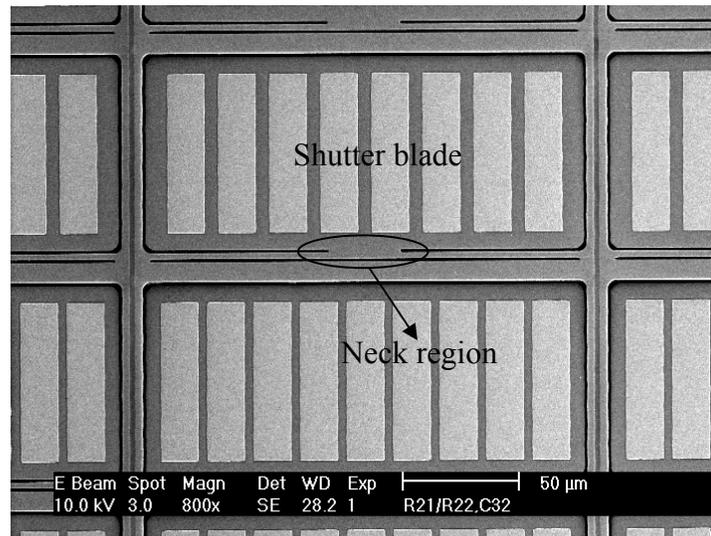
Figure 7.1: Micrograph of microshutter elements. From the magnetic actuation testing results of this device, the dominant failure mode is the missing shutter blades from the neck regions.

BIBLIOGRAPHY

[1]   B. P. Gogoi and D. Mladenovic, "Integration technology for MEMS automotive sensors," presented at IEEE 28th Annual Conference of the Industrial Electronics Society, 2002.

[2]   H. Kim and K. Chun, "Integrated MEMS for pressure transponder," presented at Transducer'97, Chicago, IL, 1997.

[3]   T.-W. Yeow, K. L. E. Law, and A. Goldenberg, "MEMS optical switches," *IEEE Communications Magazine*, vol. 39, pp. 158 - 163, 2001.

[4]   J. Gong, S.-K. Fan, and C.-J. Kim, "Portable digital microfluidies platform with active but disposable lab-on-chip," presented at 17th IEEE International Conference on Micro Electro Mechanical Systems, 2004.

[5]   T. K. Tang, "MEMS for space applications," presented at IEEE International SOI Conference, Rohnert Park, CA, 1999.

[6]   S. J. Fiedziuszko, "Applications of MEMS in communication satellites," presented at 13th International Conference on Microwaves, Radar and Wireless Communications, Wroclaw, Poland, 2000.

[7]   D. Farrar, W. Schneider, R. Osiander, J. L. Champion, A. G. Darrin, D. Douglas, and T. D. Swanson, "Controlling Variable Emittance (MEMS) Coatings for space applications," presented at The Eighth Intersociety Conference on Thermal and Thermomechanical Phenomena in Electronic Systems, 2002.

[8]   H. S. Stockman, *The next generation space telescope: visiting a time when galaxies were young*: The Association of Universities for Research in Astronomy, Inc., 1997.

[9]   H. S. Moseley, R. K. Fettig, A. Kutyrev, C. Bowers, R. Kimble, J. Orloff, and B. Woodgate, "Programmable 2 dimensional microshutter arrays," *Proceedings of SPIE*, vol. 3878, pp. 392 - 397, 1999.

[10]   H. S. Moseley, R. K. Fettig, A. Kutyrev, M. Li, D. Mott, and B. Woodgate, "Status of the development of a 128X128 microshutter array," *Proceedings of SPIE*, vol. 4178, pp. 51 - 58, 2000.

[11]   T. King, G. Kletetschka, M. A. Jah, M. Li, M. D. Jhabvala, L. L. Wang, M. A. Beamesderfer, A. Kutyrev, R. F. Silverberg, D. S. Schwinger, G. M. Voellmer, H. S. Moseley, and L. M. Sparr, "Cryogenic characterization and testing of magnetically-actuated microshutter arrays for the James Webb Space Telescope,"

presented at Solid-State Sensor, Actuator and Microsystems, Hilton Head Island, SC, 2004.

[12]   D. Mott, S. Aslam, K. A. Blumenstock, R. K. Fettig, D. Franz, A. Kutyrev, M. Li, C. J. Monroy, H. S. Moseley, and D. S. Schwinger, "Magnetically actuated microshutter arrays," *Proceedings of SPIE*, vol. 4561, pp. 163 - 170, 2001.

[13]   M. Li, S. Aslam, A. Ewin, R. K. Fettig, D. Franz, C. Kotechi, A. Kutyrev, H. S. Moseley, C. J. Monroy, D. Mott, and Y. Zheng, "Fabrication of microshutter arrays for space application," *Proceedings of SPIE*, vol. 4407, pp. 295 - 303, 2001.

[14]   G. T. A. Kovacs, N. I. Maluf, and K. E. Petersen, "Bulk micromachining of silicon," *Proceedings of the IEEE*, vol. 86, pp. 1536 - 1551, 1998.

[15]   J. M. Bustillo, R. T. Howe, and R. S. Muller, "Surface micromachining for microelectromechanical systems," *Proceedings of the IEEE*, vol. 86, pp. 1552 - 1574, 1998.

[16]   Y. Gianchandani and K. Najafi, "A bulk silicon dissolved wafer process for microelectromechanical systems," *Techinical Digest of Electron Devices Meeting*, pp. 757 - 760, 1991.

[17]   W. Ehrfeld, M. Abraham, U. Ehrfeld, M. Lacher, and H. Lehr, "Materials for LIGA products," presented at MEMS '94, Oiso, Japan, 1994.

[18]   W. Meeusen, J. Clijnen, D. Reynaerts, H. Van Brussel, and R. Puers, "Micro-electro-discharge machining as microsensor fabrication technology," *IEEE Sensors Journal*, vol. 3, pp. 632 - 639, 2003.

[19]   H. Seidel, L. Csepregi, A. Heuberger, and H. Baumgartel, "Anisotropic etching of crystalline silicon in alkaline solutions I: Orientation dependence and behavior of passivation layers," *Journal of The Electrochemical Society*, vol. 137, pp. 3612 - 3636, 1990.

[20]   H. Seidel, L. Csepregi, A. Heuberger, and H. Baumgartel, "Anisotropic etching of crystalline silicon in alkaline solutions II: Influence of dopants," *Journal of The Electrochemical Society*, vol. 137, pp. 3626 - 3632, 1990.

[21]   R. T. Howe, "Recent advances in surface micromachining," presented at 13th Sensor Symposium, Tokyo, Japan, 1995.

[22]   R. T. Howe and R. S. Muller, "Stress in polyrystalline and amporphous silicon thin films," *Journal of Applied Physics*, vol. 54, pp. 4674 - 4675, 1983.

[23]   H. Baltes, "CMOS as sensor technology," *Sensors and Actuators A: Physical*, vol. 37 -38, pp. 51 - 56, 1993.

[24]   L. J. Hornbeck, "From cathode rays to digital micromirrors: A history of electronic projection display technology," *TI Techical Journal*, pp. 7 - 46, 1998.

[25]   C. Lemaire, "Surface micromachined sensors for vehicle and personal navigation systems," presented at IEEE Conference on Intelligent Transportation System, Boston, MA, 1997.

[26]   B. E. Cole, R. E. Higashi, and R. A. Wood, "Monolithic two-dimensional arrays of micromachined microstructures for infrared applications," *Proceedings of the IEEE*, vol. 86, pp. 1679 - 1686, 1998.

[27]   C. E. Bauer, "Business perspectives on MCM, MEMS and MEOMS," presented at Electronic Materials and Packaging, Jeju Island, South Korea, 2001.

[28]   A. R. Mirza, "Wafer-level packaging technology for MEMS," presented at Thermal and Thermomechanical Phenomena in Electronic Systems, Las Vegas, NV, 2000.

[29]   K. Minami, T. Moriuchi, and M. Esashi, "Cavity pressure control for critical damping of packaged micromechanical devices," presented at Solid State Sensors and Actuators, Stockholm, Sweden, 1995.

[30]   M. Previti and K. Gilleo, "Getters: micromolecular scavengers for packaging MEMS," presented at International Symposium on Advanced Packaging Materials: Processes, Properties and Interfaces, Braselton, GA, 2001.

[31]   G. M. Voellmer and J. Palmer, "Packaging MEMS devices for cryogenic space applications: JWST microshutters," presented at MEMS Alliance, University of Maryland, College Park, 2003.

[32]   S. D. Senturia, *Microsystem design*. Norwell, MA: Kluwer, 2001.

[33]   V. Samper and A. Trigg, "MEMS failure analysis and reliability," presented at International Symposium on the Physical and Failure Analysis of Integrated Circuits, Singapore, 2003.

[34]   D. M. Tanner, "Reliability of surface micromachined MicroElectroMechanical actuators," presented at International Conference on Microelectronics, Albuquerque, NM, 2000.

[35]   D.-H. Shim and J.-W. Cho, "Nonlinear micromachined flexure for stiction reduction," presented at International Conference on Modeling and Simulation of Microsystems, San Juan, Puerto Rico, 2002.

[36]   X. Zhu, "Monolayer surface coatings solve stiction and drift problems in MEMS," presented at International Conference on MEMS, NANO and Smart Systems, Minneapolis, MN, 2003.

[37]   C.-P. Chang, "MEMS for telecommunications: devices and reliability," presented at IEEE 2003 Conference on Custom Integrated Circuits, Murray Hill, NJ, 2003.

[38]   W. N. Sharpe, Jr. , K. M. Jackson, K. J. Hemker, and Z. Xie, "Effect of specimen size on Young's modulus and fracture strength of polysilicon," *Journal of Microelectromechanical Systems*, vol. 10, pp. 317 - 326, 2001.

[39]   S. Johansson, J.-A. Schweitz, L. Tenerz, and J. Tiren, "Fracture testing of silicon microelements in situ in a scanning electron microscope," *Journal of Applied Physics*, vol. 63, pp. 4799 - 4803, 1988.

[40]   Y. C. Tai and R. S. Muller, "Measurement of Young's modulus on microfabricated structures using a surface profiler," presented at IEEE Conference on Micro Electro Mechanical Systems, Napa Valley, CA, 1990.

[41]   X. Li and B. Bhushan, "Micro/nanomechanical characterization of ceramic films for microdevices," *Thin Solid Films*, vol. 340, pp. 210 - 217, 1999.

[42]   M. Gad-el-Hak, *The MEMS handbook*: CRC Press, 2002.

[43]   P. M. Osterberg and S. D. Senturia, "M-TEST: A test chip for MEMS material property measurement using electrostatically actuated test structures," *Journal of Microelectromechanical Systems*, vol. 6, pp. 107 - 118, 1997.

[44]   I. Chasiotis and W. Knauss, "Mechanical properties of thin polysilicon films by means of probe microscopy," *Proceedings of SPIE*, vol. 3512, pp. 66 - 75, 1998.

[45]   W. N. Sharpe, Jr. , B. Yuan, and R. L. Edwards, "A new technique for measuring the mechanical properties of thin films," *Journal of Microelectromechanical Systems*, vol. 6, pp. 193 - 199, 1997.

[46]   D. T. Read and J. W. Dally, "A new method for measuring the constitutive properties of thin films," *Journal of Materials Research*, vol. 8, pp. 1542 - 1549, 1992.

[47]   T. Tsuchiya, O. Tabata, J. Sakata, and Y. Taga, "Specimen size effect on tensile strength of surface micromachined polycrystalline silicon thin films," presented at IEEE Conference on Micro Electro Mechanical Systems, Nagoya, Japan, 1997.

[48]   J. J. Vlassak and W. D. Nix, "A new bulge test technique for the determination of Young's modulus and Poisson's ratio of thin films," *Journal of Materials Research*, vol. 7, pp. 3242 - 3249, 1992.

[49]   S. Jayaraman, R. L. Edwards, and K. Hemker, "Determination of the mechanical properties of polysilicon thin films using bulge testing," *Materials Research Society Symposium*, vol. 505, pp. 623 - 628, 1998.

[50]   K. E. Petersen and C. R. Guarnieri, "Young's modulus measurements of thin films using micromechanics," *Journal of Applied Physics*, vol. 50, pp. 6761 - 6766, 1979.

[51]   C. L. Muhlstein, E. A. Stach, and R. O. Ritchie, "Mechanism of fatigue in micron-scale films of polycrystalline silicon for microelectromechanical systems," *Applied Physics Letters*, vol. 80, pp. 1532 - 1534, 2002.

[52]   W.-H. Chuang, T. Luger, R. K. Fettig, and R. Ghodssi, "A cryogenic measurement setup for microelectromechanical systems used in space applications," *Review of Scientific Instruments*, April, 2005 (in press).

[53]   W.-H. Chuang, T. Luger, R. K. Fettig, and R. Ghodssi, "Measurement of mechanical properties of silicon nitride thin film at cryogenic temperatures," presented at American Vacuum Society 50th International Symposium, Baltimore, Maryland, 2003.

[54]   S. Reyntjens and R. Puers, "A review of focused ion beam applications in microsystem technology," *Journal of Micromechanics and Microengineering*, vol. 11, pp. 287 - 300, 2001.

[55]   J. Orloff, M. Utlaut, and L. Swanson, *High resolution focused ion beams: FIB and its applications*. New York: Kluwer Academic, 2002.

[56]   J. F. Walker, J. C. Reiner, and C. Solenthale, "Focused ion beam sample preparation for TEM," *Proc. Microsc. Semicond. Mater. Conf.*, pp. 629, 1995.

[57]   G. J. Athas, K. E. Noll, R. Mello, R. Hill, D. Yansen, F. F. Wenners, J. P. Nadeau, T. Ngo, and M. Siebers, "Focused ion beam system for automated MEMS prototyping and processing," *Proceedings of SPIE*, vol. 3223, pp. 198 - 207, 1997.

[58]   S.-J. Kim, T. Yamashita, K.-Y. Lee, M. Nagao, M. Sato, and H. Maeda, "Development of 3-D focused-ion-beam (FIB) etching methods for nano and micro-technology application," presented at 2001 International Microprocesses and nanotechnology Conference, Shimane, Japan, 2001.

[59]   T. Tao, J. Ro, and J. Melngailis, "Focused ion beam induced deposition of platinum," *Journal of Vacuum Society Technology*, vol. 8, pp. 1826 - 1829, 1990.

[60]   T. Tao, W. Wilkinson, and J. Melngailis, "Focused ion beam induced deposition of platinum for repair process," *Journal of Vacuum Society Technology*, vol. 9, pp. 162 - 164, 1991.

[61]   J. Melngailis, "Focused ion beam induced depostion - a review," presented at Proceedings of SPIE, 1991.

[62]   G. K. White and P. J. Messon, *Experimental techniques in low-temperature physics*, Fourth ed: Oxford University Press, 2002.

[63] Janis Research Company, Wilmington, MA. www.janis.com.

[64] "Lake Shore Cryotronics Inc., Model: HTR-50, Westerville, OH. www.lakeshore.com."

[65] R. F. Barron, *Cryogenic heat transfer*: Taylor & Francis, 1999.

[66] G. T. A. Kovacs, *Micromachined transducers sourcebook*: McGraw-Hill Company, 1998.

[67] "Lake Shore Cryotronics Inc., Model: DT-470-SD-12, Westerville, OH. www.lakeshore.com."

[68] "Lake Shore Cryotronics Inc., Model: 321, Westerville, OH. www.lakeshore.com."

[69] G. T. Dyos and T. Farrell, *Electrical resistivity handbook*: Peter Peregrinus Ltd., 1992.

[70] Lake Shore Cryotronics Inc., Stycast epoxy, Westerville, OH. www.lakeshore.com.

[71] D. A. Wigley, *MEchanical properties of materials at low temperatures*: Plenum Press, 1971.

[72] R. F. Barron, *Cryogenic systems*: Oxford University Press, 1985.

[73] M. A. Butler and S. J. Martin, "Magnetically-excited flexural plate wave devices," *Proceedings of Transducers '97*, pp. 1031 - 1034, 1997.

[74] T.-Y. Zhang, Y.-J. Su, C.-F. Qian, M.-H. Zhao, and L.-Q. Chen, "Microbridge testing of silicon nitride thin films deposited on silicon wafers," *Acta Materialia*, vol. 48, pp. 2843 - 2857, 2000.

[75] M. Hoummady, E. Farnault, H. Kawakatsu, and T. Masuzawa, "Applications of dynamic techniques for accurate determination of silicon nitride Young's moduli," *Transducer '97*, vol. 1, pp. 615 - 618, 1997.

[76] W.-H. Chuang, T. Luger, R. K. Fettig, and R. Ghodssi, "Mechanical property characterization of LPCVD silicon nitride thin films at cryogenic temperatures," *Journal of Microelectromechanical Systems*, vol. 13, pp. 870 - 879, 2004.

[77] W.-H. Chuang, T. Luger, R. K. Fettig, and R. Ghodssi, "Characterization of mechanical properties of silicon nitride thin films for space applications," *Proceedings of Materials Research Society*, vol. 782, pp. A5.21.1 - A5.21.6, 2004.

[78] W. D. Pilkey, *Formulas for stress, strain, and structural matrices*. New York: John Wiley & Sons, Inc., 1994.

[79]   M. Madou, *Fundamentals of microfabrication*: CRC Press, 1997.

[80]   J. P. Cleveland, S. Manne, D. Bocek, and P. K. Hansma, "A nondestructive method for determining the spring constant of cantilevers for scanning force microscopy," *Review of Scientific Instruments*, vol. 64, pp. 403 - 405, 1993.

[81]   A. Gupta, J. P. Denton, H. McNally, and R. Bashir, "Novel fabrication method for surface micromachined thin single-crystal silicon cantilever beams," *Journal of Microelectromechanical Systems*, vol. 12, pp. 185 - 192, 2003.

[82]   D. R. Askeland, *The science and engineering of materials*, Second ed. Boston: PWS - KENT, 1989.

[83]   D. Schneider and M. D. Tucker, "Non-destructive characterization and evaluation of thin films by laser induced ultrasonic surface waves," *Thin Solid Films*, vol. 209 - 291, pp. 305 - 311, 1996.

[84]   O. Tabata, K. Kawahata, S. Sugiyama, and I. Igarashi, "Mechanical property measurements of thin-films using load deflection of composite recrangular membranes," *Sensors and Actuators A: Physical*, vol. 20, pp. 135 - 141, 1989.

[85]   G. S. Brady, H. R. Clauser, and J. A. Vaccari, *Materials handbook*, Fifteen ed, 2002.

[86]   F. Mosteller and J. W. Tukey, *Data analysis and regression*: Addison - Wesley, 1977.

[87]   R. W. Hertzberg, *Deformation and fracture mechanics of engineering materials*: John Wiley & Sons, Inc., 1995.

[88]   G. Coles, R. L. Edwards, and W. N. Sharpe, Jr., "Mechanical properties of silicon nitride," *SEM Annual Conference*, 2001.

[89]   P. Hollman, A. Alahelisten, M. Olsson, and S. Hogmark, "Residual stress, Young's modulus and fracture strength of hot flame deposited diamond," *Thin Solid Films*, vol. 270, pp. 137 - 142, 1995.

[90]   T. P. Weihs, S. Hong, J. C. Bravman, and W. D. Nix, "Mechanical deflection of cantilever microbeams," *Journal of Materials Research*, vol. 3, pp. 931 - 942, 1988.

[91]   T. Namazu, Y. Isono, and T. Tanaka, "Nano-scale bending test of Si beam for MEMS," *MEMS 2000*, pp. 205 - 210, 2000.

[92]   H. D. Pierson, *Handbook of chemical vapor deposition, principles, technology, and applications*, 1999.

[93] J. Yang and O. Paul, "Fracture properties of LPCVD silicon nitride thin films from the load-deflection of long membranes," *Sensors and Actuators A: Physical,* vol. 97 - 98, pp. 520 - 526, 2002.

[94] J. P. Loughlin, R. K. Fettig, S. H. Moseley, A. S. Kutyrev, and D. Mott, "Structural Analysis of a Magnetically Actuated Silicon Nitride Micro-Shutter for Space Applications," presented at Nano Tech 2002-ICCN-MSM, San Juan, Puerto Rico, USA, 2002.

[95] H. Bongtae and G. Yifan, "Determination of an effective coefficient of thermal expansion of electronic packaging components: a whole-field approach," *IEEE Transactions on Components, Packaging, and Manufacturing Technology,* vol. 19, pp. 240 - 247, 1996.

[96] W.-H. Chu, M. Mehregany, and R. L. Mullen, "Analysis of tip deflection and force of a bimetallic cantilever microactuator," *Journal of Micromechanics and Microengineering,* vol. 3, pp. 4 - 7, 1993.

[97] C. S. Pan and W. Hsu, "An electro-thermally and laterally driven polysilicon microactuator," *Journal of Micromechanics and Microengineering,* vol. 7, pp. 7 - 13, 1997.

[98] M. P. Von Arx, O.   Baltes, H., "Process-dependent thin-film thermal conductivities for thermal CMOS MEMS," *Journal of Microelectromechanical Systems,* vol. 9, pp. 136 - 145, 2000.

[99] W.-H. Chuang, R. K. Fettig, and R. Ghodssi, "Mechanical property characterization of thin film materials for space applications," presented at 16th International Vaccum Congress, Venice, Italy, 2004.

[100] G. Stoney, "The tension of metallic films deposited by electrolysis," *Proceedings of Royal Society,* vol. 82, pp. 172, 1909.

[101] L. B. Freund, J. A. Floro, and E. Chason, "Extensions of the Stoney formula for substrate curvature to configurations with thin substrates or large deformations," *Applied Physics Letters,* vol. 74, pp. 1987 - 1989, 1999.

[102] H. Guckel, T. Randazzo, and D. W. Burns, "A simple technique for the determination of mechanical strain in thin films with applications to polysilicon," *Journal of Applied Physics,* vol. 57, pp. 1671 - 1675, 1985.

[103] H. Guckel, D. W. Burns, C. C. G. Visser, H. A. C. Tilmans, and D. Deroo, "Fine-grained polysilicon films with built-in tensile strain," *IEEE Transactions on Electron Devices,* vol. 35, pp. 800 - 801, 1988.

[104] M. G. Allen, M. Mehregany, R. T. Howe, and S. D. Senturia, "Microfabricated structures for the in situ measurement of residual stress, Young's modulus, and ultimate strain of thin films," *Applied Physics Letters,* vol. 51, pp. 241 - 243, 1987.

[105] M. Mehregany, R. T. Howe, and S. D. Senturia, "Novel microstructures for the in situ measurement of mechanical properties of thin films," *Journal of Applied Physics*, vol. 62, pp. 3579 - 3584, 1987.

[106] L. Lin, A. P. Pisano, and R. T. Howe, "A micro strain gauge with mechanical amplifier," *Journal of Microelectromechanical Systems*, vol. 6, pp. 313 - 321, 1997.

[107] T. F. Retajczyk and A. K. Sinha, "Elastic stiffness and thermal expansion coefficient of BN films," *Applied Physics Letters*, vol. 36, pp. 161 - 163, 1980.

[108] S. P. Murarka and T. F. Retajczyk, "Effect of phosphorus doping on stress in silicon and polycrystalline silicon," *Journal of Applied Physics*, vol. 54, pp. 2069 - 2072, 1983.

[109] V. Ziebart, O. Paul, and H. Baltes, "Extraction of the coefficient of thermal expansion of thin films from buckled membranes," *Proceedings of Material Research Society*, vol. 546, pp. 103 - 108, 1999.

[110] J.-H. Chae, J.-Y. Lee, and S.-W. Kang, "Measursment of thermal expansion coeffiecnt of poly-Si using microgauge sensors," *Sensors and Actuators A: Physical*, vol. 75, pp. 222 - 229, 1999.

[111] N. Tas, t. Sonnenberg, H. Jansen, R. Legtenberg, and M. Elwenspoek, "Stiction in surface micromachining," *Journal of Micromechanics and Microengineering*, vol. 6, pp. 385 - 397, 1996.

[112] Y. Okada and Y. Tokumaru, "Precise determination of lattice parameter and thermal expansion coefficient of silicon between 300 and 1500 K," *Journal of Applied Physics*, vol. 56, pp. 314 - 320, 1984.

[113] T. F. Retajczyk and A. K. Sinha, "Elastic stiffness and thermal expansion coefficients of various refractory silicides and silicon nitride films," *Thin Solid Films*, vol. 70, pp. 241 - 247, 1980.

[114] C. H. Mastrangelo, Y. C. Tai, and R. S. Muller, "Thermophysical properties of low-residual-stress, silicon rich LPCVD silicon nitride films," *Sensors and Actuators A: Physical*, vol. 23, pp. 856 - 880, 1990.

[115] C. L. Muhlstein, S. B. Brown, and R. O. Ritchie, "High-cycle fatigue of single-crystal silicon thin films," *Journal of Microelectromechanical Systems*, vol. 10, pp. 593-600, 2001.

[116] C. L. Muhlstein, E. A. Stach, and R. O. Ritchie, "Mechanism of fatigue in micro-scale films of polycrystalline silicon for microelectromechanical systems," *Applied Physics Letters*, vol. 80, pp. 1532-1534, 2002.

[117]   R. O. Ritchie, "Mechanisms of fatigue-crack propagation in ductile and brittle solids," *International Journal of Fracture*, vol. 100, pp. 55-83, 1999.

[118]   J. Bagdahn and W. N. Sharpe, "Fatigue of polycrystalline silicon under long-term cyclic loading," *Sensors and Actuators A*, vol. 103, pp. 9-15, 2003.

[119]   H. S. Cho, K. J. Hemker, K. Lian, and J. Goettert, "Tensile, creep and fatigue properties of LIGA nickel structures," presented at The Fifteenth IEEE International Conference on Micro Electro Mechanical Systems, 2002.

[120]   R. Ballarini, R. L. Mullern, H. Kahn, and A. H. Heuer, "The fracture toughness of polysilicon microdevices," presented at Materials Research Society, San Francisco, CA, 1998.

[121]   W. Van Arsdell and S. B. Brown, "Crack growth in polysilicon," presented at ASME International Mechanical Engineering Congress and Exposition, Anaheim, CA, 1998.

[122]   W.-H. Chuang, R. K. Fettig, and R. Ghodssi, "A novel electrostatic actuator for fatigue testing of low-stress LPCVD silicon nitride thin films," *Sensors and Actuators A: Physical*, 2005 (in press).

[123]   W.-H. Chuang, R. K. Fettig, and R. Ghodssi, "FIB-based cryogenic characterization and testing of silicon nitride thin film materials and devices for space applications," *Proceedings of Materials Research Society*, vol. 851, pp. NN5.16.1 - NN5.16.6, 2005.

[124]   W. C. Young, *Roark's formulas for stress & strain*, Sixth ed: McGraw-Hill, 1989.

[125]   A. A. Ayon, X. Zhang, and R. Khanna, "Anisotropic silicon trenches 300-500 um deep employing time multiplexed deep etching (TMDE)," *Sensors and Actuators A*, vol. 91, pp. 381 - 385, 2001.

[126]   J. W. Coburn and H. F. Winters, "Conductance considerations in the reactive ion etching of high aspect ratio features," *Applied Physics Letters*, vol. 55, pp. 2730 - 2732, 1989.

[127]   J. B. Hudson, *Surface science: an introduction*: Wiley-Interscience, 1998.

[128]   A. A. Ayon, R. Braff, C. C. Lin, H. H. Sawin, and M. A. Schmidt, "Characterization of a time multiplexed inductively coupled plasma etcher," *Journal of The Electrochemical Society*, vol. 146, pp. 339 - 349, 1999.

[129]   A. A. Ayon, R. Braff, R. Bayt, H. H. Sawin, and M. A. Schmidt, "Influence of coil power on the etching characteristics in a high density plasma etcher," *Journal of The Electrochemical Society*, vol. 146, pp. 2730 - 2736, 1999.

[130] J. Orloff, M. Utlaut, and L. Swanson, *High Resolution Focused Ion Beams*: Kluwer, 2002.

[131] J. N. Ding, Y. G. Meng, and S. Z. Wen, "Size effect on the mechanical properties and reliability analysis of microfabricated polysilicon thin films," presented at IEEE International Reliability Physics Symposium, Orlando, FL, 2001.

[132] R. J. Corruccini and J. J. Gniewek, *Thermal expansion of technical solids at low temperatures*: National Bureau of Standards, 1961.

[133] S. G. Nilsson, X. Borrise, and L. Montelius, "Size effect on Young's modulus of thin chromium cantilevers," *Applied Physics Letters*, vol. 85, pp. 3555 - 3557, 2004.

[134] J.-A. Schweitz, "Mechanical characterization of thin films by micromechanical techniques," *MRS Bulletin*, pp. 34 - 45, 1992.

[135] B. W. Kempshall, L. A. Giannuzzi, B. I. Prenitzer, F. A. Stevie, and S. X. Da, "Compressive evaluation of protective coatings and focused ion beam chemical vapor deposition processes," *Journal of Vacuum Society Technology*, vol. 20, pp. 286-290, 2002.

[136] S. Rubanov and P. R. Munroe, "FIB-induced damage in silicon," *Journal of Microscopy*, vol. 214, pp. 213-221, 2003.

[137] C. L. Muhlstein, S. B. Brown, and R. O. Ritchie, "High-cycle fatigue and durability of polycrystalline silicon thin films in ambient air," *Sensors and Actuators A*, vol. 94, pp. 177 - 188, 2001.

[138] S. Suresh, *Fatigue of materials*, First ed: Cambridge University Press, 1991.

[139] C. R. Soderberg, "Factor of safety and working stress," *Transactions of the American Society of Mechanical Engineerings*, vol. 52, pp. 13 - 28, 1939.

[140] J. A. Bannantine, J. J. Comer, and J. L. Handrock, *Fundamentals of metal fatigue analysis*: Englewood Cliffs: Prentice-Hall, 1990.

[141] Y. S. Garud, "Multiaxial fatigue: a survey of the state of the art," *Journal of testing and evaluation*, vol. 9, pp. 165 - 178, 1981.

[142] A. S. Kutyrev, R. Arendt, S. H. Moseley, R. A. Boucarut, T. Hadjimichael, M. Jhabvala, T. King, M. J. Li, J. Loughlin, D. Rapchun, D. S. Schwinger, and R. F. Silverberg, "Programmable microshutter arrays for the JWST NIRSpec: optical performance," *IEEE Journal of Selected Topics in Quantum Electronics*, vol. 10, pp. 652 - 661, 2004.

[143] A. N. Cleland and M. L. Roukes, "Fabrication of high frequency nanometer scale mechanical resonators from bulk Si substrates," *Applied Physics Letters*, vol. 69, pp. 2653, 1996.

[144] A. N. Cleland and M. L. Roukes, "A nanometer-scale mechanical electrometer," *Nature*, vol. 392, pp. 160, 1998.

[145] K. Schwab, E. A. Henriken, J. M. Worlock, and M. L. Roukes, "Measurements of the quantum of thermal conductance," *Nature*, vol. 404, pp. 974, 2000.

[146] A. A. G. Requicha, "Nanorobots, NEMS, and nanoassembly," *Proceedings of IEEE*, vol. 91, pp. 1922 - 1933, 2003.

[147] R. S. Muller, "Microdynamics," *Sensors and Actuators A*, vol. 21, pp. 1 - 8, 1990.

[148] W.-H. Chuang, R. K. Fettig, and R. Ghodssi, "High-Cycle Fatigue Testing of Micro/nano-Scale Silicon Nitride Thin Films Using a Novel Mechanical-Amplifier Actuator," presented at Materials Research Society 2005 Spring Meeting, San Francisco, CA, 2005.

[149] W.-H. Chuang, R. K. Fettig, and R. Ghodssi, "Fatigue study of nano-scale silicon nitride thin films using a novel electrostatic actuator," presented at The 13th International Conference on Solid-State Sensors, Actuators, and Microsystems (Transducers '05), Seoul, Korea, 2005.

[150] T. Namazu, Y. Isono, and T. Tanaka, "Evaluation of size effect on mechanical properties of single crystal silicon by nanoscale bending test using AFM," *Journal of Microelectromechanical Systems*, vol. 9, pp. 450 - 459, 2000.

[151] Y. Isono, T. Namazu, and T. Tanaka, "AFM bending testing of nanometric single crystal silicon wire at intermediate temperatures for MEMS," presented at IEEE International Conference on Micro Electro Mechanical Systems, Interlaken, Switzerland, 2001.

[152] T. Namazu and T. Isono, "Quasi-static/cyclic loading tests of nanometric SiO2 wires using AFM technique for NEMS designs," presented at IEEE Conference on Nanotechnology, 2002.

[153] S. Sundararajan and B. Bhushan, "Development of AFM-based techniques to measure mechanical properties of nanoscale structures," *Sensors and Actuators A*, vol. 101, pp. 338 - 351, 2002.

[154] J. H. Poynting, "On pressure perpendicular to the shear planes in finite pure shears, and on the lengthening of loaded wires when twisted," *Proceedings of the Royal Society of London*, vol. 82, pp. 546 - 559, 1909.

[155] M. Kuball, F. H. Morrissey, M. Benyoucef, I. Harrison, D. Korakakis, and C. T. Foxon, "Nano-fabrication of GaN pillars using focused ion beam etching," *Physica Status Solidi (a)*, vol. 176, pp. 355, 1999.

[156] L. Biao, X. Huimin, X. Bai, R. Geer, and J. Castracane, "Investigation of strain in microstructures by a novel moire method," *Journal of Microelectromechanical Systems*, vol. 11, pp. 829 - 836, 2002.